YUKAWA INSTITUTE FOR THEORETICAL PHYSICS

DOCTORAL THESIS

Rho resonance from lattice QCD: Technical improvement and its application

---

Author: Yutaro AKAHOSHI

A thesis submitted in fulfillment of the requirements for the degree of Doctor of Science

in the

Department of Physics
Kyoto University

January 4, 2022

Abstract

In this thesis, we introduce our challenges on the ρ resonance study from lattice QCD. Recent discoveries of exotic hadrons call for the first-principle study of hadron interactions from lattice QCD. The HAL QCD method enables us to study them from the spacetime dependence of correlation functions in lattice QCD, but there is a technical issue: the estimation of all-to-all quark propagators.

To overcome the difficulty, we first employ one of the typical methods to calculate all-to-all propagators called the hybrid method. We calculate $I = 1, 2$ $\pi\pi$ interactions and investigate the behaviors of HAL QCD potentials systematically. We find that the computational cost to reduce noise contamination from the hybrid method is too large to perform large-scale simulations. We then seek the better calculation scheme in which both noise contamination and computational cost are low. As a result, we find that the combination of the one-end trick, the sequential propagator technique, and the covariant approximation averaging (CAA) can achieve the requirements.

Using the new calculation scheme, we next investigate the ρ meson resonance appearing in the $I = 1$ $\pi\pi$ interaction with large box size and small pion mass enough for the ρ meson to be a resonance. Thanks to the new scheme, we succeed in the determination of the non-local $I = 1$ $\pi\pi$ potential at the next-to-next-to-leading order (N^2LO) of the derivative expansion for the first time. The N^2LO potential reproduces a typical resonance behavior of the scattering phase shift, and resonance mass and coupling of the ρ resonance is extracted directly from the pole search of the S-matrix via the complex-scaled Schrödinger equation. We find that the resonance mass is consistent with the value in the literature, while the coupling turns out to be somewhat larger. The latter observation may be attributed to the truncation error of the derivative expansion in a near-threshold region, where the center-of-mass energy levels cannot cover.

We finally study the laboratory frame formalism of the HAL QCD method with the one-end trick. The laboratory frame calculation can be applied to reduce systematics appearing in the resonance study, for example, the truncation error of the derivative expansion and the vacuum contamination. We calculate the $I = 2$ $\pi\pi$ S-wave interaction from both the laboratory frame and center-of-mass frame formalisms and compare those results with each other. The potentials extracted from the laboratory frame NBS wave function gives consistent phase shifts with that of the center-of-mass frame as well as values obtained from the Lüshcer's method.

Our series of studies on the cooperation of the all-to-all propagators and the HAL QCD method establishes one of the promising ways to study hadronic resonances from lattice QCD. Furthermore, our calculation scheme can be applied to other interactions like nuclear force. We also mention future applications of our strategy to both exotic resonances and other interactions in the last of the thesis.

Contents

List of Publications

Papers related to the thesis

1. Yutaro Akahoshi, Sinya Aoki, and Takumi Doi,
"Emergence of the ρ resonance from the HAL QCD potential in lattice QCD"
Phys. Rev. D **104** 054510 (2021) [arXiv:2106.08175[hep-lat]].

2. Yutaro Akahoshi, Sinya Aoki, Tatsumi Aoyama, Takumi Doi, Takaya Miyamoto and Kenji Sasaki,
"The HAL QCD potential in $I = 1$ $\pi\pi$ system with the ρ meson bound state"
PTEP **2020**, no.7, 073B07 (2020) [arXiv:2004.01356[hep-lat]].

3. Yutaro Akahoshi, Sinya Aoki, Tatsumi Aoyama, Takumi Doi, Takaya Miyamoto, Kenji Sasaki,
"$I = 2$ $\pi\pi$ potential in the HAL QCD method with all-to-all propagators"
PTEP **2019**, no.8 083B02 (2019) [arXiv:1904.09549[hep-lat]].

Published papers not included in the thesis

1. Kotaro Murakami, Yutaro Akahoshi, and Sinya Aoki,
"S-wave kaon-nucleon potentials with all-to-all propagators in the HAL QCD method"
PTEP **2020**, no.9, 093B03 (2020) [arXiv:2006.01383[hep-lat]].

2. Takaya Miyamoto, Yutaro Akahoshi, Sinya Aoki, Tatsumi Aoyama, Takumi Doi, Takaya Miyamoto, Gongyo Shinya, Kenji Sasaki,
"Partial wave decomposition on the lattice and its applications to the HAL QCD method"
Phys. Rev. D **101**, no.7, 074514 (2020) [arXiv:1906.01987[hep-lat]].

Chapter 1

Introduction

Understanding hadron interactions is one of the most important challenges in particle and nuclear physics. Hadrons are composite particles of the fundamental quarks and gluons, most of which can be categorized into two families by the quark model [1–3]: baryons made of three quarks (qqq) and mesons made of one quark and one antiquark ($q\bar{q}$) [4]. On the other hand, there are some hadronic states which deviate from the quark model predictions, called "exotic hadrons". Such exotic states are first discovered by experiments in 2003. For example, $X(3872)$, the first signal in the charmonium-like X, Y, Z states, is observed in Belle experiment [5]. Many exotic states have been discovered in experiments since the first observation and various phenomenological models have been proposed to describe them (see, e.g. recent review [6], for details). Exotic hadrons have also been predicted and discussed theoretically for a long time, even before the experimental discovery in 2003. The prime example is the light scalar meson called σ [7]. The investigation of corresponding hadron interactions is important to shed light on them.

In particle physics, we know that the dynamics of quarks and gluons are described by quantum chromodynamics (QCD). QCD is defined as the SU(3) non-Abelian gauge theory with fermions and has a striking nature that the interaction becomes strong in low energy. Therefore, a non-perturbative treatment is mandatory to study low-energy phenomena including hadron physics from QCD. One sophisticated way to realize it is lattice QCD, whose fundamental formulation is firstly introduced by K. G. Wilson[8]. Lattice QCD has been succeeded in numerical demonstration of the quark confinement[9] and reproduction of the spectroscopy of single hadrons[10]. From the viewpoint of the quarks and gluons, exotic hadrons, as well as standard ones, should be understood by QCD in a unified manner. Under these circumstances, the first-principle study of the hadronic interactions and corresponding resonances becomes one of the hottest research topics in the lattice QCD community.

Investigating hadron interactions from lattice QCD is, however, not straightforward work, since the real-time evolutions like particle scatterings is not directly accessed from lattice QCD on Euclidean spacetime [11]. In such a situation, M. Lüshcer discovers a relation between the scattering phase shift and the finite-volume energy eigenstates in 1991 [12], and it opens a new

frontier to study hadron interactions from lattice QCD. At the beginning the formulation is restricted to the elastic scattering of two scalar particles in the center-of-mass frame, it has been extended to the laboratory frames and multi-channel (inelastic) scattering afterward [13, 14]. The Lüscher's finite volume method has been mainly applied to elastic/inelastic meson-meson scatterings and some impressive results on corresponding mesonic resonances have appeared [15]. After the discovery of the Lüscher's method, an alternative approach to study hadron interactions from lattice QCD, called the HAL QCD method, is proposed [16–18]. The HAL QCD method enables us to construct energy-independent non-local potentials of hadron interactions from the spacetime dependence of the correlation function. It has been mainly applied to baryon-baryon interactions, to which the Lüscher's method is hard to apply [19]. Recent near-physical point simulations predict the existence of some nontrivial two-baryon bound states (dibaryons) [20–22]. Exotic $Z_c(3900)$ is also studied in detail, and it is found that this state may not be a particle-like object but a kinematical effect [23, 24]. Furthermore, the direct comparison between the HAL QCD result and the experimental data is performed by the ALICE Collaboration, and authors find that the HAL QCD potentials of the proton-Ξ and proton-Ω interactions reproduce the experimental scattering amplitude well [25]. The study of hadron-hadron interactions from lattice QCD now enters, therefore, a new stage of a direct comparison with experimental results.

On the other hand, there are some remaining issues in the study of the hadron interactions from lattice QCD. In the Lüshcer's method, precise studies are restricted only to the meson-meson interaction due to the difficulty of the precise determination of two-baryon energy eigenstates. Furthermore, bias-free analyses on multi-channel scatterings are difficult since it is inevitable to introduce some ansatze of the energy dependence of the multi-channel scattering amplitudes. As regards the HAL QCD method, a mature way to calculate the full contents of the quark propagator (so-called all-to-all propagator) has not been established yet, while the problems in the Lüshcer's method introduced above can be avoided. The enlargement of the applicability of the HAL QCD method is especially beneficial since it is relatively less biased and brings the information of the hadron interaction as the potential explicitly. Therefore, it is mandatory to overcome the problem of the all-to-all propagator in the HAL QCD method.

The all-to-all quark propagator is mathematically an inverse of the large sparse matrix, whose naive calculation needs over tens or hundreds of years to finish, even when we run it on supercomputers. We then need to reduce the numerical cost by introducing some approximation, and our mission is to find or invent the all-to-all method with the best compatibility to the HAL QCD method. The previous work[26, 27] employs one of the famous approximation methods called the Laplacian-Heaviside (LapH) method (or distillation)[28], which is widely applied to analyses of the Lüshcer's method. Authors calculate the HAL QCD potential with and without the LapH method and find that the LapH method enlarges the non-locality of the potential[26]. The enhancement of the non-locality of the potential is not suitable for our practical calculation, since we have to approximate the non-locality by small-order truncation of some series expansion in practice. A more compatible method is desired.

Under these circumstances, we first investigate another possibility of the all-to-all calculations to establish the best marriage of the all-to-all propagator and the HAL QCD method. We employ the hybrid method [29], which relies on the low-mode spectral decomposition and high-mode stochastic estimation. It is expected not to enlarge the non-locality like the LapH method. We find that the precise potential can be obtained if the contamination from the high-mode estimation is suppressed well [30, 31]. On the other hand, the noise reduction needs a lot of numerical costs and it seems difficult to apply this method to large-scale simulations. We, therefore, investigate other possibilities with less usage of stochastic estimations and find that the combination of the three techniques, namely the one-end trick [32], the sequential propagator [33] and covariant approximation averaging [34]. Some test calculation shows over $\mathcal{O}(10^2)$ improvements against the case before.

We next apply the new calculation scheme of the all-to-all calculation to the $I = 1$ $\pi\pi$ P-wave interaction. This system is the simplest nontrivial system containing a narrow resonance state, known as the ρ resonance. It is experimentally observed at an energy of $m_\rho \sim 770$ MeV with width $\Gamma_\rho \sim 150$ MeV[4], and its P-wave phase shift is known as a prime example of the narrow resonance[35, 36] Theoretically, the ρ resonance plays a fundamental role in understanding many processes in the context of vector meson dominance[37]. It is also known that the nuclear force at the middle range is phenomenologically understood by exchanges of the ρ meson, together with π, ω, and σ[38]. In lattice QCD community, this system has been widely studied [39–47] since it can be simply investigated by the single-channel approximation and contains a typical numerical difficulty of resonance studies, the all-to-all propagators. As a result, we succeed in the determination of the non-local potential at the N^{2}LO for the first time and reproduce the typical resonance structure corresponding to the ρ meson, up to the remaining truncation error of the approximation of the non-locality [48]. One of the possibilities to reduce the remaining truncation error is introducing the scattering analysis in the laboratory frame [49], but the laboratory frame extension of the HAL QCD method has not been verified numerically yet due to the difficulty of the all-to-all propagator. Using the one-end trick, we numerically investigate the laboratory frame formalism for the first time and confirm that the potential can be reasonably obtained by the formalism.

The series of our study establishes one way to treat all-to-all propagators in the framework of the HAL QCD method. Furthermore, we also complete the laboratory frame formalism of the HAL QCD method as a byproduct of the all-to-all studies. Those achievements can be widely applied to further investigations of hadron interactions and may produce many important results in the future.

This thesis is organized as follows. In Chapter 2, we briefly introduce the basic formulations of lattice QCD and a typical procedure of its numerical calculation. We introduce the fundamental concepts to describe the hadron interaction and the ways to study it from lattice QCD, the HAL QCD method and the Lüshcer's method, in Chapter 3. Chapter 4 is devoted to introducing

the problem of the all-to-all propagator and its approximation methods. From Chapter 5, we discuss the results of our studies. In Chapter 5, studies on the application of the hybrid method are discussed. We also discuss the new calculation strategy and its first trial here. The main result of this thesis, the study of the ρ resonance using the new calculation strategy, is discussed in Chapter 6. Chapter 7 gives the study of the laboratory frame formalism of the HAL QCD method. Finally, the summary and perspective of our study are presented in Chapter 8.

Chapter 2

Lattice QCD

Since the QCD coupling becomes strong in the low-energy region where hadronic phenomena occur, it is impossible to study them by the perturbation theory. However, the lattice gauge theory, which is first proposed by K. G. Wilson [8], enables us to analyze QCD non-perturbatively by numerical simulations. In this chapter, we introduce a formulation of lattice QCD and its typical application to the extraction of hadron masses.

2.1 Lattice regularization of QCD

In the lattice regularization, we define a target theory on a discretized Euclidean spacetime with a finite volume. It allows the numerical estimation of the path integral. Here we discuss how to formulate QCD on the lattice Euclidean spacetime in detail. We employ the Einstein convention for summations of indices unless otherwise stated.

2.1.1 Euclidean action of QCD

Let us begin with the QCD action on the continuum Minkowski spacetime,

$$S_M = \int d^4x\, \bar{\psi}^{(f)}(i\gamma^\mu D_\mu - m^{(f)})\psi^{(f)} - \int d^4x\, \frac{1}{2g^2}\mathrm{tr}(F_{\mu\nu}F^{\mu\nu}), \tag{2.1}$$

where an index f represents flavors of quarks $(u, d, s, \cdots)$, and the metric of the Minkowski spacetime is given as

$$\eta_{\mu\nu} = \mathrm{diag}(1, -1, -1, -1). \tag{2.2}$$

D_μ and $F_{\mu\nu}$ are defined as

$$D_\mu = \partial_\mu + iA_\mu, \tag{2.3}$$

$$F_{\mu\nu} = \partial_\mu A_\nu - \partial_\nu A_\mu + i\left[A_\mu, A_\nu\right], \tag{2.4}$$

with $[A, B] \equiv AB - BA$. The gauge field A_μ is an element of Lie algebra $\mathfrak{su}(3)$,

$$A_\mu = A_\mu^a T^a, \tag{2.5}$$

where T^a are trace-less Hermitian matrices called generators of Lie group SU(3). The generators obey

$$[T^a, T^b] = if^{abc}T^c, \tag{2.6}$$

where f^{abc} is a structure constant. Gamma matrices $\gamma_\mu(\mu = 0, 1, 2, 3)$ are 4×4 matrices in the spinor space which satisfy

$$\begin{aligned} \{\gamma_\mu, \gamma_\nu\} &= 2\eta_{\mu\nu} && (2.7)\\ (\gamma_0)^\dagger &= \gamma_0 && (2.8)\\ (\gamma_i)^\dagger &= -\gamma_i \ (i = 1, 2, 3), && (2.9) \end{aligned}$$

with $\{A, B\} \equiv AB + BA$. In the Dirac representation, their explicit forms are given as

$$\gamma_0 = \begin{pmatrix} \mathbf{1} & 0 \\ 0 & -\mathbf{1} \end{pmatrix} \tag{2.10}$$

$$\gamma_1 = \begin{pmatrix} 0 & \sigma_1 \\ -\sigma_1 & 0 \end{pmatrix} \tag{2.11}$$

$$\gamma_2 = \begin{pmatrix} 0 & \sigma_2 \\ -\sigma_2 & 0 \end{pmatrix} \tag{2.12}$$

$$\gamma_3 = \begin{pmatrix} 0 & \sigma_3 \\ -\sigma_3 & 0 \end{pmatrix}, \tag{2.13}$$

where $\mathbf{1}$ is a 2×2 unit matrix and σ_i $(i = 1, 2, 3)$ are the Pauli matices. γ_5 is defined as

$$\gamma_5 = i\gamma_0\gamma_1\gamma_2\gamma_3. \tag{2.14}$$

The action (Eq.(2.1)) is invariant for the following local gauge transformation,

$$\begin{aligned} \psi(x) &\rightarrow \Omega(x)\psi(x) && (2.15)\\ \bar{\psi}(x) &\rightarrow \bar{\psi}(x)\Omega^\dagger(x) && (2.16)\\ A_\mu(x) &\rightarrow \Omega(x)A_\mu(x)\Omega^\dagger(x) - i\Omega(x)\partial_\mu\Omega^\dagger(x), && (2.17) \end{aligned}$$

where $\Omega(x)$ is a local gauge transformation matrix.

Next, let us move on to the Euclidean spacetime. The coordinates in the Euclidean spacetime $x_\mu^{(E)}$ $(\mu = 1, 2, 3, 4)$ are defined by the Wick rotation,

$$x^0 = -ix_4^{(E)} \tag{2.18}$$
$$x^i = x_i^{(E)} \ (i = 1, 2, 3) \tag{2.19}$$
$$\partial_0 = i\partial_4^{(E)} \tag{2.20}$$
$$\partial_i = \partial_i^{(E)} \ (i = 1, 2, 3). \tag{2.21}$$

The gauge field and the gamma matrices in the Euclidean spacetime, $A_\mu^{(E)}$ and $\gamma_\mu^{(E)}$, are defined as

$$A_0 = iA_4^{(E)} \tag{2.22}$$
$$A_i = A_i^{(E)} \ (i = 1, 2, 3) \tag{2.23}$$
$$\gamma^0 = \gamma_4^{(E)} \tag{2.24}$$
$$\gamma^i = i\gamma_i^{(E)}. \tag{2.25}$$

$\gamma_\mu^{(E)}$ now satisfies

$$\{\gamma_\mu^{(E)}, \gamma_\nu^{(E)}\} = 2\delta_{\mu\nu}, \ \delta_{\mu\nu} = \mathrm{diag}(1, 1, 1, 1) \tag{2.26}$$
$$(\gamma_\mu^{(E)})^\dagger = \gamma_\mu^{(E)}. \tag{2.27}$$

Substituting them into the original action Eq.(2.1), we obtain the Euclidean action as

$$S_E \equiv -iS_M = \sum_f \int d^4x^{(E)} \ \bar{\psi}^{(f)}(\gamma_\mu^{(E)}(\partial_\mu^{(E)} + iA_\mu^{(E)}) + m^{(f)})\psi^{(f)} + \int d^4x^{(E)} \ \frac{1}{2g^2}\mathrm{tr}(F_{\mu\nu}F_{\mu\nu}). \tag{2.28}$$

In the following discussion, we consider the Euclidean spacetime unless otherwise stated. We, therefore, ignore superscripts (E) and describe all Euclidean indices (μ, ν, etc.) as subscripts since positions of the indices (upper or lower) are no longer meaningful.

2.1.2 Lattice regularization

Now let us discuss the lattice regularization of the Euclidean action introduced above. The continuous Euclidean spacetime is replaced by a 4D finite lattice which contains $|\Lambda|$ lattice points (sites) with an interval (lattice spacing) a,

$$\Lambda = \{n = (n_1, n_2, n_3, n_4) \ | n_\mu = 0, 1, 2, ..., N_\mu - 1, \ |\Lambda| = N_1N_2N_3N_4\}, \tag{2.29}$$

and the fields $\psi, \bar{\psi}$ is defined on each sites. The spacetime coordinates x_μ is described by the dimensionless 4D vector n_μ as $x_\mu = an_\mu$. Thanks to this regularization, we can treat QCD as a

quantum system with finite degrees of freedom. This procedure corresponds to the UV cut-off with a cut-off parameter $1/a$, therefore it is called "lattice regularization".

The quark part of Euclidean action is discretized by the replacement of derivatives with differences as

$$a^4 \sum_{n\in\Lambda} \bar{\psi}(n) \left(\sum_{\mu=1}^{4} \gamma_\mu \frac{U_\mu(n)\psi(n+\hat{\mu}) - U_\mu^\dagger(n-\hat{\mu})\psi(n-\hat{\mu})}{2a} + m\psi(n) \right), \tag{2.30}$$

here we employ a central difference and only consider a case of a single flavor. $U_\mu(n)$ is an SU(3) matrix called "link variable", which is transformed by the local gauge transformation as

$$U_\mu(n) \to \Omega(n) U_\mu(n) \Omega^\dagger(n+\hat{\mu}). \tag{2.31}$$

Together with the gauge transformation property of the quark fields,

$$\psi(n) \to \Omega(n)\psi(n) \tag{2.32}$$
$$\bar{\psi}(n) \to \bar{\psi}(n)\Omega^\dagger(n), \tag{2.33}$$

the discretized quark action(2.30) is invariant under the local gauge transformation.

The link variable introduced above is a lattice counterpart of the Wilson line (or gauge transporter) [50] in the continuum theory, which is defined as

$$G(x,y) = \mathrm{P}\exp\left[i\int_x^y A\cdot dx \right] \equiv \lim_{N\to\infty} \prod_{n=0}^{N-1} \left[1 + iA_\mu(x+n\Delta x)\Delta x_\mu \right], \tag{2.34}$$

where $|\Delta x| = \frac{|y-x|}{N}$. When the lattice spacing a is fine it can be directly related to the gauge field as

$$U_\mu(n) = e^{iaA_\mu(n)} \left(\approx \mathrm{P} e^{i\int_x^{x+a\hat{\mu}} A\cdot dx} \right). \tag{2.35}$$

In the lattice gauge theory, we treat the link variable U_μ as a fundamental variable instead of the gauge field A_μ. This treatment makes the gauge part of the path integral well-defined without any gauge fixing. Therefore the role of the gauge fixing changes. For instance, we need it to calculate the non-gauge invariant quantities such as smeared hadron propagators (it will be discussed later).

Next, let us discuss the lattice regularization of the gauge action. The simplest one is the plaquette action, which is introduced by K. G. Wilson [8],

$$\frac{\beta}{3} \sum_{n\in\Lambda} \sum_{\mu<\nu} \mathrm{Re}\,\mathrm{tr}(\mathbf{1} - U_{\mu\nu}(n)), \tag{2.36}$$

where $\beta \equiv \frac{6}{g^2}$. $U_{\mu\nu}(n)$ is the smallest Wilson loop called the plaquette and defined as

$$U_{\mu\nu}(n) \equiv U_\mu(n)U_\nu(n+\hat{\mu})U_\mu^\dagger(n+\hat{\nu})U_\nu^\dagger(n). \tag{2.37}$$

A schematic figure of the plaquette is given in Fig. 2.1. Generally speaking, we can introduce not

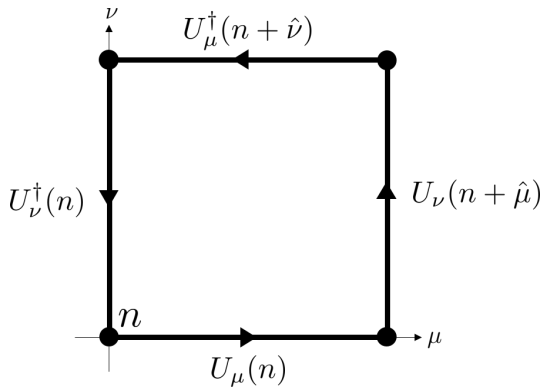

FIGURE 2.1: Schematic figure of the plaquette, $U_{\mu\nu}(n)$.

only the plaquette but also other Wilson loops in the definition of the lattice action, as long as it correctly reproduces the continuum action. Such an ambiguity is utilized to reduce unnecessary systematics of the lattice action, as will be discussed later.

In summary, the lattice regularization leads to the following QCD action:

$$S_E = S_F + S_G, \tag{2.38}$$

$$S_F = a^4 \sum_{n\in\Lambda} \bar{\psi}(n) \left(\sum_{\mu=1}^{4} \gamma_\mu \frac{U_\mu(n)\psi(n+\hat{\mu}) - U_\mu^\dagger(n-\hat{\mu})\psi(n-\hat{\mu})}{2a} + m\psi(n) \right), \tag{2.39}$$

$$S_G = \frac{\beta}{3} \sum_{n\in\Lambda} \sum_{\mu<\nu} \mathrm{Re\ tr}(\mathbf{1} - U_{\mu\nu}(n)). \tag{2.40}$$

We demonstrate how it reproduces the continuum theory at the limit of $a \to 0$ in Appendix A. In practice, however, we cannot use this action as it is due to the doubling problem of the fermion action. Furthermore, modern lattice simulations commonly employ some improved actions to reduce discretization errors. We discuss those issues in the following sections.

2.1.3 Doubling problem

To understand the doubling problem, let us consider a free lattice fermion (Eq.(2.39) with $U_\mu \equiv \mathbf{1}$),

$$S_F = a^4 \sum_{n\in\Lambda} \bar{\psi}(n) \left(\sum_{\mu=1}^{4} \gamma_\mu \frac{\psi(n+\hat{\mu}) - \psi(n-\hat{\mu})}{2a} + m\psi(n) \right), \tag{2.41}$$

$$\equiv a^4 \sum_{n,m\in\Lambda} \bar{\psi}(n) D(n|m) \psi(m), \tag{2.42}$$

$$D(n|m) = \left(\sum_{\mu=1}^{4} \gamma_\mu \frac{\delta_{n+\hat{\mu},m} - \delta_{n-\hat{\mu},m}}{2a} + m\delta_{n,m}\mathbf{1}_{\text{spinor}} \right) \mathbf{1}_{\text{color}}, \tag{2.43}$$

where $\mathbf{1}_{\text{spinor}}$ and $\mathbf{1}_{\text{color}}$ are unit matrices of spinor and color spaces, respectively. In the following we call $D(n|m)$ the Dirac operator. To investigate one-particle states this action contains, we consider the Fourier transformation of the Dirac operator as

$$\begin{aligned}
\tilde{D}(p|q) &= \sum_{n,m\in\Lambda} e^{-ip\cdot na} D(n|m) e^{iq\cdot ma} && (2.44)\\
&= \sum_{n,m\in\Lambda} e^{-ip\cdot na} \left(\sum_{\mu=1}^{4} \gamma_\mu \frac{\delta_{n+\hat{\mu},m} - \delta_{n-\hat{\mu},m}}{2a} + m\delta_{n,m}\mathbf{1}_{\text{spinor}} \right) \mathbf{1}_{\text{color}} e^{iq\cdot ma} && (2.45)\\
&= \sum_{n\in\Lambda} e^{-i(p-q)\cdot na} \left(\sum_{\mu=1}^{4} \gamma_\mu \frac{e^{iq\cdot\hat{\mu}a} - e^{-iq\cdot\hat{\mu}a}}{2a} + m\mathbf{1}_{\text{spinor}} \right) \mathbf{1}_{\text{color}} && (2.46)\\
&= |\Lambda|\delta_{p,q}\Big(\sum_{\mu} \frac{i}{a}\gamma_\mu \sin(p_\mu a) + m\mathbf{1}_{\text{spinor}}\Big)\mathbf{1}_{\text{color}} && (2.47)\\
&\equiv |\Lambda|\delta_{p,q}\mathbf{1}_{\text{color}}\tilde{D}(p). && (2.48)
\end{aligned}$$

Since the one-particle states correspond to the poles of the propagator in the momentum space,

$$\begin{aligned}
\tilde{D}^{-1}(p) &= \frac{1}{\sum_\mu \frac{i}{a}\gamma_\mu \sin(p_\mu a) + m\mathbf{1}_{\text{spinor}}} && (2.49)\\
&= \frac{m\mathbf{1}_{\text{spinor}} - \sum_\mu \frac{i}{a}\gamma_\mu \sin(p_\mu a)}{m^2 + \frac{1}{a^2}\sum_\mu \sin^2(p_\mu a)}, && (2.50)
\end{aligned}$$

we can study them by the solutions of

$$m^2 + \frac{1}{a^2}\sum_\mu \sin^2(p_\mu a) = 0. \tag{2.51}$$

Obviously, there is a physical solution $\hat{p}_\mu$, which corresponds to the true one-particle state in the continuum theory. At the same time, there are other solutions whose components are partly or fully replaced by $\hat{p}_\mu \pm \pi/a$ due to the periodicity of $\sin(x)$. By considering the fact that each components are restricted to an interval $(-\pi/a, \pi/a]$ by the lattice regularization, we can conclude that there exist 15 additional solutions. Such unphysical one-particle states are called doublers, and they always appear as long as the simulations are performed with a non-zero lattice spacing. This difficulty is called the doubling problem.

Nielsen and Ninomiya prove that the doubling problem always occurs when the lattice fermion action satisfies the following properties[51–53]:

- Translational invariance
- Hermiticity

- Locality
- Chiral symmetry
- Fermion bilinear

Those conditions are automatically satisfied when one naively applies the lattice regularization to the continuum fermion action. Therefore, one needs some modifications to avoid the doubling problem. Here we introduce one of the lattice fermion actions free from the doubling problem called the Wilson fermion action.

The Wilson fermion action is defined as,

$$\begin{aligned} S_{\text{Wilson}} = a^4 \sum_{n\in\Lambda} \bar{\psi}^{(f)}(n) \left(\sum_{\mu=1}^{4} \gamma_\mu \frac{U_\mu(n)\psi^{(f)}(n+\hat{\mu}) - U_\mu^\dagger(n-\hat{\mu})\psi^{(f)}(n-\hat{\mu})}{2a} + m^{(f)}\psi^{(f)}(n) \right) \\ + \bar{\psi}^{(f)}(n) \sum_{\mu=1}^{4} \frac{2\psi^{(f)}(n) - U_\mu\psi^{(f)}(n+\hat{\mu}) - U_\mu^\dagger(n-\hat{\mu})\psi^{(f)}(n-\hat{\mu})}{2a}. \end{aligned} \tag{2.52}$$

The first row is the naive lattice fermion action introduced before, and the second row is an additional term called the Wilson term. This term corresponds to $-\frac{a}{2}\bar{\psi}D^2\psi$ in the continuum theory and disappears as $a \to 0$. Since the Wilson term explicitly breaks the chiral symmetry, we can avoid the doubling problem. As before, let us investigate one-particle states in the free case ($U \equiv \mathbf{1}$). $\tilde{D}(p)$ for the free Wilson fermion is given as,

$$\tilde{D}(p) = \sum_\mu \frac{i}{a}\gamma_\mu \sin(p_\mu a) + m\mathbf{1}_{\text{spinor}} + \underline{\frac{1}{a}\sum_\mu (1-\cos(p_\mu a))\mathbf{1}_{\text{spinor}}}. \tag{2.53}$$

The underlined part comes from the Wilson term. It gives different contributions depending on the solution of $\tilde{D}(p) = 0$ as

$$\frac{1}{a}\sum_\mu (1-\cos(p_\mu a)) \to \begin{cases} 0 + \mathcal{O}(a) & (\text{physical pole}) \\ \frac{2n}{a} + \mathcal{O}(a) & (\text{doubler}), \end{cases} \tag{2.54}$$

where n is the number of π/a which appears in the solution p_μ. As a result, doubler solutions correspond to particles with masses of $m + \frac{2n}{a}$. Such particles are decoupled in the continuum limit since they become infinitely heavy, therefore only the physical particle remains.

Finally, we introduce a dimensionless representation of the Wilson fermion action, which is useful for actual numerical calculations.

$$S_{\text{Wilson}} = \sum_{n,m\in\Lambda} \bar{\psi}'(n) D(n|m) \psi'(m), \tag{2.55}$$

$$D(n|m) = (ma+4)\left[\mathbf{1}_{\text{spinor}}\mathbf{1}_{\text{color}}\delta_{n,m} - \kappa\sum_{\mu=\pm1}^{\pm4}\frac{1}{2}(\mathbf{1}_{\text{spinor}}-\gamma_\mu)U_\mu(n)\delta_{n+\hat{\mu},m}\right], \tag{2.56}$$

where $\gamma_{-\mu} \equiv -\gamma_\mu$ and $\bar{\psi}' = a^{3/2}\bar{\psi}$, $\psi' = a^{3/2}\psi$. κ is a dimenson-less paremeter called "hopping parameter", which is related to the fermion mass as $\kappa = 1/2(ma+4)$. An overall factor $(ma+4)$ can be absorbed by the fermion fields. By combining it with the gauge action (2.36), we can perform lattice QCD simulations. Input parameters of the simulations are the inverse coupling β and the hopping parameter κ. In the rest of this thesis, we describe dimensionful quantities in the lattice unit (in other words, dimensionless representation using lattice spacing), unless otherwise stated.

2.1.4 Improvement of lattice actions

Practically, available lattice spacings a for the continuum limit are at most a few values, so it is important to remove the discretization errors as much as possible. The ambiguity of the addition of terms irrelevant to the continuum limit can be utilized for this purpose. Several improved lattice actions have been proposed until now, and here we introduce the Wilson-clover fermion action[54] and Iwasaki gauge action[55] employed in our study.

The Wilson-clover action is defined as,

$$S_F = S_{\text{Wilson}} + c_{\text{SW}}a^5\sum_{n\in\Lambda}\sum_{\mu<\nu}\bar{\psi}(n)\frac{1}{2}\sigma_{\mu\nu}\hat{F}_{\mu\nu}(n)\psi(n), \tag{2.57}$$

where S_{Wilson} is the Wilson fermion action introduced in the previous section and c_{SW} is a tunable parameter to remove a leading $\mathcal{O}(a)$ discretization error. In this study, we use a non-perturbatively determined value of c_{SW}. We do not discuss the details of the tuning process further.

The Iwasaki gauge action [55] is a gauge action consisting of not only the plaquettes but also 1×2 rectangular loops,

$$S_G = \frac{2}{g^2}\sum_{n\in\Lambda}\sum_{\mu<\nu}\left(w_{n,\mu\nu}\text{Re tr}(\mathbf{1}-U_{\mu\nu}(n)) + v_{n,\mu\nu}\text{Re tr}(\mathbf{1}-U^{(1\times2)}_{\mu\nu}(n))\right), \tag{2.58}$$

where $U^{(1\times2)}_{\mu\nu}(n)$ is a 1×2 rectangular loop on a $\mu\nu$ plane, and w, v are tunable parameter to improve the scaling behavior on a. In Refs. [56, 57], it is found that this action can avoid an unphysical first-order phase transition at zero-temparature observed in the plaquette action.

2.1.5 Path integral quantization

Now it is time to discuss the path integral quantization of the lattice QCD. The partition function Z is defined as

$$Z = \int \mathcal{D}[\psi, \bar{\psi}, U_\mu] e^{-S_E} \tag{2.59}$$

$$S_E = S_F + S_G \tag{2.60}$$

$$\mathcal{D}[\psi, \bar{\psi}, U_\mu] = \prod_{n \in \Lambda, \mu} d\psi(n) d\bar{\psi}(n) dU_\mu(n). \tag{2.61}$$

The fermion integrals are Grassmann integrals and integrals of the link variables are defined by the Haar measure of SU(3). Both kinds of integrals are normalized to unity. Furthermore, the integrand has an exponentially suppressing factor e^{-S_E}, therefore the whole integral is well-defined. The vacuum expectation value of a certain operator $\mathcal{O}$ is defined as

$$\langle \mathcal{O} \rangle = \frac{1}{Z} \int \mathcal{D}[\psi, \bar{\psi}, U_\mu] \mathcal{O}[\psi, \bar{\psi}, U_\mu] e^{-S_E}. \tag{2.62}$$

2.2 Calculation of correlation functions

To extract physical quantities such as hadron masses, one needs to calculate correlation functions corresponding to the target quantities in lattice QCD. In this section, we discuss the procedure of those calculations step by step.

2.2.1 Integral of fermions

Integrals of fermions can be performed analytically using the Wick contraction formula,

$$\int \prod_{k=1}^{N} d\eta_k d\bar{\eta}_k \eta_{i_1} \bar{\eta}_{j_1} ... \eta_{i_n} \bar{\eta}_{j_n} e^{\bar{\eta}_l M_{lm} \eta_m} = (-)^n \det(M) \sum_{P(1,...,n)} \mathrm{sign}(P) (M^{-1})_{i_1 j_{P_1}} ... (M^{-1})_{i_n j_{P_n}}, \tag{2.63}$$

where $\eta_k, \bar{\eta}_k$ are Grassmann variables, M is a matrix of $N \times N$, $P(1, ..., n) = (P_1, ..., P_n)$ is permutations of indices $(1, ..., n)$ with a sign of $\mathrm{sign}(P)$. In lattice QCD, $\eta, \bar{\eta}$ and M correspond to the quark fields $\psi, \bar{\psi}$ and the Dirac operator $-D(n|m)$, respectively. After the integration of the fermion fields, correlation functions typically shape into the following form:

$$\langle \mathcal{O} \rangle = \frac{1}{Z} \int dU \prod_f \det(D^{(f)}(U)) f_\mathcal{O}(U) e^{-S_G(U)} \equiv \langle f_\mathcal{O}(U) \rangle_{\text{gauge}}, \tag{2.64}$$

where $f_\mathcal{O}(U)$ is a function of the link variable derived from the Wick contraction and typically something like

$$f_\mathcal{O}(U) = \mathrm{tr} \left[D^{-1}(U) \Gamma D^{-1}(U) \cdots \right] + \cdots, \tag{2.65}$$

where a trace is taken in the color and spinor indices, Γ is a product of gamma matrices, and D^{-1} is a quark propagator, an inverse matrix of the Dirac operator.

2.2.2 Integral of link variables

Although the path integral after the Wick contraction is a multi-dimensional integral of the link variables, its direct calculation is still impossible in practice. Fortunately, the structure of the integral is an expectation value of $f_{\mathcal{O}}(U)$ under the probabilistic distribution,

$$P(U) = \frac{\prod_f \det(D^{(f)}(U))e^{-S_G(U)}}{Z}, \tag{2.66}$$

and we can apply the Markov chain Monte Carlo (MCMC) method to estimate the expectation value. The integral can be estimated by the mean value of Monte Carlo samples U_i generated from $P(U)$ as

$$\langle f_{\mathcal{O}}(U)\rangle_{\text{gauge}} = \int dU P(U) f_{\mathcal{O}}(U) \approx \frac{1}{N}\sum_{i=1}^{N} f_{\mathcal{O}}(U_i), \tag{2.67}$$

up to the statistical error due to the finite number of samples. In modern lattice simulations with dynamical quarks, the hybrid Monte Carlo (HMC) algorithm, in which samples are updated by a molecular dynamics evolution, is commonly employed to achieve both good acceptance and small correlations between samples. Lattice QCD simulations are performed in accordance with this idea unless there is the so-called sign problem (the sign problem is also one of the hot topics in the lattice QCD community, but we do not discuss it in this thesis).

2.2.3 Error estimation

The estimation of the statistical error is inevitable in lattice QCD simulation. In the most simple case where the statistical samples are totally independent, we can estimate the error from the standard deviation,

$$\delta\langle\mathcal{O}\rangle = \sqrt{\frac{1}{N(N-1)}\sum_i (\mathcal{O}_i - \langle\mathcal{O}\rangle)^2}, \tag{2.68}$$

and for a function of the statistical variables, we can apply the formula for the error propagation,

$$\delta\langle f(\{\mathcal{O}_n\})\rangle = \sqrt{\sum_n \langle\frac{\partial f}{\partial \mathcal{O}_n}\rangle^2 \delta\langle\mathcal{O}_n\rangle^2}. \tag{2.69}$$

However, the samples generated from the Monte Carlo method generally have correlations with each other and the formulae above cannot be applied. Furthermore, the error propagation may give wrong error estimations for complicated functions. One of the error estimation methods we can apply to such cases is the jackknife method, which is commonly used in lattice QCD simulations. We introduce the jackknife method with bin-size n here.

Let us consider the estimation of the expectation value of $f(\mathcal{O})$ from N samples of $\mathcal{O}$, $\{\mathcal{O}_1, ..., \mathcal{O}_N\}$. To make effectively independent samples, we first divide N samples into $N_n \equiv N/n$ small bins, and calculate N_n different mean values by excluding one of the bins as

$$O_a = \frac{1}{N-n} \sum_{i \notin I_a} \mathcal{O}_i, \ (a = 1, ..., N_n), \tag{2.70}$$

where I_a is a set of sample indices consist of ath bin. N_n samples $\{O_a\}$ are called jackknife samples. Then we can estimate a mean value and statistical error by

$$\langle f(\mathcal{O}) \rangle = \frac{1}{N_n} \sum_{a=1}^{N_n} f(O_a) \tag{2.71}$$

$$\delta \langle f(\mathcal{O}) \rangle = \sqrt{\frac{(N_n - 1)}{N_n} \sum_{a=1}^{N_n} (f(O_a) - \langle f(\mathcal{O}) \rangle)^2}. \tag{2.72}$$

This formulae are identical to the standard treatment when $f(\mathcal{O}) = \mathcal{O}$ and bin-size = 1.

The bin-size n is determined as follows. If we apply the jackknife method for correlated samples, the jackknife error (2.72) converges towards a certain value with an increase of the bin-size. This is because the bin-size becomes large enough to regard the bins as statistically independent samples. Therefore the converged error gives a valid estimation for the correlated data, and the bin-size n can be chosen from values where the error converges.

2.2.4 Flow of numerical simulations in lattice QCD

Here we summarize a procedure of numerical simulations in lattice QCD for the convenience of readers:

1. Generate gauge configurations $\{U_0, U_1, \cdots U_N\}$ by the Monte Carlo simulation based on $P(U)$.
2. Define the target correlation function and specify $f_{\mathcal{O}}(U)$ by the Wick contraction.
3. Calculate D^{-1} and estimate $f_{\mathcal{O}}(U)$ for each configurations.
4. Estimate the target correlation function and corresponding physical observables statistically using, for instance, the jackknife method.

Basically, the first and third steps require a lot of computational resources, and we perform these calculations on supercomputers. To avoid unnecessary computational costs, it is common to store configurations and reuse them in other simulations once they are generated. Some configurations generated before are open to the public. We employ such public configurations in our calculations.

2.3 Hadron masses from lattice QCD

In the closing part of this chapter, we discuss a typical application of lattice QCD, namely the extraction of hadron masses. First, we show how to extract hadron masses from lattice QCD simulations. Then, we discuss the quark smearing, which is useful to reduce unnecessary contamination in practice.

2.3.1 Extraction of hadron masses

Let us consider a two-point correlation function (or propagator) of the target hadron,

$$C(t) = \langle O(t+t_0)\bar{O}(t_0)\rangle, \tag{2.73}$$

where $O(t), \bar{O}(t)$ are the operator which has the same quantum numbers (total spin, total momentum, isospin, etc.) as the target state and its conjugate operator, respectively. By inserting the completeness relation $\mathbf{1} = \sum_n |n\rangle\langle n|$ in between the operators, we obtain

$$\begin{aligned}
\langle O(t+t_0)\bar{O}(t_0)\rangle &= \sum_n \langle O(t+t_0)|n\rangle\langle n|\bar{O}(t_0)\rangle & (2.74)\\
&= \sum_n \langle O(t+t_0)|O,n\rangle\langle O,n|\bar{O}(t_0)\rangle & (2.75)\\
&= \sum_n \langle O(0)|O,n\rangle\langle O,n|\bar{O}(0)\rangle e^{-E_n t}, & (2.76)
\end{aligned}$$

where $|O,n\rangle$ and E_n are an nth energy eigenstate and its energy eigenvalue with the same quantum numbers as O. When t is sufficiently large, excited states are exponentially suppressed and only the ground state survives,

$$C(t) \to |\langle 0|O(0)|O,0\rangle|^2 e^{-E_0 t} \ (t\to\infty). \tag{2.77}$$

Therefore we can extract the ground state energy from the time dependence of $C(t)$ in a large t region. If we choose the hadron operator projected onto zero momentum, $O(\mathbf{p}=\mathbf{0},t) \equiv \sum_{\mathbf{x}} O(\mathbf{x},t)$, we can obtain a target hadron mass as the ground state energy. For the extraction of the hadron mass from the exponential time dependence e^{-mt}, one basically employs exponential fit of the 2pt function,

$$C(t) = Ce^{-mt}, \tag{2.78}$$

where C and m is fit parameters, or with the periodic boundary condition for time direction, cosh-shape fit

$$C(t) = C\cosh(m(t-T/2)), \tag{2.79}$$

where T is a length of the time direction, is employed. A range of fit is determined by referring the time dependence of the effective mass,

$$m_{\text{eff}}(t) \equiv -\log\left(\frac{C(t+1)}{C(t)}\right). \tag{2.80}$$

This quantity is equivalent to the hadron mass if the correlation function is dominated by the ground state. Therefore, the time interval where $m_{\text{eff}}(t)$ shows a plateau behavior is suitable for the fit.

The choice of the hadron operator O is arbitrary in general, but the common choice is a local operator based on the quark model. For instance, the pion operators are given as,

$$\pi^+(\mathbf{x},t) = \bar{d}(\mathbf{x},t)\gamma_5 u(\mathbf{x},t) \tag{2.81}$$

$$\pi^-(\mathbf{x},t) = \bar{u}(\mathbf{x},t)\gamma_5 d(\mathbf{x},t) \tag{2.82}$$

$$\pi^0(\mathbf{x},t) = \frac{1}{\sqrt{2}}\left(\bar{u}(\mathbf{x},t)\gamma_5 u(\mathbf{x},t) - \bar{d}(\mathbf{x},t)\gamma_5 d(\mathbf{x},t)\right), \tag{2.83}$$

where u, d are the up and down quark fields, respectively.

2.3.2 Quark smearing

The quark smearing is a way to reduce excited-state contamination in correlation functions, which is beneficial for precise determinations of hadron masses. In the quark smearing, we replace the local quark field $\psi, \bar{\psi}$ by the smeared quark fields $\psi_s, \bar{\psi}_s$ defined as

$$\psi_{\alpha,a}(\mathbf{x},t) \to \psi_{s,(\alpha,a)}(\mathbf{x},t) = \sum_{\mathbf{y},b,\beta} S^*_{(\alpha,a)(\beta,b)}(\mathbf{x};\mathbf{y})\psi_{(\beta,b)}(\mathbf{y},t), \tag{2.84}$$

$$\bar{\psi}_{\alpha,a}(\mathbf{x},t) \to \bar{\psi}_{s,(\alpha,a)}(\mathbf{x},t) = \sum_{\mathbf{y},b,\beta} \bar{\psi}_{(\beta,b)}(\mathbf{y},t) S_{(\beta,b)(\alpha,a)}(\mathbf{y};\mathbf{x}). \tag{2.85}$$

S is called a smearing function and several types have ever been proposed. The purpose of the smearing is to give quark fields some spatial extent as wave packets, and it allows the smeared operators to overlap physical states strongly. Here we introduce some typical examples of the smearing.

- Exponential smearing (Tsukuba-type)
  Exponential smearing (Tsukuba-type)[58, 59] is the smearing with exponential smearing function as

$$S_{(\alpha,a)(\beta,b)}(\mathbf{x};\mathbf{y}) = \delta_{\alpha\beta}\delta_{ab} f\left(|\mathbf{x}-\mathbf{y}|\right) \tag{2.86}$$

$$f\left(|\mathbf{x}-\mathbf{y}|\right) = \begin{cases} Ae^{-B|\mathbf{x}-\mathbf{y}|} & (\ 0 < |\mathbf{x}-\mathbf{y}| < (L-1)/2\ ) \\ 1 & (\ |\mathbf{x}-\mathbf{y}| = 0\ ) \\ 0 & (\ |\mathbf{x}-\mathbf{y}| \geq (L-1)/2\ ) \end{cases} \tag{2.87}$$

Tunable parameters are A and B. Since the smearing function do not include any link variable, it is not a gauge invariant operation. We need some gauge fixing to use it.

- Jacobi smearing
  In the Jacobi smearing[60], the smearing functions is defined as follows:

$$S_{(\alpha,a)(\beta,b)}(\mathbf{x};\mathbf{y}) = \delta_{\alpha\beta} J_{ab}(\mathbf{x};\mathbf{y}), \tag{2.88}$$

$$J_{ab}(\mathbf{x};\mathbf{y}) = \sum_{n=0}^{N-1} \kappa^n H^n_{ab}(\mathbf{x};\mathbf{y}), \tag{2.89}$$

where the function H is

$$H(\mathbf{x};\mathbf{y}) = \sum_{i=1}^{3} \left(U_j(\mathbf{x},t)\delta_{\mathbf{x}+a\hat{\mathbf{j}},\mathbf{y}} + U_j^\dagger(\mathbf{x}-a\hat{\mathbf{j}},\mathbf{t})\delta_{\mathbf{x}-\mathbf{a}\hat{\mathbf{j}},\mathbf{y}} \right). \tag{2.90}$$

Tunable parameters are κ and N. In contrast to the exponential smearing, it does not need any gauge fixing since the link variable is inserted.

Chapter 3

Hadron-hadron scattering from lattice QCD

In this chapter, we discuss how to analyze hadron-hadron scattering from lattice QCD. At present, there are mainly two methods to study hadron interaction from lattice QCD, the Lüshcer's method and the HAL QCD method. Both methods are based on the fundamental quantity called the Nambu–Bethe–Salpeter (NBS) wave function. In this study, we employ the HAL QCD method to study hadron interactions. The enlargement of the applicability of the HAL QCD method is beneficial since it is relatively less-biased than the Lüscher's method and brings the interaction potential directly.

This chapter is organized as follows. First, we introduce a general feature of the scattering S-matrix, a fundamental quantity to analyze scattering processes. We then introduce the Nambu–Bethe–Salpeter (NBS) wave function and its features. After that, we introduce the basic formulation of the HAL QCD method in detail. We discuss not only the conventional center-of-mass frame calculation but also its extension to the laboratory frame. Finally, we briefly introduce the Lüscher's finite volume method.

3.1 Unitarity of S-matrix and scattering phase shift

A fundamental quantity to describe scatterings of quantum systems is the S-matrix. The S-matrix is a unitary operator, which satisfies

$$SS^\dagger = S^\dagger S = \mathbf{1}. \tag{3.1}$$

Here we consider the T-matrix defined as $S = \mathbf{1} + iT$, which describe an interacting part of the scattering processes. By the unitarity relation (3.1), we obtain the following formula on the T-matrix,

$$\langle f|T|i\rangle - \langle f|T^\dagger|i\rangle = i\langle f|TT^\dagger|i\rangle = i\sum_n \langle f|T|n\rangle\langle n|T^\dagger|i\rangle, \tag{3.2}$$

where $|i\rangle, |f\rangle$ are initial and final asymptotic states we consider and at the second equality we insert a completeness relation, $\mathbf{1} = \sum_n |n\rangle\langle n|$. In the following, we consider an elastic scattering of two distinguishable scalar particles with the same mass m and consider Minkowski spacetime. The asymptotic states in the center-of-mass (CM) frame are given as,

$$|i\rangle = |k_1, k_2\rangle \tag{3.3}$$
$$|f\rangle = |p_1, p_2\rangle, \tag{3.4}$$

where four-momenta k_i, p_i $(i = 1, 2)$ are on-shell as

$$k_1 = (\sqrt{\mathbf{k}^2 + m^2}, \mathbf{k}) \tag{3.5}$$
$$k_2 = (\sqrt{\mathbf{k}^2 + m^2}, -\mathbf{k}) \tag{3.6}$$
$$p_1 = (\sqrt{\mathbf{p}^2 + m^2}, \mathbf{p}) \tag{3.7}$$
$$p_2 = (\sqrt{\mathbf{p}^2 + m^2}, -\mathbf{p}). \tag{3.8}$$

Since the system has a translational invariance, the matrix element of the T-matrix behaves as

$$\langle p_1, p_2|T|k_1, k_2\rangle = T(\mathbf{p}, \mathbf{k})(2\pi)^4\delta^4(p_1 + p_2 - k_1 - k_2). \tag{3.9}$$

Furthermore, we assume there is no stable bound states and we can ignore inelastic scattering. In that case, elastic two-particle states only contribute to the completeness relation, and the right-hand side of (3.2) becomes

$$\begin{aligned}
& i \sum_n \langle f|T|n\rangle\langle n|T^\dagger|i\rangle \\
= \; & i \int \frac{d^3\mathbf{q_1} d^3\mathbf{q_2}}{(2\pi)^6 2E_{q_1} 2E_{q_2}} \langle p_1, p_2|T|q_1, q_2\rangle\langle q_1, q_2|T^\dagger|k_1, k_2\rangle \\
= \; & i \int \frac{d^3\mathbf{q_1} d^3\mathbf{q_2}}{(2\pi)^6 2E_{q_1} 2E_{q_2}} T^*(\mathbf{q_1}, \mathbf{q_2}, \mathbf{p}) T(\mathbf{q_1}, \mathbf{q_2}, \mathbf{k})(2\pi)^8\delta^4(q_1 + q_2 - k_1 - k_2)\delta^4(p_1 + p_2 - q_1 - q_2) \\
= \; & \underline{(2\pi)^4\delta^4(p_1 + p_2 - k_1 - k_2)} \\
& \qquad \times i \int \frac{d^3\mathbf{q_1} d^3\mathbf{q_2}}{(2\pi)^2 2E_{q_1} 2E_{q_2}} T^*(\mathbf{q_1}, \mathbf{q_2}, \mathbf{p}) T(\mathbf{q_1}, \mathbf{q_2}, \mathbf{k})\delta^4(q_1 + q_2 - k_1 - k_2).
\end{aligned} \tag{3.10}$$

We remove the underlined part since it is a common factor of the both sides of (3.2). A remaining integral can be partly performed thanks to the delta function as

$$\begin{aligned} & i \int \frac{d^3\mathbf{q_1} d^3\mathbf{q_2}}{(2\pi)^2 2E_{q_1} 2E_{q_2}} T^*(\mathbf{q_1},\mathbf{q_2},\mathbf{p}) T(\mathbf{q_1},\mathbf{q_2},\mathbf{k}) \delta^4(q_1+q_2-k_1-k_2) \\ = \; & i \int \frac{d^3\mathbf{q_1} d^3\mathbf{q_2}}{(2\pi)^2 2E_{q_1} 2E_{q_2}} T^*(\mathbf{q_1},\mathbf{q_2},\mathbf{p}) T(\mathbf{q_1},\mathbf{q_2},\mathbf{k}) \delta(E_{q_1}+E_{q_2}-2E_k) \delta^3(\mathbf{q_1}+\mathbf{q_2}) \\ = \; & i \int \frac{d^3\mathbf{q}}{(2\pi)^2 (2E_q)^2} T^*(\mathbf{q},\mathbf{p}) T(\mathbf{q},\mathbf{k}) \delta(2E_q - 2E_k) \\ = \; & i \frac{1}{16\pi^2} \int d\Omega_{\mathbf{q}} \int \frac{q^2 dq}{E_q^2} T^*(\mathbf{q},\mathbf{p}) T(\mathbf{q},\mathbf{k}) \frac{E_k}{2k} \delta(q-k) \; (q=|\mathbf{q}|, k=|\mathbf{k}|) \\ = \; & \frac{ik}{32\pi^2 E_k} \int d\Omega_{\mathbf{q}} T^*(\mathbf{q},\mathbf{p}) T(\mathbf{q},\mathbf{k}), \end{aligned} \tag{3.11}$$

where we use a formula of $\delta(f(x)-f(a)) = 1/|f'(a)|\delta(x-a)$ at the third equality. In summary, we obtain a formula on $T(\mathbf{p},\mathbf{k})$ as

$$T(\mathbf{p},\mathbf{k}) - T^*(\mathbf{k},\mathbf{p}) = \frac{ik}{32\pi^2 E_k} \int d\Omega_{\mathbf{q}} T^*(\mathbf{q},\mathbf{p}) T(\mathbf{q},\mathbf{k}), \tag{3.12}$$

with the on-shell condition $|\mathbf{q}| = |\mathbf{k}| = |\mathbf{p}|$. To see behaviors of the partial wave T-matrix, we apply the partial wave decomposition to $T(\mathbf{p},\mathbf{k})$ as

$$T(\mathbf{p},\mathbf{k}) = 4\pi \sum_{l=0}^{\infty} \sum_{m=-l}^{l} T_l(p,k) Y_{lm}(\Omega_{\mathbf{p}}) \bar{Y}_{lm}(\Omega_{\mathbf{k}}). \tag{3.13}$$

Together with the orthogonality of the spherical harmonics,

$$\int d\Omega Y_{lm}(\Omega) \bar{Y}_{l'm'}(\Omega) = \delta_{ll'}\delta_{mm'}, \tag{3.14}$$

we can perform the angular integral of (3.12) as

$$\begin{aligned} & \frac{ik}{32\pi^2 E_k} (4\pi)^2 \sum_{l,m} \sum_{l',m'} \int d\Omega_{\mathbf{q}} T_l^*(q,p) Y_{lm}(\Omega_{\mathbf{p}}) \bar{Y}_{lm}(\Omega_{\mathbf{q}}) T_{l'}(q,k) Y_{l'm'}(\Omega_{\mathbf{q}}) \bar{Y}_{l'm'}(\Omega_{\mathbf{k}}) \\ = \; & 4\pi \sum_{l,m} \frac{ik}{8\pi E_k} T_l^*(k,k) T_l(k,k) Y_{lm}(\Omega_{\mathbf{p}}) \bar{Y}_{lm}(\Omega_{\mathbf{k}}). \end{aligned} \tag{3.15}$$

Therefore we obtain a formula of the partial wave T-matrix from (3.12), (3.13), and (3.14),

$$T_l(k,k) - T_l^*(k,k) = \frac{ik}{8\pi E_k} T_l^*(k,k) T_l(k,k). \tag{3.16}$$

This formula is satisfied with the parametrization of

$$T_l(k,k) = \frac{16\pi E_k}{k}\sin(\delta_l(k))e^{i\delta_l(k)}, \tag{3.17}$$

where $\delta_l(k)$ is a real parameter depending on l and k. This result means that the whole information of the elastic scattering is summarized to the parameter $\delta_l(k)$, which is called the scattering phase shift. A main task to analyze the particle scattering is, therefore, to extract information of $\delta_l(k)$ somehow.

3.2 Nambu–Bethe–Salpeter wave function

In non-relativistic quantum mechanics, the scattering phase shift appears as a phase of an asymptotic wave function. On the other hand, in quantum field theory, the Nambu–Bethe–Salpeter (NBS) wave function contains the information of the scattering phase shift. Here we discuss the definition of the NBS wave function and derive its asymptotic behavior.

3.2.1 Definition

Let us consider an elastic scattering of two distinguishable scalar particles with the same mass m in Minkowski spacetime. The NBS wave function for this system is defined as

$$\psi_{k_1,k_2}(x_1,x_2) = \langle 0|\mathrm{T}\{\varphi_1(x_1)\varphi_2(x_2)\}|k_1,k_2\rangle_{\mathrm{in}}, \tag{3.18}$$

where $\varphi_i(x)$ is scalar field operators ($i = 1,2$ is an identifier of two particles) and $|k_1,k_2\rangle_{\mathrm{in}}$ is an asymptotic in-state of two particles with four-momenta k_1 and k_2. In general, the NBS wave function can be defined in any frame of reference, but here we are interested in one in the center-of-mass frame since it is directly related to the scattering phase shift. On the other hand, the NBS wave function in the laboratory frame also play an important role in practice, as will be discussed later. The field operators and asymptotic states are transformed under Lorentz transformation as

$$U(\Lambda)\varphi_i(x)U^{-1}(\Lambda) = \varphi_i(x') \tag{3.19}$$

$$U(\Lambda)|k_1,k_2\rangle_{\mathrm{in}} = |k_1',k_2'\rangle_{\mathrm{in}}, \tag{3.20}$$

where $U(\Lambda)$ is a unitary operator which implements Lorentz transformation on the states and prime symbols represent transformed objects, for example, $x'^{\mu} = \Lambda^{\mu}{}_{\nu}x^{\nu}$. Using eqs. (3.18), (3.19), and (3.20), we can derive the relation between two NBS wave functions in different frames as

$$\psi_{k_1,k_2}(x_1,x_2) = \psi_{k_1',k_2'}(x_1',x_2'). \tag{3.21}$$

Furthermore, the relation $\varphi(x) = e^{iP\cdot x}\varphi(0)e^{-iP\cdot x}$ (where P is the energy-momentum operator and $P\cdot x = \eta_{\mu\nu}P^\mu x^\nu$) implies that the NBS wave function is factorized into a center–of–mass plane wave and a relative wave function as

$$\psi_{k_1,k_2}(x_1,x_2) = \phi_{k_1,k_2}(x)e^{-iWX^0+i\mathbf{P}\cdot\mathbf{X}}, \tag{3.22}$$

where $W = \sqrt{\mathbf{k}_1^2+m^2}+\sqrt{\mathbf{k}_2^2+m^2}$ and $\mathbf{P} = \mathbf{k}_1+\mathbf{k}_2$ are the total energy and momentum, respectively. The center–of–mass and relative coordinates (X, x) are defined as

$$X \equiv \frac{x_1+x_2}{2}, \quad x \equiv x_1 - x_2. \tag{3.23}$$

Since $\eta_{\mu\nu}P^\mu X^\nu = WX^0 - \mathbf{P}\cdot\mathbf{X}$ is Lorentz invariant, eqs. (3.21) and (3.22) give a relation between relative wave functions in different frames as

$$\phi_{k_1,k_2}(x) = \phi_{k_1',k_2'}(x'). \tag{3.24}$$

3.2.2 Asymptotic behavior of the relative NBS wave function in the center-of-mass frame

In the following, we derive an asymptotic form of the relative NBS wave function in the center-of-mass frame,

$$\phi_{\mathbf{k}}(\mathbf{x},t) = \langle 0|\mathrm{T}\{\varphi_1(\mathbf{x}/2,t/2)\varphi_2(-\mathbf{x}/2,-t/2)\}|\mathbf{k},-\mathbf{k}\rangle_{\mathrm{in}}. \tag{3.25}$$

First, we insert a complete set of the asymptotic out states,

$$\mathbf{1} = |0\rangle\langle 0| + \sum_i \int \frac{d^3\mathbf{p}}{(2\pi)^3 2E_p}|\mathbf{p},i\rangle_{\mathrm{out}\ \mathrm{out}}\langle\mathbf{p},i| + (\text{multiparticle states}), \tag{3.26}$$

into the NBS wave function. The elastic part is given as

$$\phi^{\mathrm{elas.}}_{\mathbf{k}}(\mathbf{x},t) = \sum_i \int \frac{d^3\mathbf{p}}{(2\pi)^3 2E_p}\langle 0|\varphi_1(\mathbf{x}/2,t/2)|\mathbf{p},i\rangle_{\mathrm{out}\ \mathrm{out}}\langle\mathbf{p},i|\varphi_2(-\mathbf{x}/2,-t/2)|\mathbf{k},-\mathbf{k}\rangle_{\mathrm{in}}. \tag{3.27}$$

The first matrix element behaves as

$$\langle 0|\varphi_i(\mathbf{x}/2,t/2)|\mathbf{p},j\rangle_{\mathrm{out}} = \delta_{ij}\sqrt{Z}e^{i\mathbf{p}\cdot\mathbf{x}/2-iE_pt/2}, \tag{3.28}$$

where Z is a renormalization factor of the field φ_i, therefore

$$\phi^{\mathrm{elas.}}_{\mathbf{k}}(\mathbf{x},t) = \sqrt{Z}\int \frac{d^3\mathbf{p}}{(2\pi)^3 2E_p}e^{i\mathbf{p}\cdot\mathbf{x}/2-iE_pt/2}\ {}_{\mathrm{out}}\langle\mathbf{p},1|\varphi_2(-\mathbf{x}/2,-t/2)|\mathbf{k},-\mathbf{k}\rangle_{\mathrm{in}}. \tag{3.29}$$

The LSZ reduction formula,

$$
\begin{aligned}
a_{out,i,\mathbf{p}}\mathrm{T}(\mathcal{O}) - \mathrm{T}(\mathcal{O})a_{in,i,\mathbf{p}} &= i(-p^2+m^2)\mathrm{T}(\varphi_i(p)\mathcal{O})/\sqrt{2E_p} && (3.30)\\
\mathrm{T}(\mathcal{O})a^\dagger_{in,i,\mathbf{p}} - a^\dagger_{out,i,\mathbf{p}}\mathrm{T}(\mathcal{O}) &= i(-p^2+m^2)\mathrm{T}(\varphi^\dagger_i(p)\mathcal{O})/\sqrt{2E_p} && (3.31)\\
\varphi_i(p) &= \int d^4x \frac{1}{\sqrt{Z}}\varphi_i(x)e^{ip\cdot x}, && (3.32)
\end{aligned}
$$

leads us to,

$$
\begin{aligned}
{}_{\mathrm{out}}\langle \mathbf{p},1|\varphi_2(-\mathbf{x}/2,-t/2)|\mathbf{k},-\mathbf{k}\rangle_{\mathrm{in}} = \sqrt{Z}(2\pi)^3 2E_k e^{+iE_kt/2}e^{+i\mathbf{k}\cdot\mathbf{x}/2}\delta(\mathbf{p}-\mathbf{k})\\
+\sqrt{Z}\frac{e^{+iq\cdot x/2}}{m^2-q^2-i\epsilon}\hat{T}(p,q,k,k),
\end{aligned}
\qquad (3.33)
$$

where $x=(t,\mathbf{x})$ and $q=(-E_p+2E_k,-\mathbf{p})$. $\hat{T}$ is a half off-shell T-matrix defined as

$$
\hat{T}(p,q,k,k) = i(-p^2+m^2)i(-q^2+m^2)G(p,q,k,k)i(-k^2+m^2)i(-k^2+m^2) \qquad (3.34)
$$

$$
iG(p,q,k,k)(2\pi)^4\delta^4(p+q-2k) = \langle 0|\varphi_1(p)\varphi_2(q)\varphi_1^\dagger(k)\varphi_2^\dagger(k)|0\rangle. \qquad (3.35)
$$

In summary, the elastic part of the relative NBS wave function behaves as

$$
\begin{aligned}
\phi^{\mathrm{elas.}}_{\mathbf{k}}(\mathbf{x},t) &= Z\left[e^{i\mathbf{k}\cdot\mathbf{r}} + \int \frac{d^3\mathbf{p}}{(2\pi)^3 2E_p}e^{i\mathbf{p}\cdot\mathbf{r}-i(E_p-E_k)t}\frac{\hat{T}(p,q,k_a,k_b)}{m^2-q^2-i\epsilon}\right]\\
&= Z\left[e^{i\mathbf{k}\cdot\mathbf{r}} + \int \frac{d^3\mathbf{p}}{(2\pi)^3}e^{i\mathbf{p}\cdot\mathbf{r}-i(E_p-E_k)t}\frac{E_p+E_k}{8E_pE_k}\frac{\hat{T}(p,q,k_a,k_b)}{|\mathbf{p}|^2-|\mathbf{k}|^2-i\epsilon}\right]\\
&= Z\left[e^{i\mathbf{k}\cdot\mathbf{r}} + \int \frac{d^3\mathbf{p}}{(2\pi)^3}e^{i\mathbf{p}\cdot\mathbf{r}-i(E_p-E_k)t}\frac{\hat{H}(\mathbf{p},\mathbf{k})}{|\mathbf{p}|^2-|\mathbf{k}|^2-i\epsilon}\right]. \qquad (3.36)
\end{aligned}
$$

In the last equality we define

$$
\hat{H}(\mathbf{p},\mathbf{k}) \equiv \frac{E_p+E_k}{8E_pE_k}\hat{T}, \qquad (3.37)
$$

and rewrite the integrand. In the following, we represent $p=|\mathbf{p}|, k=|\mathbf{k}|$ unless otherwise stated. Insert the partial wave decomposition,

$$
\begin{aligned}
\hat{H}(\mathbf{p},\mathbf{k}) &= (4\pi)\sum_{lm} H_l(p,k)Y_{lm}(\Omega_{\mathbf{p}})\bar{Y}_{lm}(\Omega_{\mathbf{k}}) && (3.38)\\
e^{i\mathbf{p}\cdot\mathbf{x}} &= (4\pi)\sum_{lm} i^l j_l(pr)Y_{lm}(\Omega_{\mathbf{x}})\bar{Y}_{lm}(\Omega_{\mathbf{p}}) && (3.39)\\
\phi^{\mathrm{elas.}}_{\mathbf{k}}(\mathbf{x},t) &= (4\pi)\sum_{lm} i^l\phi_l(k,r,t)Y_{lm}(\Omega_{\mathbf{x}})\bar{Y}_{lm}(\Omega_{\mathbf{k}}), && (3.40)
\end{aligned}
$$

and apply the orthogonality relation of the spherical harmonics, we obtain

$$\phi_l(k,r,t) = Z\left[j_l(kr) - \frac{1}{2\pi^2}\int_0^\infty p^2 dp \frac{H_l(p,k)j_l(pr)e^{-i(E_p-E_k)t}}{k^2-p^2+i\epsilon}\right]. \tag{3.41}$$

The integral in the second term can be estimated by the formula,

$$\int_0^\infty q^2 dq \frac{j_l(qr)}{k^2-q^2+i\epsilon}F_l(q) \approx -\frac{\pi k}{2}F_l(k)\left[n_l(kr)+ij_l(kr)\right] \ (r \gg 1), \tag{3.42}$$

where j_l and n_l are the spherical Bessel and Neumann function defined as

$$j_l(x) = (-x)^l\left(\frac{1}{x}\frac{d}{dx}\right)^l\left(\frac{\sin(x)}{x}\right) \tag{3.43}$$

$$n_l(x) = (-x)^l\left(\frac{1}{x}\frac{d}{dx}\right)^l\left(\frac{\cos(x)}{x}\right), \tag{3.44}$$

and $F_l(q)$ has a property as $F_l(-q) = (-1)^l F_l(q)$ and does not have any pole on a real axis. In our case, F_l is given as

$$F_l(p) = H_l(p,k)e^{-i(E_p-E_k)t}. \tag{3.45}$$

Since we consider the elastic scattering, there is no pole on the real axis. Furthermore, from the partial wave decomposition of $\hat{H}(\mathbf{q},\mathbf{k})$ and the property of the spherical harmonics $Y_{lm}(\Omega_{-\mathbf{q}}) = (-1)^l Y_{lm}(\Omega_{\mathbf{q}})$, we can show $H(-p,k) = (-1)^l H(p,k)$. Therefore, $F_l(-q) = (-1)^l F_l(q)$ is actually satisfied. Using the formula (3.42), partial wave NBS wave functions behave at a sufficiently large r as

$$\phi_l(k,r,t) \approx Z\left[j_l(kr) + \frac{1}{16\pi E_k}T_l(k,k)(n_l(kr)+ij_l(kr))\right]. \tag{3.46}$$

The parametrization of the partial wave T-matrix,

$$T_l(k,k) = \frac{16\pi E_k}{k}\sin(\delta_l(k))e^{i\delta_l(k)}, \tag{3.47}$$

and asymptotic behaviors of the spherical Bessel and Neumann functions at a sufficiently large r,

$$j_l(kr) \to \frac{\sin(kr-\frac{l\pi}{2})}{kr} \tag{3.48}$$

$$n_l(kr) \to \frac{\cos(kr-\frac{l\pi}{2})}{kr}, \tag{3.49}$$

finally leads to

$$\phi_l(k,r,t) \to Ze^{i\delta_l}\frac{\sin(kr-\frac{l\pi}{2}+\delta_l)}{kr}. \tag{3.50}$$

This form is the same as the asymptotic wave function in the non-relativistic quantum scattering. Accordingly, we can also show that the NBS wave function satisfies the Helmholtz equation in the asymptotic region as

$$(\nabla^2 + k^2)\phi_{\mathbf{k}}^{\text{elas.}}(\mathbf{x}, t) \to 0. \tag{3.51}$$

As a result, we can extract the scattering information $\delta_l(k)$ from the asymptotic NBS wave function as the non-relativistic scattering theory, although there is no non-relativistic approximation in our discussion. Incidentally, we haven't discussed the contribution from the inelastic part of (3.26), but it can be shown that they are small as long as we consider low-energy scatterings far below inelastic thresholds.

3.3 HAL QCD method

In this section we introduce the HAL QCD method[16–18] in details. The discussion in the last section reveals that the NBS wave function contains the scattering information in the same manner as the non-relativistic quantum scattering. The idea of the HAL QCD method is to reconstruct interaction potentials via the Schrödinger equation, starting from the NBS wave function.

3.3.1 Energy-independent non-local potential

We assume that the interaction of particles is short range, namely the interaction disappears at $r = R$. Since the NBS wave function asymptotically contains the scattering phase shift, we can expect that there exists an interaction potential with which the NBS wave function satisfies the Schrödinger-type equation,

$$\frac{1}{2\mu}(\nabla^2 + k^2)\phi_{\mathbf{k}}(\mathbf{x}, t) = \int d^3\mathbf{r} U_t(\mathbf{x}, \mathbf{x}')\phi_{\mathbf{k}}(\mathbf{x}', t), \tag{3.52}$$

where $\mu = m/2$ is a reduced mass of the system and U_t is the interaction potential. We note that here the relative time t is fixed and eq.(3.52) is understood as the time-independent Schrödinger equation. Inversely, the interaction potential can be reconstructed if we know whole set of the elastic NBS wave functions beforehand:

1. Define a kernel $\mathcal{K}_W$ by the known NBS wave functions as

$$\mathcal{K}_W(\mathbf{x}, t) \equiv \frac{1}{2\mu}(\nabla^2 + k^2)\phi_{\mathbf{k}}(\mathbf{x}, t) \ (W < W_{\text{th}}), \tag{3.53}$$

   where $k = |\mathbf{k}|$ and $W = 2\sqrt{k^2 + m^2}$, W_{th} is a threshold of an inelastic scattering. Since the NBS wave function satisfies the Helmholtz equation at large distances, this kernel goes to zero at $r > R$.

2. Next, define a metric $\mathcal{N}_{W,W'}$ as

$$\mathcal{N}_{W,W'}(t) \equiv \int d^3\mathbf{x}\phi^*_{\mathbf{k}}(\mathbf{x},t)\phi_{\mathbf{k}'}(\mathbf{x},t). \tag{3.54}$$

Generally speaking, this metric is not diagonal since the NBS wave functions are not orthogonal.

3. From these, we can reconstruct the energy-independent non-local potential as

$$U_t(\mathbf{x},\mathbf{x}') \equiv \sum_{W,W'}^{W_{th}} \mathcal{K}_W(\mathbf{x},t)\mathcal{N}^{-1}_{W,W'}(t)\phi^*_{\mathbf{k}'}(\mathbf{x}',t). \tag{3.55}$$

The subscription t represents a dependence on the relative time separation. The shape of the potential generally depends on how we define the NBS wave function (relative time separation, definition of the hadron operator, etc.) and we refer to it as "scheme dependence". By construction, this potential satisfies the Schrödinger equation (3.52),

$$\begin{aligned}
\int d^3\mathbf{x}' U_t(\mathbf{x},\mathbf{x}')\phi_{\mathbf{k}}(\mathbf{x}',t) &= \sum_{W',W''}^{W_{th}} \int d^3\mathbf{x}' \mathcal{K}_{W'}(\mathbf{x},t)\mathcal{N}^{-1}_{W',W''}(t)\phi^*_{\mathbf{k}''}(\mathbf{x}',t)\phi_{\mathbf{k}}(\mathbf{x}',t) \\
&= \sum_{W',W''}^{W_{th}} \mathcal{K}_{W'}(\mathbf{x},t)\mathcal{N}^{-1}_{W',W''}(t)\mathcal{N}_{W'',W}(t) \\
&= \mathcal{K}_W(\mathbf{x},t) \\
&= \frac{1}{2\mu}(\nabla^2 + k^2)\phi_{\mathbf{k}}(\mathbf{x},t).
\end{aligned} \tag{3.56}$$

The interaction potential is faithful to the scattering phase shift (and therefore to the S-matrix). Once we reconstruct the potential we can use it to calculate physical observables. The non-local potential generally depends on the scheme, but the physical observables are independent of it as long as the complete non-local potential is considered. Therefore, we can choose schemes convenient for the calculations of physical observables.

3.3.2 Derivative expansion of the non-local potential

The potential defined above can be calculated if we know all NBS wave functions below the inelastic threshold. In practice, however, it is impossible to reconstruct the complete non-local potential, since only discretized energy eigenstates can be accessed in lattice QCD. To determine the non-locality of the potential with restricted energy eigenstates, we employ a derivative expansion of the non-locality as

$$U(\mathbf{x},\mathbf{x}') = V(\mathbf{x},\nabla)\delta^3(\mathbf{x}-\mathbf{x}'). \tag{3.57}$$

In our study $V(\mathbf{x}, \nabla)$ is given as [1],

$$V(\mathbf{x}, \nabla) = V_0(\mathbf{x}) + V_2(\mathbf{x})\nabla^2 + O(\nabla^4). \tag{3.58}$$

We truncate this expansion at a sufficient order of expansion. In our study, we consider the effective leading order (LO) potential

$$V^{\mathrm{LO}}(\mathbf{x}, \nabla) = V_0^{\mathrm{LO}}(\mathbf{x}), \tag{3.59}$$

and the effective next-to-next-to-leading order ($\mathrm{N^2LO}$) potential,

$$V^{\mathrm{N^2LO}}(\mathbf{x}, \nabla) = V_0^{\mathrm{N^2LO}}(\mathbf{x}) + V_2^{\mathrm{N^2LO}}(\mathbf{x})\nabla^2. \tag{3.60}$$

The truncation introduces systematic uncertainty in the HAL QCD method. The physical observables can be affected by this truncation if the expansion is insufficient to reproduce the non-locality of the true potential. In general, we cannot know the extent of the non-locality beforehand, therefore it is better to study how physical observables depend on the truncation. Furthermore, the convergence of the derivative expansion depends on the scheme we choose. To utilize the scheme dependence to improve the calculation, one should care about the convergence of the expansion.

3.3.3 Interaction potential from lattice QCD: case of center-of-mass frame

Now let us consider the extraction of the interaction potential from lattice QCD. In this subsection, we first consider a case of the center-of-mass frame. We consider Euclidean spacetime in the following.

Naive method

In order to extract the potential, we need to calculate the NBS wave function beforehand. In lattice QCD, the NBS wave function are encoded in a correlation function defined as

$$F(x_1, x_2) = \langle \varphi_1(x_1)\varphi_2(x_2)\overline{\mathcal{J}}(0)\rangle, \tag{3.61}$$

where φ_i is a hadron operator and $\overline{\mathcal{J}}(0)$ is a source operator, which has the same quantum numbers as the target two hadron system. The part $\varphi_1(x_1)\varphi_2(x_2)$ is called a sink operator, whose choice determines the scheme of the NBS wave function. A typical choice is local operators of the target two hadrons putting on the same timeslice (it is called "equal-time local-sink scheme"). In our study, however, we choose some non-typical schemes to reduce systematical uncertainty, as discussed later.

[1] In general we can include not only terms with even powers of ∇ but also ones with odd powers. A fact that we do not include odd-power terms here can be regarded as the scheme of the potential.

By inserting the complete set of the scattering states in lattice QCD, we obtain

$$\begin{aligned} F(x_1,x_2) &= \sum_n \langle \varphi_1(x_1)\varphi_2(x_2)|W_n\rangle\langle W_n|\overline{\mathcal{J}}(0)\rangle + (\text{inelastic}) \\ &= \sum_n A_n \phi_{W_n}(\mathbf{x},t)e^{-W_n T} + (\text{inelastic}), \end{aligned} \tag{3.62}$$

where $\mathbf{x}, t$ are the relative space-time coordinates between two operators at sink, and T is the center-of-mass imaginary time. $A_n = \langle W_n|\overline{\mathcal{J}}(0)|0\rangle$ is an overlapping factor. Therefore we can extract the lowest NBS wave function by taking $T \gg 1$,

$$F(x_1,x_2) \to A_0\phi_{W_0}(\mathbf{x},t)e^{-W_0 T}\ (T \gg 1). \tag{3.63}$$

The effective leading-order potential, $U(\mathbf{x},\mathbf{x}') = V(\mathbf{x})\delta(\mathbf{x}-\mathbf{x}')$, can be obtained at a sufficiently large T as

$$V_t^{\mathrm{LO}}(\mathbf{x}) = \frac{\frac{1}{2\mu}(\nabla^2 + k_0^2)F(x_1,x_2)}{F(x_1,x_2)}, \tag{3.64}$$

where $k_0 = \sqrt{W_0^2/4 - m^2}$. Although we can calculate the potential by this naive method, we use a cleverer method called a time-dependent method [61] in practice. We introduce the time-dependent method next.

Time-dependent method

In the time-dependent method [61], we first define a normalized correlation function (we call it "R-correlator") as

$$R(\mathbf{x},t,T) \equiv \frac{F(x_1,x_2)}{C_1(T)C_2(T)}, \tag{3.65}$$

where F is a correlation function introduced above and $C_i(T) = \sum_{\mathbf{x},\mathbf{y}}\langle \varphi_i(\mathbf{x},T)\bar{\varphi}_i(\mathbf{y},0)\rangle$ is a two-point function of the target hadrons. From eq. (3.62), the R-correlator behaves as

$$R(\mathbf{x},t,T) = \sum_n B_n \phi_{W_n}(\mathbf{x},t)e^{-\Delta W_n T} + (\text{inelastic}) \tag{3.66}$$

$$\Delta W_n = W_n - 2m, \tag{3.67}$$

when T is large enough. The energy shift ΔW_n satisfies the following equation:

$$\begin{aligned} (\Delta W_n)^2 &= (W_n - 2m)^2 \\ &= W_n^2 - 4mW_n + 4m^2 \\ &= 4(k_n^2 + m^2) - 4mW_n + 4m^2 \\ &= 4k_n^2 - 4m(W_n - 2m) \\ &= 4k_n^2 - 4m\Delta W_n, \end{aligned}$$

$$\therefore \Delta W_n = \frac{k_n^2}{m} - \frac{(\Delta W_n)^2}{4m}. \tag{3.68}$$

Since T derivatives of the R-correlator gives a factor of $-\Delta W_n$, we can show that the R-correlator satisfies

$$\therefore \left[\frac{\nabla^2}{m} - \frac{\partial}{\partial T} + \frac{1}{4m}\frac{\partial^2}{\partial T^2}\right] R(\mathbf{x}, t, T) = \int d^3\mathbf{x}' U_t(\mathbf{x}, \mathbf{x}') R(\mathbf{x}', t, T), \tag{3.69}$$

when the inelastic contributions are negligible. The effective LO potential is given as

$$V_t^{\mathrm{LO}} = \frac{\left[\frac{\nabla^2}{m} - \frac{\partial}{\partial T} + \frac{1}{4m}\frac{\partial^2}{\partial T^2}\right] R(\mathbf{x}', t, T)}{R(\mathbf{x}', t, T)}. \tag{3.70}$$

The first advantage of this method is that we can use smaller timeslices to obtain the potential since we only need to suppress the inelastic contributions, rather than the elastic excited states. It enables us to calculate the correct potentials of systems whose signals are buried by noises at large timeslices, like two-baryon scatterings. At the same time, all elastic states are included in this method thanks to the replacement of the k_n^2 by the combination of the time derivatives.

3.3.4 Interaction potential from lattice QCD: case of laboratory frame

The extraction of the HAL QCD potential from the laboratory frame NBS wave function has not developed well until now, since the conventional center-of-mass approach has been enough to calculate physical observables correctly. Recently, however, the need for the laboratory frame calculation gradually increases. For example, the recent ρ resonance study, which will be discussed in Chap. 6, reveals that P-wave scattering phase shifts can deviate from correct values in the low-energy region not covered by the center-of-mass frame when the non-locality of the potential is happened to be large. Moreover, in analyses of hadron systems with the same quantum number as a vacuum (e.g. the $I = 0$ S-wave $\pi\pi$ interaction corresponding to the σ resonance), introducing non-zero total momenta is a promising way to reduce contamination from the vacuum state. In this subsection, we introduce the formulation of the laboratory frame approach. We continuously consider Euclidean spacetime here. The numerical calculation based on this formulation, which is one of our achievements, will be discussed in Chap. 7.

First let us recall the relation between the NBS wave functions in laboratory and center-of-mass frame. As already discussed, the relative NBS wave function in the laboratory frame is related to the center-of-mass counterpart by the Lorentz transformation as

$$\phi_{k_1,k_2}(x) = \phi_{k_1^*,k_2^*}(x^*), \tag{3.71}$$

where $\mathbf{k}^* = \mathbf{k}_1^* = -\mathbf{k}_2^*$ and $W^* = 2\sqrt{k^{*2} + m^2}$. In this subsection, we represent center-of-mass quantities with starred symbols (*). Relative coordinates in the laboratory and center-of-mass

frames are related as

$$x^{*4} = \gamma(x^4 - i\mathbf{v}\cdot\mathbf{x}_\parallel), \quad \mathbf{x}^*_\parallel = \gamma(\mathbf{x}_\parallel + i\mathbf{v}x^4), \quad \mathbf{x}^*_\perp = \mathbf{x}_\perp, \tag{3.72}$$

where $\parallel$ and $\perp$ represent vector components parallel and perpendicular to the direction of the total momentum, respectively. The velocity is determined from $\mathbf{P}^* = \gamma(\mathbf{P} - \mathbf{v}W) = 0$ as $\mathbf{v} = \mathbf{P}/W$, where W is the total energy in the laboratory frame, while the total energy in the center-of-mass frame W^* is related to W by

$$W^{*2} = W^2 - \mathbf{P}^2. \tag{3.73}$$

The interaction potential is defined in the center-of-mass frame through the Schrödinger–type equation as

$$\frac{1}{2\mu}(\nabla^{*2} + k^{*2})\phi_{k^*_1,k^*_2}(\mathbf{x}^*, x^{*4}) = \int d^3\mathbf{y}^* U_{x^{*4}}(\mathbf{x}^*, \mathbf{y}^*)\phi_{k^*_1,k^*_2}(\mathbf{y}^*, x^{*4}). \tag{3.74}$$

By combining eqs. (3.24), (3.72) and (3.74), we can rewrite the Schrodinger–type equation in terms of the laboratory frame quantities as

$$\begin{aligned}&\frac{1}{2\mu}(\nabla^2_\perp + \gamma^2(\nabla_\parallel + i\mathbf{v}\partial_{x^4})^2 + k^{*2})\phi_{k_1,k_2}(\mathbf{x}, x^4)\\ &\quad = \sum_i V^i_{\gamma(x^4 - i\mathbf{v}\cdot\mathbf{x}_\parallel)}\left(\mathbf{x}_\perp, \gamma(\mathbf{x}_\parallel + i\mathbf{v}x^4)\right)\left(\nabla^2_\perp + \gamma^2(\nabla_\parallel + i\mathbf{v}\partial_{x^4})^2\right)^i \phi_{k_1,k_2}(\mathbf{x}, x^4),\end{aligned} \tag{3.75}$$

where we have applied the derivative expansion $U_{x^{*4}}(\mathbf{x}^*, \mathbf{y}^*) = \sum_i V^i_{x^{*4}}(\mathbf{x}^*)\left(\nabla^{*2}\right)^i \delta(\mathbf{x}^* - \mathbf{y}^*)$. To extract meaningful potential from this equation, $x^4 = 0$ is required since $\mathbf{x}^*_\parallel$ becomes complex with non-zero x^4. We also fix $\mathbf{x}_\parallel$ to specify the scheme of the potential via x^{*4}, since x^{*4} depends on $\mathbf{x}_\parallel$. In this thesis, we take $\mathbf{x}_\parallel = 0$ and thus obtain the equal–time scheme potential.

Naive method

In lattice simulations, we put the system in a box of size $L \times L \times L$ with periodic boundary conditions in the laboratory frame. We define a correlation function as

$$F_{\mathbf{P}}(x_1, x_2) = \langle\varphi_1(x_1)\varphi_2(x_2)\overline{\mathcal{J}}_{\mathbf{P}}(0)\rangle, \tag{3.76}$$

where $\overline{\mathcal{J}}_{\mathbf{P}}(0)$ creates two-particle states with total momentum $\mathbf{P}$ at $T = 0$, which is quantized as $\mathbf{P} = \frac{2\pi}{L}\mathbf{n}_{\text{total}}$ ($\mathbf{n}_{\text{total}} \in \mathbf{Z}^3$). This correlation function can be written as

$$F_{\mathbf{P}}(x_1, x_2) = e^{i\mathbf{P}\cdot\mathbf{X}}\sum_{\mathbf{n}} A_{\mathbf{P},n}\phi_{W_n}(x)e^{-W_n T} + (\text{inelastic contributions}) \tag{3.77}$$

$$\to e^{i\mathbf{P}\cdot\mathbf{X}}A_{\mathbf{P},0}\phi_{W_0}(x)e^{-W_0 T}, \qquad (T \gg 1), \tag{3.78}$$

where $A_{\mathbf{P},n} = \langle W_n | \overline{\mathcal{J}}_{\mathbf{P}}(0)|0\rangle$. Therefore, we can extract the NBS wave function of the lowest energy state at a large T, same as the center-of-mass approach. Note that these relative NBS wave functions have a periodicity depending on $\mathbf{P} = \frac{2\pi}{L}\mathbf{n}_{\rm total}$ as

$$\phi_W(\mathbf{x} + \mathbf{m}L, x^4)e^{i\pi\mathbf{n}_{\rm total}\cdot\mathbf{m}} = \phi_W(\mathbf{x}, x^4) \quad (\mathbf{n}_{\rm total}, \mathbf{m} \in \mathbf{Z}^3), \tag{3.79}$$

which can be derived from (3.22) together with the periodicity of coordinates $\mathbf{x_i}$ $(i = 1, 2)$. The calculations of derivatives (e.g. $\nabla_\parallel$ at $\mathbf{x}_\parallel = 0$) are implemented by taking this periodicity into account. The effective LO potential in the equal–time scheme is obtained at a sufficiently large T as

$$V^{\rm LO}_{x^{*4}=0}(\mathbf{x}^*_\perp) = \left.\frac{(\nabla^2_\perp + \gamma^2(\nabla_\parallel + i\mathbf{v}\partial_{x^4})^2 + k^{*2}_0)F_{\mathbf{P}}(x_1, x_2)}{2\mu F_{\mathbf{P}}(x_1, x_2)}\right|_{x^4=0,\mathbf{x}_\parallel=0}, \tag{3.80}$$

where we set $x^4 = 0$ and $\mathbf{x}_\parallel = 0$ after taking derivatives in the right–hand side. The relative momentum k^{*2}_0 is obtained by $k^{*2}_0 = W^{*2}_0/4 - m^2 = (W^2_0 - P^2)/4 - m^2$.

Time-dependent method

As the case of the center-of-mass frame, the time-dependent method is available for the laboratory frame approach, even though it becomes more involved. We define the R-correlator in the laboratory frame as

$$R(\mathbf{x}, x^4, X^4) = \frac{e^{-i\mathbf{P}\cdot\mathbf{X}}F_{\mathbf{P}}(x_1, x_2)}{C_1(X^4)C_2(X^4)}, \tag{3.81}$$

where $C_i(X^4)$ $(i = 1, 2)$ are certain hadron two-point functions and a factor $e^{-i\mathbf{P}\cdot\mathbf{X}}$ removes the plane wave factor $e^{i\mathbf{P}\cdot\mathbf{X}}$ in (3.76). Since hadrons basically have momenta in the laboratory frame, a normalization by a free lowest energy is one natural choice. For example, if the source operator forms like $\overline{\mathcal{J}}_{\mathbf{P}}(0) = \sum_{\mathbf{x},\mathbf{y}} e^{i\mathbf{P}\cdot\mathbf{x}}\bar\varphi_1(\mathbf{x}, 0)\bar\varphi_2(\mathbf{y}, 0)$, then the normalization is done by $C_1(T) = \sum_{\mathbf{x},\mathbf{y}} e^{i\mathbf{P}\cdot(\mathbf{y}-\mathbf{x})}\langle\varphi_1(\mathbf{x}, T)\bar\varphi_1(\mathbf{y}, 0)\rangle$ and $C_2(T) = \sum_{\mathbf{x},\mathbf{y}}\langle\varphi_2(\mathbf{x}, T)\bar\varphi_2(\mathbf{y}, 0)\rangle$. We note that we can choose an another normalization, e.g. using hadron masses like the center-of-mass case. The difference of those normalizations is only the definition of the energy shift, therefore they give the same result in principle. In practice, however, some difference may appear due to the systematics like the discretization error. Since the involved calculation of the laboratory frame formalism may cause such systematics, we check it explicitly in our numerical simulation. It will be discussed in Chap. 7 and Appendix F.

To extract the potential we calculate the following parts beforehand:

$$G(\mathbf{x}, x^4, X^4) = \left((\partial_{X^4} - W_{0,\rm free})^2 - \mathbf{P}^2\right) R(\mathbf{x}, x^4, X^4), \tag{3.82}$$

$$E(\mathbf{x}, x^4, X^4) = \frac{1}{4m}\left[\partial^2_{X^4} - 2W_{0,\rm free}\partial_{X^4} + W^2_{0,\rm free} - \mathbf{P}^2 - 4m^2\right] G(\mathbf{x}, x^4, X^4), \tag{3.83}$$

$$L_\perp(\mathbf{x}, x^4, X^4) = \nabla^2_\perp G(\mathbf{x}, x^4, X^4), \tag{3.84}$$

$$L_\parallel(\mathbf{x}, x^4, X^4) = \left(-(\partial_{X^4} - W_{0,\rm free})\nabla_\parallel + i\mathbf{P}\partial_{x^4}\right)^2 R(\mathbf{x}, x^4, X^4), \tag{3.85}$$

where $W_{0,\text{free}}$ is a free lowest energy expected by the source operator. At a large X^4 where the inelastic contributions can be neglected, we have

$$G(\mathbf{x}, x^4, X^4) \simeq \sum_n B'_n W_n^{*2} \varphi_{W_n}(\mathbf{x}, x^4) e^{-(W_n - W_{0,\text{free}})X^4} \tag{3.86}$$

$$E(\mathbf{x}, x^4, X^4) \simeq \sum_n B'_n W_n^{*2} \frac{k_n^{*2}}{m} \varphi_{W_n}(\mathbf{x}, x^4) e^{-(W_n - W_{0,\text{free}})X^4} \tag{3.87}$$

$$L_\perp(\mathbf{x}, x^4, X^4) \simeq \sum_n B'_n W_n^{*2} \nabla_\perp^2 \varphi_{W_n}(\mathbf{x}, x^4) e^{-(W_n - W_{0,\text{free}})X^4} \tag{3.88}$$

$$L_\parallel(\mathbf{x}, x^4, X^4) \simeq \sum_n B'_n W_n^{*2} \gamma_n^2 (\nabla_\parallel + i\mathbf{v}_n \partial_{x^4})^2 \varphi_{W_n}(\mathbf{x}, x^4) e^{-(W_n - W_{0,\text{free}})X^4}, \tag{3.89}$$

where B'_n is an overlapping factor in the normalized correlation function, the center-of-mass energy of $W_n^{*2} = W_n^2 - \mathbf{P}^2 = 4(k_n^{*2} + m^2)$ and the boost factor of $\gamma_n^2 = \frac{W_n^2}{W_n^{*2}}$.

By combining these and eq. (3.75), we obtain

$$\begin{aligned} \left(\frac{L_\perp + L_\parallel}{m} + E \right) (\mathbf{x}, x^4, X^4) \Big|_{x^4=0, \mathbf{x}_\parallel = 0} &\simeq \sum_i V^i_{x^{*4}=0} \left(\mathbf{x}^*_\perp = \mathbf{x}_\perp, \mathbf{x}^*_\parallel = 0 \right) \\ &\times \left((\nabla^{*2})^i G(x, x^4, X^4) \right) \big|_{x^4=0, \mathbf{x}_\parallel = 0} \end{aligned} \tag{3.90}$$

at a large X^4, where the operation of starred-Laplacians to G is understood as

$$(\nabla^{*2})^i G(x, x^4, X^4) = \sum_n B'_n W_n^{*2} \left(\nabla_\perp^2 + \gamma_n^2 (\nabla_\parallel + i\mathbf{v}_n \partial_{x^4})^2 \right)^i \varphi_{W_n}(\mathbf{x}, x^4) e^{-(W_n - W_{0,\text{free}})X^4}. \tag{3.91}$$

Note that we can put V^i outside a summation over n for elastic states in (3.90) only at $x^{*4} = 0$, since the scheme of the potential depends on n as long as $x^{*4} = \gamma_n(x^4 - i\mathbf{v}_n \cdot \mathbf{x}_\parallel) \neq 0$. For example, the effective LO potential is given by

$$V^{\text{LO}}_{x^{*4}=0}(\mathbf{x}_\perp) = \left. \frac{\left(L_\perp + L_\parallel + mE \right) (\mathbf{x}, x^4, X^4)}{m G(\mathbf{x}, x^4, X^4)} \right|_{x^4=0, \mathbf{x}_\parallel = 0}. \tag{3.92}$$

This procedure is more complicated than the conventional time-dependent method, since we need to sum over n without knowing not only k_n^{*2} in (3.87) but also the Lorentz factors γ_n^2 and velocities $\mathbf{v}_n$ in (3.89), by combining several terms as shown above. In principle, the potential does not depend on the normalization discussed above since their difference is just a definition of the energy shift. In practice, however, the normalization dependence can appear due to the statistical correlation between the numerator and denominator of the R-correlator and other systematics on lattice simulations.

3.3.5 Calculations of physical observables

Once the potential is extracted, we can calculate physical observables by solving the Schrödinger equation. If the interaction disappears within a half of the lattice box size, the infinite-volume Schrödinger equation is valid since the extracted potential is not affected by the periodicity. To solve the infinite volume Schrodinger equation, the extracted potentials are fitted by some fit function in practice. Furthermore, the interaction potential can be immediately applied to other model calculations of hadron phenomena.

Finally, let us summarize possible systematics appearing in the HAL QCD method. The most important one is the truncation error of the derivative expansion. Generally speaking, the effective potentials depend on a choice of source operators. In other words, they implicitly depend on discrete energy levels included in their determination due to the truncation of the derivative expansion. Therefore, systematic errors in the derivative expansion for physical observables depend on the magnitude of non-locality in the true potential as well as on the difference between the energy region relevant for physical observables and that employed to determine the effective potentials. To see the truncation effect of a target observable explicitly, we need to calculate the observable by several source operators (and their combinations) and see the dependence on them.

In addition to the derivative expansion, there is another source of systematics, namely the mixing of the higher partial waves. Since lattice QCD simulation is performed in a finite-volume box, the rotational invariance reduces to cubic (or, in the laboratory frame, some hexahedral) invariance. Therefore, the scattering states in lattice QCD belong to irreducible representations of the reduced symmetry group. In terms of the basis of the continuum $O(3)$ group, those irreducible representations are mixtures of partial waves, therefore the scattering analysis in lattice QCD suffers from the partial wave mixing in general. The details of the relation between irreducible representations and partial waves appearing in our study are summarized in Appendix B. In the HAL QCD method, such contamination appears as non-smooth behavior of the r dependence of the potential, and the fit procedure can be affected. Fortunately, most of the non-smooth behavior can be removed by the effective partial wave decomposition recently introduced [62], except for the small r region of the potential. The remaining contamination should be treated appropriately if it is not negligible.

3.4 Lüscher's finite volume method

In this section, we briefly introduce another way to study hadron scatterings from lattice QCD, the Lüscher's finite volume method[12]. This method is also based on the asymptotic behavior of the NBS wave function. In contrast to the HAL QCD method, however, it focuses on the asymptotic region to extract the scattering information.

3.4.1 General solution of the Helmholtz equation in a finite box

Let us consider the scattering of two distinguishable scalar particles in the center-of-mass frame in a $L \times L \times L$ finite box with a periodic boundary condition. The relative NBS wave function in the center-of-mass frame satisfies the periodicity,

$$\phi_{\mathbf{k}}^{\text{elas.}}(\mathbf{x} + \mathbf{m}L, t) = \phi_{\mathbf{k}}^{\text{elas.}}(\mathbf{x}, t) \quad (\mathbf{m} \in \mathbf{Z}^3), \tag{3.93}$$

and the Helmholtz equation,

$$(\nabla^2 + k^2)\phi_{\mathbf{k}}^{\text{elas.}}(\mathbf{x}, t) \to 0 \quad (|\mathbf{x}| > R), \tag{3.94}$$

in the asymptotic region. The radial NBS wave function behaves as

$$\phi_{lm}(k, r, t) \approx b_{lm}(k, t) \left[\cos(\delta_l(k)) j_l(kr) + \sin(\delta_l(k)) n_l(kr)\right], \tag{3.95}$$

with some coefficients of b_{lm}.

On the other hand, we can construct a general solution of the Helmholtz equation which satisfies (3.93),

$$\begin{aligned} \phi_{L,k}(\mathbf{r}) &= \sum_{l,m} v_{lm}(k) G_{lm}(\mathbf{r}, k) && (3.96) \\ G_{lm}(\mathbf{r}, k) &= \sqrt{4\pi}\mathcal{Y}_{lm}(\nabla) G(\mathbf{r}, k) && (3.97) \\ G(\mathbf{r}, k) &= \frac{1}{L^3} \sum_{\mathbf{n} \in \mathbb{Z}^3} \frac{e^{-i\frac{2\pi}{L}\mathbf{n}\cdot\mathbf{r}}}{(\frac{2\pi}{L}\mathbf{n})^2 - k^2}, && (3.98) \end{aligned}$$

where $\mathcal{Y}_{lm}(\mathbf{r}) = r^l Y_{lm}(\Omega_{\mathbf{r}})$. The partial wave decomposition of $G(\mathbf{r}, k)$ is given as

$$G(\mathbf{r}, k) = \frac{1}{4\pi} n_0(kr) + \sum_{l,m} g_{lm}(k) j_l(kr) Y_{lm}(\Omega_{\mathbf{r}}), \tag{3.99}$$

$$g_{lm} = \frac{1}{L^3} \sum_{\mathbf{p} \in \Gamma} \frac{(ip/k)^l}{p^2 - k^2} \bar{Y}_{lm}(\Omega_{\mathbf{p}}), \tag{3.100}$$

where $\Gamma = \{\mathbf{p} | \mathbf{p} = \frac{2\pi}{L}\mathbf{n},\ \mathbf{n} \in \mathbb{Z}^3\}$, and it leads to

$$G_{lm}(\mathbf{r}, k) = -\frac{(-k)^{l+1}}{4\pi} \left[Y_{lm}(\Omega_{\mathbf{r}}) n_l(kr) + \sum_{l',m'} \mathcal{M}_{lm,l'm'} Y_{l'm'}(\Omega_{\mathbf{r}}) j_{l'}(kr) \right]. \tag{3.101}$$

3.4.2 Lüscher's formula

Since the asymptotic NBS wave function obeys the periodicity, it must be expressed by the basis of $G_{lm}(\mathbf{r}, k)$. On the other hand, we know that the asymptotic behavior of the wave function,

eq. (3.95). By combining them, we obtain the following relations between v_{lm} and $\delta(k)$:

$$b_{lm}\cos(\delta_l(k)) = \sum_{l'm'} v_{l'm'}\frac{(-1)^{l'}}{4\pi}k^{l'+1}\mathcal{M}_{l'm',lm}(k,L) \tag{3.102}$$

$$b_{lm}\sin(\delta_l(k)) = v_{lm}\frac{(-1)^{l}}{4\pi}k^{l+1}. \tag{3.103}$$

Finally we obtain a equation of v_{lm} by removing b_{lm} as

$$\sum_{l'm'} v_{l'm'}\frac{(-1)^{l'}}{4\pi}k^{l'+1}\left(\cot(\delta_{l'}(k))\delta_{l'l}\delta_{m'm} + \mathcal{M}_{l'm',lm}(k,L)\right) = 0. \tag{3.104}$$

In order for a non-trivial coefficient v_{lm} to exist, the matrix part of (3.104) must satisfy

$$\det\left[\cot(\delta_{l'}(k))\delta_{l'l}\delta_{m'm} + \mathcal{M}_{l'm',lm}(k,L)\right] = 0, \tag{3.105}$$

where the determinant is considered in the space of l, m. $\mathcal{M}$ is a function of (k, L), which is numerically calculable. The final equation is so-called Lüscher's formula [12]. This equation gives scattering energies allowed in a periodic box as $\{k_1, k_2, ...\}$, where $\det[\cot(\delta(k_i))\mathbf{1} + \mathcal{M}(k_i)] = 0$ $(i = 1, 2, ...)$, when we know the scattering phase shift $\delta_l(k)$ beforehand. In lattice QCD, however, we first know energies of scattering states from the correlation functions, then we inversely use the Lüscher's formula to specify corresponding $\delta_l(k)$. If the single-channel approximation is valid and there is no significant partial wave mixing, the equation gives a one-to-one correspondence between energies of lattice QCD (k) and scattering phase shifts at those energies $(\delta_l(k))$. For example, the Lüscher's formula becomes

$$\cot\delta_0(k) = \frac{4\pi}{k}\frac{1}{L^3}\sum_{\mathbf{p}\in\Gamma}\frac{1}{\mathbf{p}^2 - k^2}, \tag{3.106}$$

for the single-channel S-wave scattering in the center-of-mass frame. It is no longer a matrix equation since we only consider a subspace of $l = 0, m = 0$.

The extension to the laboratory frame is achieved by the similar discussion outlined above [13]. We consider the general solution of the Helmholtz equation which satisfy a modified periodicity called "d-periodicity",

$$\phi(\mathbf{x}) = (-1)^{\mathbf{d}\cdot\mathbf{n}}\phi(\mathbf{x} + \vec{\gamma}\mathbf{n}L), \tag{3.107}$$

where $\mathbf{d} = \mathbf{P}L/2\pi$ and $\vec{\gamma}\mathbf{n} = \gamma\mathbf{n}_{\parallel} + \mathbf{n}_{\perp}$. The relative NBS wave function boosted back to the center-of-mass frame satisfies this periodicity as well. From the relation between the coefficients of relative NBS wave function and the general solution, we obtain the similar formula as (3.104), and for the single-channel S-wave scattering it reduces to

$$\cot\delta_0(k) = \frac{4\pi}{k}\frac{1}{\gamma L^3}\sum_{\mathbf{p}\in\mathcal{P}_{\mathbf{d}}}\frac{1}{\mathbf{p}^2 - k^2}, \tag{3.108}$$

where

$$\mathcal{P}_{\mathbf{d}} = \{\mathbf{p}|\mathbf{p} = \frac{2\pi}{L}\vec{\gamma}^{-1}(\mathbf{m} + \frac{1}{2}\mathbf{d}),\ \mathbf{m} \in \mathbf{Z}^3\}, \tag{3.109}$$

with a short-hand notation $\vec{\gamma}^{-1}\mathbf{n} = \gamma^{-1}\mathbf{n}_{\parallel} + \mathbf{n}_{\perp}$.

In contrast to the HAL QCD method, this method needs explicit extraction of the energy eigenstates. Therefore analyses of systems suffering from the so-called signal-to-noise ratio problem are generally difficult. Furthermore, in cases of multi-channel scatterings or of the existence of non-negligible partial wave mixings, the inverse problem becomes ill-defined since we only have a single equation (3.104) for multiple unknown values. In order to avoid the ill-defined setting, it is mandatory to introduce some parametrizations for the energy dependence of the T-matrix with some ansatze to replace the inverse problem with the optimization problem. The physical quantities are read off from the ansatz functions with optimized parameters. One should be careful about the choice of the ansatze and should estimate the systematic uncertainty coming from it.

Chapter 4

Numerical challenge: All-to-all quark propagator

As already discussed in Chap. 2, calculations of correlation function contain inversions of the Dirac operator. In typical lattice QCD simulations, it is not a hard task since one only needs so-called "point-to-all" quark propagators, which are parts of a whole inverse of D. On the other hand, some systems which allow quark annihilation/creation processes require full information of the inverse matrix, so-called the "all-to-all" propagator. The all-to-all propagator costs higher than the point-to-all propagator by a factor of the lattice volume. Therefore, it is practically impossible to calculate it exactly. One of the main purposes of our study is to establish a satisfactory scheme to treat the all-to-all propagator in the HAL QCD method.

In this chapter, we introduce basic concepts of the all-to-all propagators. We first discuss how the all-to-all propagator appears in lattice QCD calculations by considering some examples of calculations appearing in our study. Then, we introduce one of the fundamental techniques to estimate the all-to-all propagator, the noisy estimator. This technique is very important since it is the foundation of several improved methods. After that, we introduce the hybrid method[29], which is an improved version of the noisy estimator. In the last part of this chapter, we discuss three techniques to establish a more suitable strategy of all-to-all estimations in the HAL QCD method, namely the one-end trick [32], sequential propagator technique [33], and the covariant approximation averaging (CAA) [34]. A detailed discussion on how to combine those building blocks will be presented in the following chapter.

4.1 Appearance of all-to-all propagator

First let us consider a simple example, namely a calculation of the pion two-point function. The pion two-point function is defined as

$$C(t) = \sum_{t_0} \sum_{\mathbf{x},\mathbf{y}} \langle \pi^+(\mathbf{x}, t + t_0) \pi^-(\mathbf{y}, t_0) \rangle, \tag{4.1}$$

where pion operators are given as $\pi^+ = \bar{d}\gamma_5 u$ and $\pi^- = \bar{u}\gamma_5 d$. This correlation function is estimated by the Wick contraction and the Monte Carlo simulation as

$$C(t) \approx \frac{1}{N}\sum_i \sum_{t_0} \sum_{\mathbf{x},\mathbf{y}} \mathrm{tr}\left[\gamma_5 D^{-1}[U_i](\mathbf{x}, t+t_0|\mathbf{y}, t_0)\gamma_5 D^{-1}[U_i](\mathbf{y}, t_0|\mathbf{x}, t+t_0)\right], \tag{4.2}$$

where N is the number of Monte Carlo samples and the trace is taken in the color and spinor spaces. We also show the U_i dependence of the quark propagators explicitly. As seen in Eq.(4.2), coordinates $\mathbf{x}, \mathbf{y}, t_0$ are summed over, and t is arbitrary to extract the pion mass from the time dependence of $C(t)$. Therefore, we need whole information of the quark propagator, namely $D^{-1}[U_i](\mathbf{x}, t|\mathbf{y}, t_0)$ for arbitrary $\mathbf{x}$, t, $\mathbf{y}$, and t_0 (and abbreviated indices of color and spinor) to estimate this correlation function. We call this "all-to-all propagator" since it naively represents a propagation of a quark from arbitrary points to another arbitrary points.

Fortunately, in some cases correlation functions have symmetries such as a translational invariance, we can avoid a full calculation of the all-to-all propagator [1] . In the case of the pion 2pt function above, we do not necessarily need for the summation of $(\mathbf{y}, t_0)$ thanks to the translational invariance, and the correlation function reduces to

$$C(t) \approx \frac{1}{N}\sum_i \sum_{\mathbf{x}} \mathrm{tr}\left[\gamma_5 D^{-1}[U_i](\mathbf{x}, t+t_0|\mathbf{x_0}, t_0)\gamma_5 D^{-1}[U_i](\mathbf{x_0}, t_0|\mathbf{x}, t+t_0)\right], \tag{4.3}$$

with some fixed coordinates $(\mathbf{x_0}, t_0)$. Quark propagators with fixed column indices are called "point-to-all" propagators and obtained by solving the following linear equation:

$$D_{a,\alpha|b,\beta}(x|y)\psi_{b,\beta}(y) = \eta_{a,\alpha}(x), \tag{4.4}$$

here we show all indices explicitly for convenience. A source vector $\eta_{a,\alpha}(n)$ is chosen to specify the fixed column indices of point-to-all propagators as

$$\eta_{a,\alpha}(x) = \delta_{aa_0}\delta_{\alpha\alpha_0}\delta_{xx_0}, \tag{4.5}$$

where zero-subscripted indices are fixed. Obviously, the solution behaves as

$$\psi_{b,\beta}(y) = D^{-1}_{b,\beta|c,\gamma}(y|z)\eta_{c,\gamma}(z) = D^{-1}_{b,\beta|a_0,\alpha_0}(y|x_0). \tag{4.6}$$

Since the trace of the color and spinor indices is required, we repeatedly solve the linear equation with 3×4 different combination of indices of a_0, α_0. Furthermore, the "all-to-point" propagator $D^{-1}[U_i](\mathbf{x_0}, t_0|\mathbf{x}, t+t_0)$ can be immediately obtained from the point-to-all propagator by using

[1] Strictly speaking, such invariance is valid up to statistical errors of Monte Carlo simulations. Therefore the summation of $(\mathbf{y}, t_0)$ in Eq. (4.2) is still a meaningful operation to reduce the statistical fluctuation by assuming the invariance, as long as the numerical cost of this summation is feasible. Statistical improvement based on the invariance of the observable is sometimes useful, and the covariant approximation averaging is one of those improvement techniques.

the γ_5-Hermiticity of the Dirac operator. Therefore, inversions of 12 times are enough in our example.

Furthermore, in some cases, we can also avoid the all-to-all propagator by choosing source operators which do not induce any all-to-all estimations. In above example of the pion two-point function, we can choose another source operator (called "wall source") as

$$\pi^-(t_0) = \sum_{\mathbf{z_1},\mathbf{z_2}} \bar{u}(\mathbf{z_1}, t_0)\gamma_5 d(\mathbf{z_2}, t_0). \tag{4.7}$$

In this operator, each quarks are projected to zero-momentum. As a result, it can overlap the ground state as well as the zero-momentum pion operator in Eq.(4.2). We note that this operator needs the gauge fixing since it is not gauge invariant. The correlation function with this source operator is then given as

$$C(t) \approx \frac{1}{N}\sum_i \sum_{\mathbf{x},\mathbf{z_1},\mathbf{z_2}} \mathrm{tr}\left[\gamma_5 D^{-1}[U_i](\mathbf{x}, t+t_0|\mathbf{z_1}, t_0)\gamma_5 D^{-1}[U_i](\mathbf{z_2}, t_0|\mathbf{x}, t+t_0)\right], \tag{4.8}$$

and the propagators can be obtained by solving the linear equations (4.4) with source vectors

$$\eta_{a,\alpha}(x) = \delta_{aa_0}\delta_{\alpha\alpha_0}\delta_{tt_0}. \tag{4.9}$$

As the case of the point-to-all propagator, it is enough to solve it with 3×4 different combination of indices of (a_0, α_0). The wall source can be basically applied to systems consists of zero-momentum quarks (and hadrons).

In summary, many lattice QCD simulations can be performed without all-to-all propagators thanks to the symmetry or the choice of operators. However, there are some cases where estimations of the all-to-all propagators are unavoidable. A typical example is $I = 1$ $\pi\pi$ P-wave system, which is the main target in our study. To understand the situation, let us consider a part of the $I = 1$ $\pi\pi$ correlation function, namely the box diagram contribution given as

$$\begin{aligned}(-)\sum_{\mathbf{x},\mathbf{y_1},\mathbf{y_2}} e^{-i\mathbf{p}\cdot\mathbf{y_1}} e^{i\mathbf{p}\cdot\mathbf{y_2}}\ \mathrm{tr}\big[&D^{-1}(\mathbf{x}+\mathbf{r}, t|\mathbf{x}, t)\gamma_5 D^{-1}(\mathbf{x}, t|\mathbf{y_2}, t_0)\\ &\times\gamma_5 D^{-1}(\mathbf{y_2}, t_0|\mathbf{y_1}, t_0)\gamma_5 D^{-1}(\mathbf{y_1}, t_0|\mathbf{x}+\mathbf{r}, t)\gamma_5\big].\end{aligned} \tag{4.10}$$

(Details of this diagram will be discussed later.) In this calculation, pion operators in the source part are projected onto $\mathbf{p} = (0, 0, \pm 2\pi/L)$ to construct the source operator in T_1^- representation of the cubic group, whose leading partial wave is $l = 1$ (P-wave). Furthermore, to extract the spatial dependence of the NBS wave function, the sink coordinates $\mathbf{r}$ is taken arbitrarily, with a summation of the center-of-mass coordinates $\mathbf{x}$. Although we can ignore the sum of $\mathbf{x}$ by considering the translational invariance of the center-of-mass coordinates, all-to-all propagators are still remaining and there is no room to improve. Naively, the all-to-all propagator can be obtained by solving the linear equation (4.4) N_{vol} times more than the case of the point-to-all

propagator, but it is practically impossible. To understand its difficulty, let us estimate how long the all-to-all calculation takes using an actual calculation time. In our study using gauge configurations on the $32^3 \times 64$ lattice with the pion mass $m_\pi \approx 0.41$ GeV, it takes about two seconds to solve the single linear equation (4.4) using a supercomputer. To obtain the all-to-all propagator exactly in this case, it takes 2 sec. $\times 3 \times 4 \times 32^3 \times 64 = 50331648$ sec. ≈ 583 days. Moreover, we need to calculate the all-to-all propagators over $\mathcal{O}(100)$ Monte Carlo samples repeatedly to estimate the correlation function. As a result, it takes over hundred years to finish the calculation even if we use supercomputers. Therefore some approximation techniques are mandatory to investigate systems requiring the all-to-all propagator.

4.2 Estimation of all-to-all propagator

In this section, we introduce one of the important ideas to estimate all-to-all propagator, called the noisy estimator. We then discuss the dilution technique to reduce the statistical fluctuation attributed to the noisy estimator. The hybrid method, which is the improved version of the noisy estimator, is also explained.

4.2.1 Noisy estimator

Noisy estimator enables us to calculate an inverse matrix within a low computational cost in return for additional contamination. Let us consider a "noise vector" η, which satisfies the following conditions,

$$\langle\langle \eta_m \otimes \eta_n^\dagger \rangle\rangle = \delta_{mn}, \tag{4.11}$$

$$|\eta_n|^2 = 1, \tag{4.12}$$

where $\otimes$ represents a tensor product, n is an index of a vector space we considered (For the Dirac operator in lattice QCD it corresponds to the color, spinor and spacetime indices, (a, α, x)), and a double bracket represents a expectation value on a probability distribution from which the noise vector is sampled. For example, a Z_4 noise vector, whose components are randomly chosen from $\{\pm 1, \pm i\}$, satisfies those conditions. This condition indicates that an average over N_r samples of noise vectors, $\eta_{[r]} (r = 0, ..., N_\mathrm{r} - 1)$, is an unbiased estimator of a unit matrix as

$$\mathbf{1} \approx \frac{1}{N_\mathrm{r}} \sum_{r=0}^{N_\mathrm{r}-1} \eta_{[r]} \otimes \eta_{[r]}^\dagger. \tag{4.13}$$

Using solutions of linear equations $M\psi_{[r]} = \eta_{[r]}$, therefore, we can approximate the inverse matrix M^{-1} as

$$M^{-1} = M^{-1} \cdot \mathbf{1} \approx M^{-1} \left(\frac{1}{N_{\rm r}} \sum_{r=0}^{N_{\rm r}-1} \eta_{[r]} \otimes \eta_{[r]}^{\dagger} \right) \approx \frac{1}{N_{\rm r}} \sum_{r=0}^{N_{\rm r}-1} \psi_{[r]} \otimes \eta_{[r]}^{\dagger}. \tag{4.14}$$

Since we estimate the unit matrix with finite $N_{\rm r}$ samples, additional noise contamination is introduced here. This method is noisy because it relies on delicate cancellations in the $\mathcal{O}(1)$ fluctuations over many samples. One naive way to reduce the noise contamination is to increase $N_{\rm r}$, but we cannot take $N_{\rm r}$ so much since it is directly related to the number of inversions. There is, however, a clever way utilizing the property of the noise vector (4.12), called "dilution"[29]. The property (4.12) guarantees the diagonal part of the estimated unit matrix to be equal to 1, therefore the noise contamination only appears in the off-diagonal part of the estimated unit matrix. In such a situation, it is expected that replacing a part of off-diagonal elements to zero improves the signal since they must disappear statistically at $N_{\rm r} \to \infty$. The dilution gives a systematic way to achieve such zero replacements. First of all, we "dilute" the noise vector $\eta_{[r]}$ in some set of elements (i) such that

$$\eta_{[r]} = \sum_{i=0}^{N_{\rm dil}-1} \eta_{[r]}^{(i)}. \tag{4.15}$$

Then, by using $\eta_{[r]}^{(i)}$ (we call them "diluted vectors") we estimate the inverse matrix as

$$M^{-1} \approx \frac{1}{N_{\rm r}} \sum_{r=0}^{N_{\rm r}-1} \sum_{i=0}^{N_{\rm dil}-1} \psi_{[r]}^{(i)} \otimes \eta_{[r]}^{(i)\dagger}, \tag{4.16}$$

where $\psi_{[r]}^{(i)} = M^{-1}\eta_{[r]}^{(i)}$. To see what happens in Eq.(4.16), let us rewrite the original estimation (Eq.(4.14)) in terms of the diluted vectors:

$$M^{-1} \left(\frac{1}{N_{\rm r}} \sum_{r=0}^{N_{\rm r}-1} \eta_{[r]} \otimes \eta_{[r]}^{\dagger} \right) = \frac{1}{N_{\rm r}} \sum_{r=0}^{N_{\rm r}-1} M^{-1} \left[\sum_{i=0}^{N_{\rm dil}-1} \eta_{[r]}^{(i)} \otimes \eta_{[r]}^{(i)\dagger} + \sum_{i \neq j} \eta_{[r]}^{(i)} \otimes \eta_{[r]}^{(j)\dagger} \right]. \tag{4.17}$$

The second term of Eq.(4.17) only contains a contributions to the off-diagonal part, and the dilution explicitly replaces it to zero. Figure 4.1 shows 50×50 unit matrices estimated by 10 sample average as $\frac{1}{10}\sum_{i=0}^{9} \eta_{[i]} \otimes \eta_{[i]}^{\dagger}$ (left) and 10 diluted vectors generated by a single noise sample as $\sum_{i=0}^{9} \eta_{[0]}^{(i)} \otimes \eta_{[0]}^{(i)\dagger}$ (right). Horizontal and vertical axis correspond to the row and column of the estimated matrix, respectively, and the color of each element represents an absolute value of it. In the estimation of the dilution technique, we find that most of the off-diagonal part are exactly zero (= white), while the estimation by the noise average contains non-zero contamination in all off-diagonal elements. Instead, the dilution allows $\mathcal{O}(1)$ contamination near the diagonal part. Such remaining contamination comes from a remnant off-diagonal contributions in the first term

of Eq.(4.17), which can be reduced by finer dilutions (= increasing of $N_{\rm dil}$) and statistical improvements (= increasing of $N_{\rm r}$). The limit of the full dilution, where we have one diluted vector for each component of noise vector, results in the exact all-to-all propagator in a finite number of steps, because of the property (4.12). Since the exact all-to-all propagator is only reproduced at $N_{\rm r} \to \infty$ statistically, the dilution procedure is expected to be better than the increasing of $N_{\rm r}$ to achieve statistical improvement. Authors of Ref.[29] actually confirm that the expectation is true even with simple dilutions in their study.

In lattice QCD, there are typical schemes to split the noise vector into the diluted vectors along the color, spinor, and spacetime indices. The dilutions we employ in our study are summarized in Appendix C.

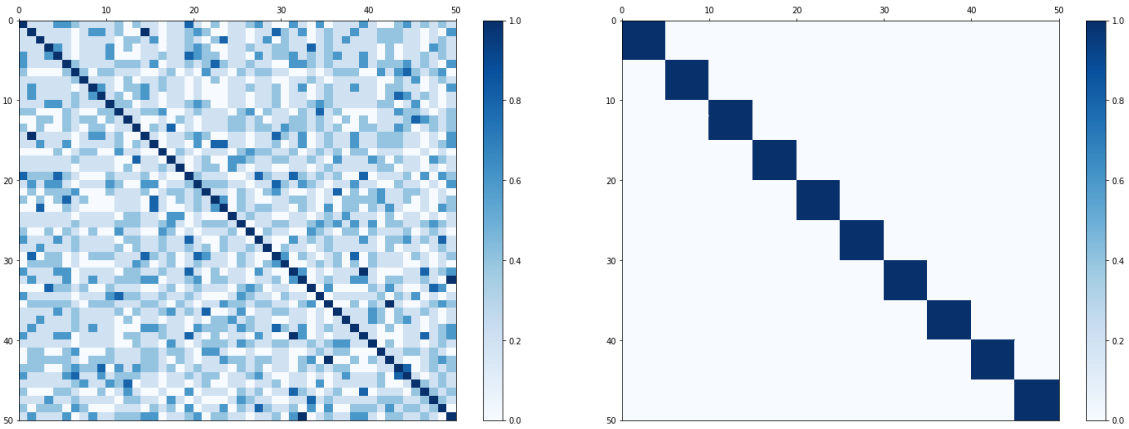

FIGURE 4.1: Comparison between the naive stochastic estimation of unit matrix and its modification with the dilution. (Left) Estimation by 10 independent sample average. (Right) Estimation by 10 diluted vectors generated by a single noise sample. Axis correspond to the row and column of the matrix and colors of elements represent their absolute values.

4.2.2 Hybrid method

The hybrid method combines a low-mode spectral decomposition and the noisy estimator. The low-mode part of the propagator contributes a lot to low-energy physical observables and the hybrid method can improve the signal in lattice QCD simulations. We explain its basic formulation in this section.

First, let us consider the spectral decomposition of an hermitian matrix M. Since eigenvectors of the hermitian matrix are orthogonal and form a complete set, we can decompose M by the eigenvectors $v^{(i)}$ and eigenvalues λ_i as

$$M = \sum_{i=0}^{N_{\rm max}-1} \lambda_i v^{(i)} \otimes v^{(i)\dagger}, \tag{4.18}$$

where $N_{\max}$ is a rank of M. The inverse matrix is also given as

$$M^{-1} = \sum_{i=0}^{N_{\max}-1} \frac{1}{\lambda_i} v^{(i)} \otimes v^{(i)\dagger}. \tag{4.19}$$

In lattice QCD, $M = \gamma_5 D = H$ with the Dirac operator which satisfy the γ_5-Hermiticity. However, it is impossible to calculate all eigenstates in practice. We therefore only consider a low-mode part of the matrix as

$$H_{\text{low}}^{-1} = \sum_{i=0}^{N_{\text{eig}}-1} \frac{1}{\lambda_i} v^{(i)} \otimes v^{(i)\dagger}, \tag{4.20}$$

where N_{eig} is the number of the low-modes. The missing high-mode part is covered by the noisy estimator as

$$H_{\text{high}}^{-1} = \frac{1}{N_{\text{r}}} \sum_{r=0}^{N_{\text{r}}-1} \sum_{j=0}^{N_{\text{dil}}-1} \psi_{[r]}^{(j)} \otimes \eta_{[r]}^{\dagger(j)}, \tag{4.21}$$

where the solutions $\psi_{[r]}^{(j)}$ are given as

$$\psi_{[r]}^{(j)} = H^{-1} \mathcal{P}_1 \eta_{[r]}^{(j)}, \tag{4.22}$$

with a projection operator onto the high-mode subspace $\mathcal{P}_1 = \mathbf{1} - \sum_{j=0}^{N_{\text{eig}}-1} v^{(j)} \otimes v^{\dagger(j)}$.

In summary, the whole propagator is estimated as

$$D^{-1} = H^{-1}\gamma_5 = \left(H_{\text{low}}^{-1} + H_{\text{high}}^{-1}\right)\gamma_5 \equiv \frac{1}{N_{\text{r}}} \sum_{r=0}^{N_{\text{r}}-1} \sum_{i=0}^{N_{\text{hl}}-1} u_{[r]}^{(i)} \otimes w_{[r]}^{\dagger(i)} \gamma_5, \tag{4.23}$$

where "hybrid lists" $u_{[r]}^{(i)}, w_{[r]}^{(i)}$ are defined as

$$w_{[r]}^{(i)} = \{\frac{v^{(0)}}{\lambda_0}, ..., \frac{v^{(N_{\text{eig}}-1)}}{\lambda_{N_{\text{eig}}-1}}, \eta_{[r]}^{(0)}, ..., \eta_{[r]}^{(N_{\text{dil}}-1)}\} \tag{4.24}$$

$$u_{[r]}^{(i)} = \{v^{(0)}, ..., v^{(N_{\text{eig}}-1)}, \psi_{[r]}^{(0)}, ..., \psi_{[r]}^{(N_{\text{dil}}-1)}\} \tag{4.25}$$

$$N_{\text{hl}} = N_{\text{eig}} + N_{\text{dil}}. \tag{4.26}$$

4.3 Techniques to reduce usage of noisy estimators

As will be discussed in the next chapter, it is revealed that the hybrid method costs a lot of computational resources and it is not suitable to perform large-scale simulations. The most time-consuming part is the suppression of the noise contamination coming from the noisy estimators. One possibility to improve the situation is to reduce insertions of the noisy estimators as many

as possible. In this section, we introduce effective techniques to achieve less usage of the noisy estimator. How to combine those techniques will be explained in Chap.6.

4.3.1 One-end trick

The one-end trick[32] enables us to estimate a combination of two all-to-all propagators with a space summation by using a single noisy estimator.

Let us consider a combination of quark propagators given by

$$\sum_{\mathbf{y}} e^{i\mathbf{p}\cdot\mathbf{y}} D^{-1}(\mathbf{x}_1, t_1|\mathbf{y}, t_0)\Gamma D^{-1}(\mathbf{y}, t_0|\mathbf{x}_2, t_2), \tag{4.27}$$

where D_f^{-1} is a quark propagator, Γ is some product of gamma matrices, and $x_i = (\mathbf{x}_i, t_i)$ are arbitrary. Such a structure typically appears at the source side of correlation functions including meson operators, e.g., the pion 2pt function with the zero-momentum projected source as discussed before. Naively, it needs two stochastic estimations for each, since each of them contains two all-to-all propagators. The one-end trick, however, utilize the γ_5-Hermiticity of the Dirac operator to estimate that structure with a single noise insertion as follows.

$$\begin{aligned}
&\sum_{\mathbf{y}} e^{i\mathbf{p}\cdot\mathbf{y}} D^{-1}(x_1|\mathbf{y}, t_0)\Gamma D^{-1}(\mathbf{y}, t_0|x_2) \\
&\quad = \sum_{\mathbf{y},\mathbf{z}} e^{i\mathbf{p}\cdot\mathbf{y}} D^{-1}(x_1|\mathbf{y}, t_0)\delta_{\mathbf{y},\mathbf{z}}\Gamma D^{-1}(\mathbf{z}, t_0|x_2) \\
&\quad \approx \sum_{\mathbf{y},\mathbf{z}} e^{i\mathbf{p}\cdot\mathbf{y}} D^{-1}(x_1|\mathbf{y}, t_0) \left(\frac{1}{N_{\mathrm{r}}}\sum_{r=0}^{N_{\mathrm{r}}-1} \eta_{[r]}(\mathbf{y})\eta^{\dagger}_{[r]}(\mathbf{z})\right)\Gamma D^{-1}(\mathbf{z}, t_0|x_2) \\
&\quad = \frac{1}{N_{\mathrm{r}}}\sum_{r=0}^{N_{\mathrm{r}}-1} \left(\sum_{\mathbf{y}} D^{-1}(x_1|\mathbf{y}, t_0)\eta_{[r]}(\mathbf{y})e^{i\mathbf{p}\cdot\mathbf{y}}\right)\left(\sum_{\mathbf{z}} \gamma_5 D^{-1}(x_2|\mathbf{z}, t_0)\gamma_5\Gamma^{\dagger}\eta_{[r]}(\mathbf{z})\right)^{\dagger},
\end{aligned} \tag{4.28}$$

where we insert the stochastic estimator $\delta_{\mathbf{y},\mathbf{z}} \approx \frac{1}{N_{\mathrm{r}}}\sum_{r=0}^{N_{\mathrm{r}}-1} \eta_{[r]}(\mathbf{z})\eta^{\dagger}_{[r]}(\mathbf{y})$ in the second line and use the γ_5-Hermiticity in the last line. We define "one-end vectors" as

$$\xi_{\mathbf{p},t_0[r]}(x) \equiv \sum_{\mathbf{y}} D^{-1}(x|\mathbf{y}, t_0)\eta_{[r]}(\mathbf{y})e^{i\mathbf{p}\cdot\mathbf{y}} \tag{4.29}$$

$$\chi_{\Gamma,t_0[r]}(x) \equiv \sum_{\mathbf{y}} D^{-1}(x|\mathbf{y}, t_0)\gamma_5\Gamma^{\dagger}\eta_{[r]}(\mathbf{y}), \tag{4.30}$$

then the final expression becomes

$$\sum_{\mathbf{y}} D^{-1}(\mathbf{x}_1, t_1|\mathbf{y}, t_0)\Gamma D^{-1}(\mathbf{y}, t_0|\mathbf{x}_2, t_2) \approx \frac{1}{N_{\mathrm{r}}}\sum_{r=0}^{N_{\mathrm{r}}-1} \xi_{\mathbf{p},t_0[r]}(\mathbf{x}_1, t_1) \otimes \chi^{\dagger}_{\Gamma,t_0[r]}(\mathbf{x}_2, t_2)\gamma_5. \tag{4.31}$$

The one-end vectors ξ and χ are obtained by solving the linear equation $D\xi = \eta e^{i\mathbf{p}\cdot\mathbf{y}}$ and $D\chi = \gamma_5\Gamma^\dagger\eta$, respectively. The dilution technique for noise reduction can be combined as well.

4.3.2 Sequential propagator technique

Let us consider a chain of two quark propagators as

$$\sum_{\mathbf{y}} D^{-1}(\mathbf{x},t|\mathbf{y},t')\Gamma D^{-1}(\mathbf{y},t'|\mathbf{x}_0,t_0), \tag{4.32}$$

where $\mathbf{x_0}, t_0$ are fixed and $\mathbf{x}, t, t'$ are arbitrary and Γ is some product of gamma matrices. The sequential propagator technique [33] is a way to calculate such a chain of quark propagators without any noisy estimator in a case where we have one of the quark propagators in some way. Here we assume that we have already solved the linear equations and obtained the point-to-all propagators as

$$\psi(\mathbf{x},t) = D^{-1}(\mathbf{x},t|\mathbf{x}_0,t_0). \tag{4.33}$$

By putting those solutions as source vectors of another linear equation,

$$D(\mathbf{x},t;z)\phi(z) = \Gamma\psi(\mathbf{x},t)\delta_{t,t'}, \tag{4.34}$$

we can obtain the chain of two propagators as a solution of the equation,

$$\begin{aligned}\phi(\mathbf{x},t) &= \sum_{\mathbf{y}} D^{-1}(\mathbf{x},t|\mathbf{y},t')\Gamma\psi(\mathbf{y},t') &(4.35)\\ &= \sum_{\mathbf{y}} D^{-1}(\mathbf{x},t|\mathbf{y},t')\Gamma D^{-1}(\mathbf{y},t'|\mathbf{x}_0,t_0). &(4.36)\end{aligned}$$

As seen, although $D^{-1}(\mathbf{x},t|\mathbf{y},t')$ is all-to-all, we can calculate it without any noisy estimator by considering the combination of two propagators. This method has also a good compatibility with meson operators as the one-end trick. Of course, we sometimes need to take $\mathbf{x_0}, t_0$ arbitrarily, requiring an another all-to-all propagator. In such a case, we can employ the one-end trick or can combine the sequential propagator and other all-to-all technique like the hybrid method.

4.3.3 Covariant approximation averaging (CAA)

The covariant approximation averaging[34] is a way to reduce statistical error using covariant symmetry of the target correlation function with minimal increase of its computational cost.

Let us consider an expectation value of an operator $\mathcal{O}[U](x,y)$, which has a symmetry property under a transformation $g \in G$ as

$$\langle \mathcal{O}^g[U](x,y)\rangle = \langle \mathcal{O}[U^g](x,y)\rangle, \tag{4.37}$$

where $U^g(x) = U(x^g)$ and $\mathcal{O}^g[U](x,y) = \mathcal{O}[U](x^g, y^g)$. If the operator is covariant under the transformation, for each Monte Carlo samples it satisfies

$$\mathcal{O}^g[U](x,y) = \mathcal{O}[U^g](x,y), \tag{4.38}$$

then there is a trivial identity,

$$\sum_{g\in G} \mathcal{O}^g[U](x,y) = \sum_{g\in G} \mathcal{O}[U^g](x,y), \tag{4.39}$$

for a set of transformations g with the number of elements N_G. Using this property, we can define an averaged operator $\mathcal{O}_G[U]$ as

$$\mathcal{O}_G[U] = \frac{1}{N_G}\sum_{g\in G} \mathcal{O}^g[U] = \frac{1}{N_G}\sum_{g\in G} \mathcal{O}[U^g], \tag{4.40}$$

whose expectation value is identical to the original one, since any transformed configurations U^g are regarded as different Monte Carlo samples with the same probability as U with an action invariant under g. The statistical error of $\mathcal{O}_G$ decreases by a factor of $1/\sqrt{N_G}$, although its computational cost naively increases by a factor of N_G. Such an improvement itself is very powerful and has been widely applied in many lattice QCD simulations. On the other hand, in cases where calculations of $\mathcal{O}[U]$ is numerically expensive, the factor N_G increase of its numerical cost is not acceptable. The covariant approximation averaging solves this problem by introducing approximation for $\mathcal{O}$.

In order to reduce numerical costs of transformed operators, authors introduce an approximation for $\mathcal{O}$, which is called $\mathcal{O}^{(\mathrm{appx})}$. Using $\mathcal{O}^{(\mathrm{appx})}$ and the original $\mathcal{O}$, an improved estimator for $\mathcal{O}$ is defined by

$$\mathcal{O}^{(\mathrm{imp})} = \mathcal{O} - \mathcal{O}^{(\mathrm{appx})} + \frac{1}{N_G}\sum_{g} \mathcal{O}^{(\mathrm{appx})g}. \tag{4.41}$$

Since the second and third terms cancel with each other after taking an expectation value and using the covariance of $\mathcal{O}^{(\mathrm{appx})}$, the improved estimator is unbiased,

$$\langle \mathcal{O}^{(\mathrm{imp})} \rangle = \langle \mathcal{O} \rangle. \tag{4.42}$$

On the other hand, the standard deviation of the improved estimator behaves as

$$\sigma^{(\mathrm{imp})} \approx \sigma \left[2\Delta r + \frac{1}{N_G} - \frac{2\Delta r}{N_G} + R^{\mathrm{corr}} \right]^{1/2}, \tag{4.43}$$

$$R^{\mathrm{corr}} = \frac{1}{N_G^2}\sum_{g\neq g'} r^{\mathrm{corr}}_{gg'}, \tag{4.44}$$

where

$$r_g = \frac{\langle \Delta\mathcal{O}\Delta\mathcal{O}^{(\mathrm{appx})g}\rangle}{\sigma\sigma_g^{(\mathrm{appx})}}, \tag{4.45}$$

$$r_{gg'}^{\mathrm{corr}} = \frac{\langle \Delta\mathcal{O}^{(\mathrm{appx})g}\Delta\mathcal{O}^{(\mathrm{appx})g'}\rangle}{\sigma_g^{(\mathrm{appx})}\sigma_g'^{(\mathrm{appx})}}, \tag{4.46}$$

$$\Delta r = 1 - r_{g=I}, \tag{4.47}$$

with $\sigma^X = \sqrt{\langle(\Delta\mathcal{O}^X)^2\rangle}$ and $\Delta\mathcal{O}^X = \mathcal{O}^X - \langle\mathcal{O}^X\rangle$. The error reduction by a factor of $1/\sqrt{N_G}$ can be achieved if $\Delta r \ll 1$ and $R^{\mathrm{corr}} \ll 1$ are satisfied. Authors summarize the conditions on $\mathcal{O}^{(\mathrm{appx})}$ and the choice of the transformation $g \in G$ to achieve an appropriate statistical improvement as follows [2] :

1. $\mathcal{O}^{(\mathrm{appx})}$ is covariant under G.
2. $\mathcal{O}^{(\mathrm{appx})}$ is strongly correlated with original $\mathcal{O}$, *i.e.* $\Delta r \ll 1$.
3. The computational cost of $\mathcal{O}^{(\mathrm{appx})}$ is much smaller than $\mathcal{O}$.
4. The transformation $g \in G$ is chosen to give small positive correlation among $\{\mathcal{O}^{(\mathrm{appx})g}\}$, *i.e.* $R^{\mathrm{corr}} \ll 1/N_G$.

There are two typical choices of $\mathcal{O}^{(\mathrm{appx})}$, namely the low-mode averaging (LMA) and the all-mode averaging (AMA).

- Low-mode averaging (LMA): $\mathcal{O}^{(\mathrm{appx})}$ is estimated by the low-mode quark propagator as

$$\mathcal{O}^{(\mathrm{LMA})} = \mathcal{O}[D^{-1}_{(\mathrm{low})}], \quad D^{-1}_{(\mathrm{low})} = \sum_{i=0}^{N_{\mathrm{eig}}-1} \frac{1}{\lambda_i} v^{(i)} \otimes v^{(i)\dagger}\gamma_5, \tag{4.48}$$

  where $\lambda_i, v^{(i)}$ are low-modes of $H = \gamma_5 D$. This approximation is good for low-mode dominant observables since it discard the high-mode part.

- All-mode averaging (AMA): In the AMA, $\mathcal{O}^{(\mathrm{appx})}$ is estimated as

$$\mathcal{O}^{(\mathrm{AMA})} = \mathcal{O}[D^{-1}_{(\mathrm{all})}], \tag{4.49}$$

$$D^{-1}_{(\mathrm{all})}\eta = \sum_{i=0}^{N_{\mathrm{eig}}-1} \frac{1}{\lambda_i} v^{(i)} \otimes v^{(i)\dagger}\gamma_5\eta + H^{-1}\mathcal{P}_1\gamma_5\eta, \tag{4.50}$$

  where η is a source vector of linear equation and $\mathcal{P}_1$ is the projection operator into the high-mode subspace, as already introduced in the hybrid method. The form of $D^{-1}_{(\mathrm{all})}$ is similar to the hybrid method, but in the AMA the noisy estimator is not introduced in the

[2] The first condition is not necessary if we introduce randomness in the choice of the transformation, $g \in G$. Moreover, the final condition can be neglected if the cost of constructing $\mathcal{O}^{(\mathrm{appx})}$ is negligible.

high-mode part in general. Instead, the spatial position of the source vector is transformed by the symmetry transformation $g \in G$ and averaged.

Chapter 5

Application of the hybrid method to the HAL QCD method

At the beginning of my research, there are a few studies on the application of the all-to-all propagator to the HAL QCD method [26, 27]. In those studies, authors apply the LapH method [28], one of the famous techniques to treat all-to-all propagators in lattice QCD. The LapH method is based on the low-mode truncation using eigenstates of a gauge covariant Laplacian, and therefore all quark fields are automatically smeared. Since the HAL QCD method is sensitive to the locality of sink operators via a spatial dependence of the NBS wave function (which is one of the scheme dependence, as already discussed), authors investigate how the automatically smeared sink operator affects the behavior of the HAL QCD potential. As a result, authors report that the quark smearing due to the LapH method has a broad spatial extent and it enlarges the non-locality of the HAL QCD potential. The higher-order determination of the derivative expansion is mandatory to reproduce correct physical observables, but it is numerically expensive. Furthermore, to reduce the non-locality attributed to the LapH method, one needs a lot of eigenstates, which are also too expensive to calculate.

Under these circumstances, we employ another all-to-all technique, the hybrid method[29]. The hybrid method is free from the non-locality problem since it does not discard any high-mode information, and therefore it can be more suitable to the HAL QCD method than the LapH method. On the other hand, it additionally introduces the noisy estimators and corresponding errors, then we study how such noise contamination affects the HAL QCD potentials and how to reduce it. In this chapter, we introduce a series of our research on the hybrid method[30, 31].

5.1 $I = 2\,\pi\pi$ potential in the HAL QCD method with all-to-all propagators

In this section, we show the first study, the elastic $I = 2\ \pi\pi$ S-wave interaction [30]. The main purpose of this study is to understand how the HAL QCD potential is affected by the introduction of the hybrid method. We study several combinations of tunable parameters in the hybrid method and obtain useful insights for the appropriate choice of the parameters. Moreover, we compare

our result with one obtained from the wall source to clarify the effect of the hybrid method. The hybrid method enables us to take the smeared source with zero-momentum projection. As a result, it reproduces the consistent phase shift at an earlier timeslice than the conventional wall source, while the statistical error becomes larger.

5.1.1 Calculation of correlation functions

First, let us introduce details of estimation of correlation functions using the hybrid method. We define pion correlation functions as

$$C(t) = \sum_{\mathbf{x},\mathbf{y},t_0} \langle \pi^+(\mathbf{x}, t+t_0)\pi^-(\mathbf{y}, t_0)\rangle, \tag{5.1}$$

$$F^{I=2}_{\pi\pi,\mathbf{P}=\mathbf{0}}(\mathbf{r}, t) = \sum_{\mathbf{x},t_0} \langle \pi^+(\mathbf{x}+\mathbf{r}, t+t_0)\pi^+(\mathbf{x}, t+t_0)\overline{\mathcal{J}}^{I=2,A_1^+}_{\pi\pi}(t_0)\rangle, \tag{5.2}$$

where the source operator is defined as

$$\overline{\mathcal{J}}^{I=2,A_1^+}_{\pi\pi}(t_0) = \sum_{\mathbf{y_1},\mathbf{y_2}} \pi^-_{\text{local/smear}}(\mathbf{y_1}, t_0)\pi^-_{\text{local/smear}}(\mathbf{y_2}, t_0), \tag{5.3}$$

and pion operators are defined as

$$\pi^+(\mathbf{x}, t) = \bar{d}(\mathbf{x}, t)\gamma_5 u(\mathbf{x}, t), \tag{5.4}$$

$$\pi^-(\mathbf{x}, t) = \bar{u}(\mathbf{x}, t)\gamma_5 d(\mathbf{x}, t). \tag{5.5}$$

$\pi_{\text{local/smear}}$ at the source part represents a pion operator constructed by local or smeared quark fields. We note that in this study we only consider the center-of-mass frame. We compare our result to the conventional wall source calculation, whose definition is given as

$$\overline{\mathcal{J}}^{I=2,A_1^+}_{\pi\pi}(t_0) = \pi^-_{\text{wall}}(t_0)\pi^-_{\text{wall}}(t_0), \tag{5.6}$$

with

$$\pi^-_{\text{wall}} = \sum_{\mathbf{x},\mathbf{y}} \bar{u}(\mathbf{x}, t)\gamma_5 d(\mathbf{y}, t). \tag{5.7}$$

As discussed before, the wall source is free from the estimations of the all-to-all propagator.

The correlation function Eq.(5.2) can be written as the summation of the separated diagram and the connected diagram, as shown in Fig.5.1. Details of the Wick contraction are explained in AppendixD. In the following we discuss how those diagrams can be estimated by using the hybrid method.

FIGURE 5.1: Representative diagrams appearing in the $I = 2$ $\pi\pi$ correlation function. Gray arrows represent quark propagations and paired $\overline{q}q$ combinations correspond to each pion operators. In this cartoons, we show the source operators on the right hand side.

Estimation of separated diagram using the hybrid method

The contribution from the separated diagram is given as

$$(+)\sum_{\mathbf{y_1},\mathbf{y_2},\mathbf{x},t_0} \mathrm{tr}\left[D^{-1}(\mathbf{x}+\mathbf{r},t+t_0|\mathbf{y_1},t_0)\gamma_5 D^{-1}(\mathbf{y_1},t_0|\mathbf{x}+\mathbf{r},t+t_0)\gamma_5\right] \times \mathrm{tr}\left[D^{-1}(\mathbf{x},t+t_0|\mathbf{y_2},t_0)\gamma_5 D^{-1}(\mathbf{y_2},t_0|\mathbf{x},t+t_0)\gamma_5\right]. \tag{5.8}$$

The quark propagator can be estimated by the hybrid method as

$$D^{-1} = H^{-1}\gamma_5 \approx \sum_{i=0}^{N_{\mathrm{hl}}-1} u^{(i)} \otimes w^{\dagger(i)}\gamma_5, \tag{5.9}$$

$$w^{(i)}_{[r]} = \{\frac{v^{(0)}}{\lambda_0},...,\frac{v^{(N_{\mathrm{eig}}-1)}}{\lambda_{N_{\mathrm{eig}}-1}},\eta^{(0)}_{[r]},...,\eta^{(N_{\mathrm{dil}}-1)}_{[r]}\} \tag{5.10}$$

$$u^{(i)}_{[r]} = \{v^{(0)},...,v^{(N_{\mathrm{eig}}-1)},\psi^{(0)}_{[r]},...,\psi^{(N_{\mathrm{dil}}-1)}_{[r]}\} \tag{5.11}$$

$$N_{\mathrm{hl}} = N_{\mathrm{eig}} + N_{\mathrm{dil}}. \tag{5.12}$$

Then, by inserting this representation for all quark propagators in Eq. (5.8), we obtain

$$(+)\sum_{\mathbf{y_1},\mathbf{y_2},\mathbf{x},t_0}\sum_{i,j,k,l} O^{(i,j)}_{[r,s]}(\mathbf{r}+\mathbf{x},t+t_0)O^{(j,i)}_{[s,r]}(\mathbf{y_1},t_0)O^{(k,l)}_{[p,q]}(\mathbf{x},t+t_0)O^{(l,k)}_{[q,p]}(\mathbf{y_2},t_0), \tag{5.13}$$

where we define "hybrid operator" $O^{(i,j)}$ as

$$O^{(i,j)}_{[r,s]}(\mathbf{x},t) = \sum_{b,\beta} w^{\dagger(i)}_{[r]\ b\beta}(\mathbf{x},t)u^{(j)}_{[s]\ b\beta}(\mathbf{x},t). \tag{5.14}$$

(i,j,k,l) are indices of the hybrid list and (r,s,p,q) are identifiers of independent noise vectors. Since the summation of (i,j) is closed within two hybrid operators $O^{(i,j)}_{[r,s]}(\mathbf{r}+\mathbf{x},t+t_0)O^{(j,i)}_{[s,r]}(\mathbf{y_1},t_0)$ (and same for (k,l)), computational cost scales as $\mathcal{O}(N_{\mathrm{hl}}^2)$ in this diagram. The

hybrid operator is dense matrix with indices (i, j) on each lattice sites. Our numerical simulation is parallelized by dividing the spacetime sites on different MPI processes, then the further parallelization on the contraction of the hybrid indices is difficult. Typically $N_{\rm hl}$ takes $\mathcal{O}(10^2)$ and the contraction is the most time-consuming part of our simulation. To accelerate the contraction, we employ the BLAS routines for matrix operations.

To perform the noise average, one needs to estimate the diagrams by other sets of noise vectors (identified as, e.g., r', s', p', q') and average them. However, it requires more inversions, which are the second time-consuming part of the simulation. Alternatively, one can reduce noise contamination without additional costs for inversions by averaging permutated noise vectors ($(r, s, p, q) \to (P(r), P(s), P(p), P(q))$ with some permutation operation P).

Estimation of connected diagram using the hybrid method

The connected diagram is given as

$$(-)\sum_{\mathbf{y_1},\mathbf{y_2},\mathbf{x},t_0} \mathrm{tr}\big[D^{-1}(\mathbf{x}+\mathbf{r}, t+t_0; \mathbf{y_1}, t_0)\gamma_5 D^{-1}(\mathbf{y_1}, t_0; \mathbf{x}, t+t_0) \times \gamma_5 D^{-1}(\mathbf{x}, t+t_0; \mathbf{y_2}, t_0)\gamma_5 D^{-1}(\mathbf{y_2}, t_0; \mathbf{x}+\mathbf{r}, t+t_0)\gamma_5\big]. \tag{5.15}$$

As the case of the separated diagram, we can rewrite it in terms of the hybrid operator as

$$(-)\sum_{\mathbf{y_1},\mathbf{y_2},\mathbf{x},t_0}\sum_{i,j,k,l} O^{(i,j)}_{[r,s]}(\mathbf{r}+\mathbf{x}, t+t_0) O^{(j,k)}_{[s,p]}(\mathbf{y_1}, t_0) O^{(k,l)}_{[p,q]}(\mathbf{x}, t+t_0) O^{(l,i)}_{[q,r]}(\mathbf{y_2}, t_0). \tag{5.16}$$

At a glance it looks similar to the separated diagram, but the combination of the hybrid indices i, j, k, l (together with r, s, p, q) is different. In this case the summation is not closed in a part of the diagram, therefore its computation scales worse than the separated diagram. Naively its scaling is expected as $\mathcal{O}(N_{\rm hl}^4)$, but we can reduce it to $\mathcal{O}(N_{\rm hl}^3)$ by dividing the calculation into two steps: the first step is a construction of the matrix $M^{(i,k)} = \sum_j O^{(i,j)} O^{(j,k)}$, which scales $\mathcal{O}(N_{\rm hl}^3)$; the second is calculation of trace of a matrix product like $\sum_{i,k} M^{(i,k)} M'^{(k,i)}$, whose scaling is $\mathcal{O}(N_{\rm hl}^2)$.

Potential calculation

Once we obtain the correlation functions, we can calculate the interaction potential as discussed in Chap.3. The time-dependent HAL QCD method reads[61]

$$\left[\frac{\nabla^2}{m_\pi} - \frac{\partial}{\partial t} + \frac{1}{4m_\pi}\frac{\partial^2}{\partial t^2}\right] R(\mathbf{r}, t) = \int d^3\mathbf{r}' U(\mathbf{r}, \mathbf{r}') R(\mathbf{r}', t), \tag{5.17}$$

as long as t is large enough to suppress inelastic contributions in $R(\mathbf{r},t) \equiv F_{\pi\pi}^{I=2}(\mathbf{r},t)/C(t)^2$. The effective LO potential, we study in detail here, is given by

$$V^{\mathrm{LO}}(r) = \frac{\left[\frac{\nabla^2}{m_\pi} - \frac{\partial}{\partial t} + \frac{1}{4m_\pi}\frac{\partial^2}{\partial t^2}\right] R(\mathbf{r},t)}{R(\mathbf{r},t)}. \tag{5.18}$$

5.1.2 Numerical setup

We employ the $2+1$ flavor full QCD configuration generated by the CP-PACS+JLQCD Collaboration[63, 64] on a $16^3 \times 32$ lattice, with the Wilson-Clover fermion action[54] and the Iwasaki gauge action[55]. The parameters of lattice actions are summarized in Table5.1. The simulations are performed with a periodic boundary condition for all spacetime directions.

TABLE 5.1: Parameters of the gauge configuration

β	κ_{ud}	κ_s	c_{SW}	a [fm]	m_π[MeV]	m_ρ[MeV]
1.83	0.1376	0.1371	1.7610	0.1214	870	1229

As regards the hybrid method, we use a single noise vector for each propagator, and the noise vectors are generated by Z_4 random noises. We employ full color and spinor dilution for all cases, and take some different combinations of time and space dilutions. We also take some different values of N_{eig} to see dependence on it. The parameter setups used in this study is summarized in Table5.2, and details of dilutions can be found in AppendixC. Statistical errors are estimated by the jackknife method with bin-size 1 except for case 5a, where the bin-size is 6.

For the quark smearing, we employ the exponential smearing (Tsukuba-type) introduced in Chap.2 with the Coulomb gauge fixing. Smearing parameters are chosen as $A = 1, B = 0.47$ to achieve an early plateau of the pion mass. As seen in Fig.5.2, the smeared source actually suppresses the inelastic contamination in comparison to the local source result.

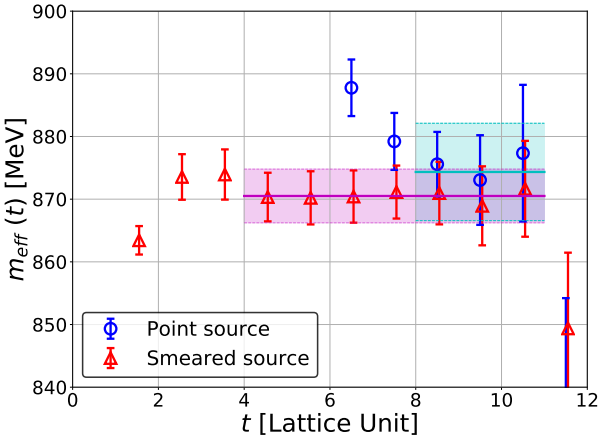

FIGURE 5.2: Effective mass of pion with local (blue circles) and smeared (red triangles) source operators. The horizontal lines gives the extracted pion mass, together with their statistical errors as light color bands.

Our numerical calculation is based on the lattice QCD codeset Bridge++[65]. All numerical calculations are performed in Cray XC40 in YITP, with a flat MPI parallelization of 2048 processes.

TABLE 5.2: Setups for the hybrid method. $N_{\rm eig}$ is the number of low eigenmodes for the all-to-all propagator, and the number of the noise vector for high eigenmodes is 1 for all cases. Color and spinor dilutions are always used.

	time dilution	space dilution	$N_{\rm eig}$	Source	$N_{\rm conf}$
case 1	full	none	100	point	20
case 2	full	$s2$ (even/odd)	100	point	20
case 3	16-interlace	$s2$ (even/odd)	100	point	20
case 4	16-interlace	$s2$ (even/odd)	100	smear	20
case 5	16-interlace	$s4$	100	smear	20
case 5a	16-interlace	$s4$	100	smear	60
case 6	16-interlace	$s2$ (even/odd)	200	point	20
case 7	16-interlace	$s2$ (even/odd)	484	smear	20

5.1.3 Results

Systematic study on parameter dependence of HAL QCD potential

Firstly, let us briefly discuss how the HAL QCD potential depends on the parameters of the hybrid method. Figure5.3 (Left) shows the effective LO potential obtained in case 1 at $t = 6$. The $I = 2$ $\pi\pi$ interaction is entirely repulsive. We observe that the data points have large statistical errors, which come from the additional noise contamination of the hybrid method. Furthermore, the large contamination mainly comes from the Laplacian term of Eq.(5.18) as seen in Fig.5.3 (Left). It suggests that for the HAL QCD method noise reduction along the spatial direction is almost mandatory, and it is intuitively understandable since the potential is extracted from the spatial dependence of the correlation function. Next, we investigate how the space dilution improves the potential. In Fig.5.3 (Right), we show two potentials with different parameter choices, namely case 1 and 2. The fluctuation of the potential data drastically decreases as expected if we employ space dilution. Furthermore, we find that the J-interlace time dilution can compensate the increase of $N_{\rm hl}$ without any additional contamination as long as we consider a small timeslice region of $t < J/2$.

The noise reduction can also be achieved by increasing $N_{\rm eig}$ since it reduces the relative segment of the propagator estimated by the noisy estimator. Figure5.4(Left) shows the $N_{\rm eig}$ dependence of the potential by comparing case 3 and case 6, and we can see that the statistical fluctuation indeed decreases. We also compare the effects of space dilution and increasing $N_{\rm eig}$ with the same computational cost (= same $N_{\rm hl}$) in Fig.5.4(Right). In this comparison, we observe that the increasing $N_{\rm eig}$ is slightly advantageous. Note that the improvement by increasing $N_{\rm eig}$

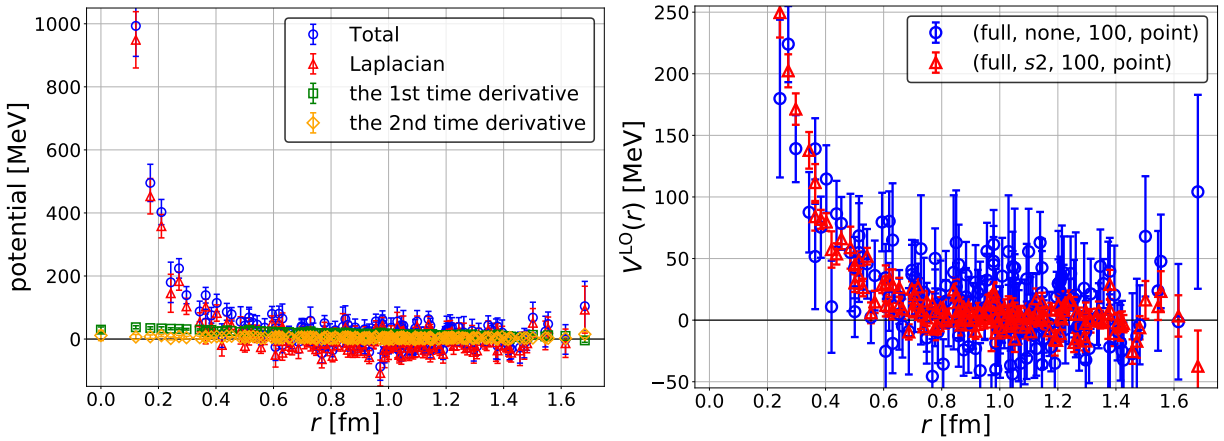

FIGURE 5.3: (Left) The potential from the hybrid method with parameters of case 1 at $t = 6$ (blue circles). We also show its breakdown to three contributions, the Laplacian (red triangles), the first time derivative (green squares), and the second time derivative (yellow diamonds). (Right) Dependence of the potential on space dilutions at $t = 6$.

strongly depends on the lattice simulation setup, therefore we can generally say that it is preferable to optimize N_{eig} as many as the cost for the eigenmode calculation remains subdominant.

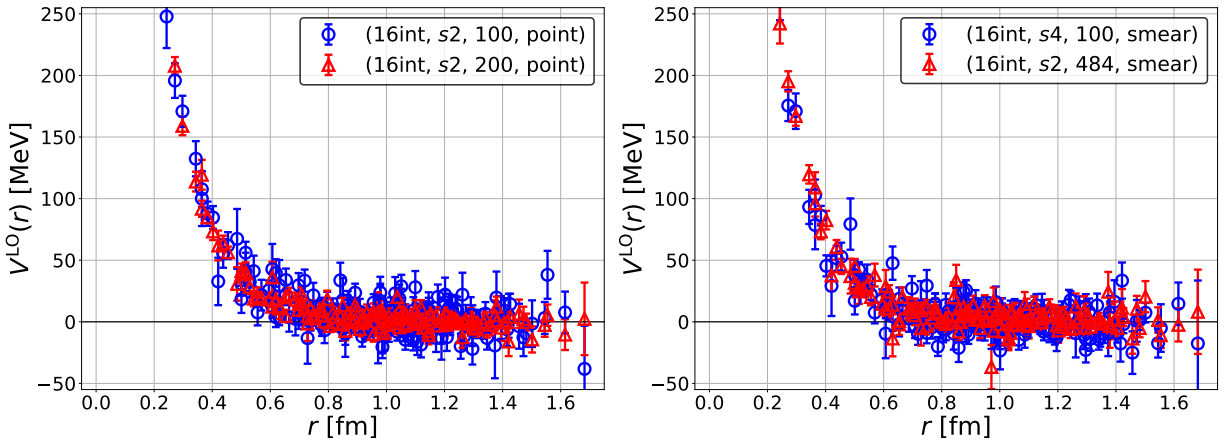

FIGURE 5.4: (Left) N_{eig} dependence of the potential between $N_{\mathrm{eig}} = 100$ (blue) and $N_{\mathrm{eig}} = 200$ (red). (Right) A comparison of the potential between case 5, (16-interlace, $s4$, smear) with $N_{\mathrm{eig}} = 100$ (blue), and case 7, (16-interlace, $s2$, smear) with $N_{\mathrm{eig}} = 484$ (red), in keeping the leading numerical cost dominated by $N_{\mathrm{hl}} = N_{\mathrm{eig}} + N_{\mathrm{dil}} = 868$ remaining.

Finally, we investigate the effect of the quark smearing. We find that the smearing allows the early time saturation as seen in Fig.5.5, but we must introduce a finer space dilution to keep statistical error comparable, as shown in Fig.5.6.

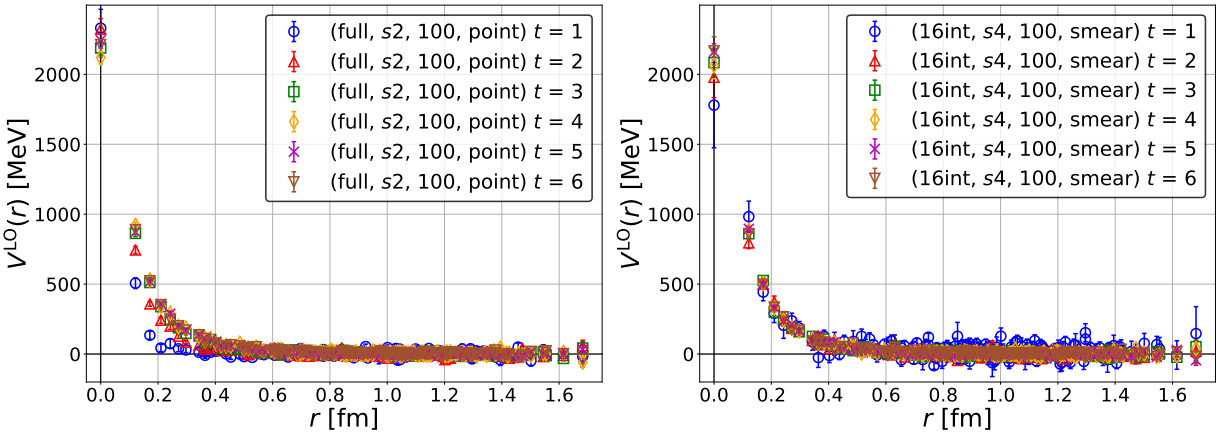

FIGURE 5.5: (Left) Dependence of the potential on t in case2 (full, $s2$, 100, point). (Right) The same one in case5 (16-interlace, $s4$, 100, smear).

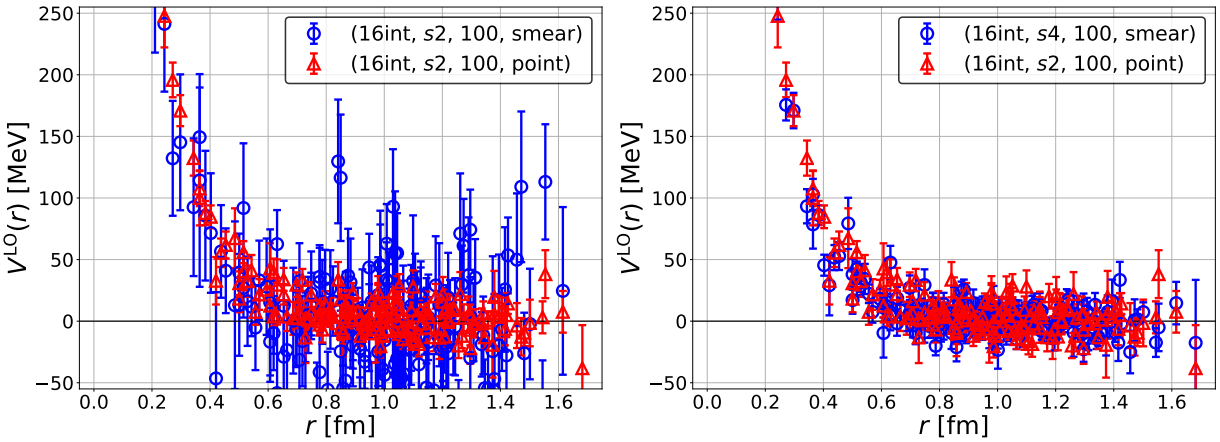

FIGURE 5.6: (Left) A comparison of the potential between the smeared source (case4) (blue circles) and the point source (case3) (red triangles) with 16-interlace time and $s2$ space dilution at $t = 6$. (Right) A comparison between the smeared source with 16-interlace time and $s4$ space dilution (case5) (blue circles) and the point source with 16-interlace time and $s2$ space dilution (case3)(red triangles) at $t = 6$.

From those studies, we obtain a general guideline for the parameter choice of the hybrid method. It is summarized as follows:

1. A finer spatial dilution should be used to reduce contamination to the HAL QCD potential.
2. A J-interlace time dilution can be used for the potential to be extracted at $t < J/2$, to reduce computational cost.
3. It is better to increase $N_{\rm eig}$ as many as possible within reasonable computational cost.
4. Quark smearing accumulates noise contamination, therefore additional spatial dilution is mandatory.

Comparison to the conventional result

Using the best parameter choice, we compare our result to the conventional HAL QCD calculation. In Figure5.7(Left), we compare our potential and that obtained with the wall source. Those potentials are almost consistent with each other, although our potential has larger statistical errors. To calculate the scattering phase shift, we fit our potential using the 2-Gaussian shape, $V(r) = a_0 e^{-r^2/a_1^2} + a_2 e^{-r^2/a_3^2}$. We also confirm that $k\cot\delta(k)$ shown in Fig.5.7(Right) agrees with the result of the Lüscher's method [26], as well as the wall source result. The important observation here is that we obtain correct physical observable at an earlier timeslice thanks to the smeared source. It is an advantageous feature achieved by introducing the all-to-all propagator.

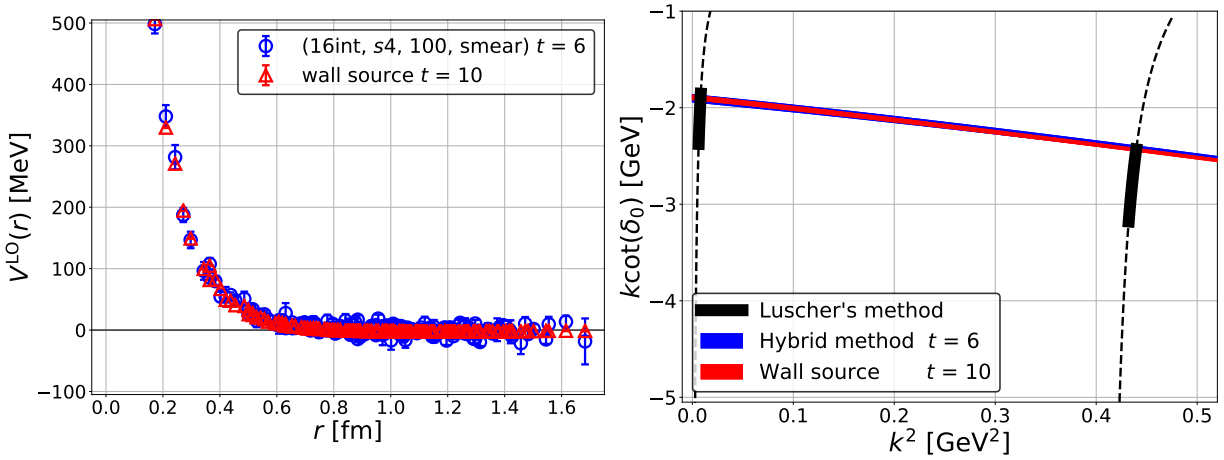

FIGURE 5.7: (Left) A comparison of the $I = 2$ $\pi\pi$ potentials, one from the hybrid method (blue circles) and the other from the wall quark source (red triangles). (Right) $k\cot\delta_0(k)$ as a function of k^2. Blue (red) bands correspond to the results from the HAL QCD method with the hybrid method (with the wall quark source). Black bands in the right figure correspond to the results from Lüscher's method [26].

5.2 The HAL QCD potential in $I = 1$ $\pi\pi$ system with the rho meson bound state

In this section, we discuss the second application of the hybrid method to the elastic $I = 1$ $\pi\pi$ P-wave interaction [31]. This study aims to verify that the combination of the HAL QCD method and the hybrid method allows reasonable calculations of diagrams involving the quark creation/annihilation. In this study, we employ the same gauge configuration as the $I = 2$ $\pi\pi$ study, where the ρ meson appears as a deeply bound state. Although this setup is quite unphysical, it reduces the computational cost and we can still investigate our primal interest, whether the hybrid method can appropriately treat the quark creation/annihilation diagrams.

5.2.1 Calculation of correlation functions

The correlation function of the elastic $I = 1$ $\pi\pi$ P-wave interaction is defined as

$$F(\mathbf{r}, t) = \sum_{\mathbf{x}, t_0} \langle (\pi\pi)_{I=1, I_z=0}(\mathbf{r}, t + t_0) \overline{\mathcal{J}}^{T_1^-}_{\pi\pi}(t_0) \rangle. \tag{5.19}$$

We employ the time-shifted sink operator

$$(\pi\pi)_{I=1, I_z=0}(\mathbf{r}, t) = \frac{1}{\sqrt{2}} \sum_{\mathbf{x}} \{\pi^+(\mathbf{r} + \mathbf{x}, t + \Delta t)\pi^-(\mathbf{x}, t) - \pi^-(\mathbf{r} + \mathbf{x}, t + \Delta t)\pi^+(\mathbf{x}, t)\}. \tag{5.20}$$

As discussed later, the non-zero time shift $\Delta t \neq 0$ may reduce the noise contamination coming from the quark creation/annihilation diagram. The source operator is chosen as the ρ-type,

$$\overline{\mathcal{J}}^{T_1^-}_{\rho; I=1, I_z=0}(t_0) = \sum_{\mathbf{x}} \bar{\rho}^0_3(\mathbf{x}, t), \tag{5.21}$$

where $\rho^0_3 = \bar{u}\gamma_3 u - \bar{d}\gamma_3 d$. The correlation function eq. (5.19) is estimated by the triangle diagrams shown in Fig.5.8. Let us discuss the estimation of the diagram next.

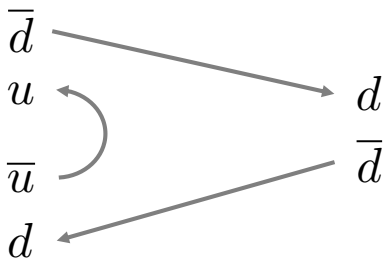

FIGURE 5.8: Representative diagram contributing to the correlation function with ρ-type source operator.

Estimation of triangle diagram using the hybrid method

The contribution of the triangle diagram is given as

$$(-)\sum_{\mathbf{x},\mathbf{z},\mathbf{t_0}} \mathrm{tr}\big[D^{-1}(\mathbf{x}+\mathbf{r},t{+}t_0{+}\Delta t;\mathbf{x},t{+}t_0)\gamma_5 D^{-1}(\mathbf{x},t{+}t_0;\mathbf{z},t_0)\gamma_3 D^{-1}(\mathbf{z},t_0;\mathbf{x}+\mathbf{r},t{+}t_0{+}\Delta t)\gamma_5\big]. \tag{5.22}$$

Inserting the propagators estimated by the hybrid method, we can rewrite it as

$$(-)\sum_{i,j,k}\sum_{\mathbf{x},t_0} O^{(i,j)}_{[r,s]}(\mathbf{x}+\mathbf{r},t+t_0+\Delta t)O^{(j,k)}_{3[s,p]}(t_0)O^{(k,i)}_{[p,r]}(\mathbf{x},t+t_0), \tag{5.23}$$

where

$$O^{(i,j)}_{3[r,s]}(t)\equiv\sum_{\mathbf{x}} w^{\dagger(i)}_{[r]}(\mathbf{x},t)\gamma_5\gamma_3 u^{(j)}_{[s]}(\mathbf{x},t),\quad O^{(i,j)}_{[r,s]}(\mathbf{x},t)\equiv w^{\dagger(i)}_{[r]}(\mathbf{x},t)u^{(j)}_{[s]}(\mathbf{x},t). \tag{5.24}$$

Potential calculation

We study the effective LO potential,

$$V^{\mathrm{LO}}_{\Delta t}(r)=\frac{\left[\dfrac{\nabla^2}{m_\pi}-\dfrac{\partial}{\partial t}+\dfrac{1}{4m_\pi}\dfrac{\partial^2}{\partial t^2}\right]R(\mathbf{r},t,\Delta t)}{R(\mathbf{r},t,\Delta t)}. \tag{5.25}$$

In the P-wave interaction, however, the NBS wave function is not rotationally invariant due to the angular dependence of spherical harmonics. In such a case, we can rewrite the above definition to improve signals by the rotational invariance of the potential as [66]

$$V^{\mathrm{LO}}_{\Delta t}(r)=\frac{\sum_{g\in O_h}R^\dagger(g\mathbf{r},t,\Delta t)\left[\dfrac{\nabla^2}{m_\pi}-\dfrac{\partial}{\partial t}+\dfrac{1}{4m_\pi}\dfrac{\partial^2}{\partial t^2}\right]R(g\mathbf{r},t,\Delta t)}{\sum_{g\in O_h}R^\dagger(g\mathbf{r},t,\Delta t)R(g\mathbf{r},t,\Delta t)}, \tag{5.26}$$

where the $g\in O_h$ is an element of the cubic rotation group O_h. We employ this improved definition in this study instead of the original one.

5.2.2 Numerical setup

We employ the same gauge configuration as the $I=2$ $\pi\pi$ interaction. The details are already discussed in Sect.5.1. In this configuration, the ρ meson appears as the deeply bound state with a relative energy $m_\rho-2m_\pi\approx-510$ [MeV].

The numerical setup are summarized in Table5.3 and 5.4. In case 1a and 1b, we average over $4\times 3!=24$ different noise samples ($3!=6$ samples for each set using the permutation of r,s,p). The parameters of case 1a, 1b in Tab.5.4 is an improved choice after observing that the calculation with the same parameters in the $I=2$ $\pi\pi$ calculation (case 0 in Tab.5.4) is

TABLE 5.3: Numerical setup for the calculations.

	Source	Scheme	$N_{\rm conf}$	Stat. error
case 0	point	equal-time ($\Delta t = 0$)	20	jackknife with bin–size 1
case 1a	smear	different-time ($\Delta t = 1$)	20	jackknife with bin–size 1
case 1b	smear	different-time ($\Delta t = 1$)	60	jackknife with bin–size 6

TABLE 5.4: Setups for the hybrid method in our calculation. $N_{\rm eig}$ is the number of low eigenmodes for the all-to-all propagator. Color and spinor dilutions are always used.

	time dilution	space dilution	$N_{\rm eig}$
case 0	16-interlace	$s2$	100
case 1a, 1b (src-to-sink)	16-interlace	$s4$	100
case 1a, 1b (sink-to-sink)	4-interlace	$s8 \times s2$	100

too noisy to obtain the reasonable potential, which will be briefly discussed later. As regards the smearing, we continuously employ the exponential smearing (Tsukuba-type) to remove inelastic contamination as early as possible. Values of the smearing parameters are the same as the $I = 2$ $\pi\pi$ study.

This calculation is performed on Cray XC40 in YITP and HOKUSAI Big-Waterfall in RIKEN, with a flat MPI parallelization of 2048 processes.

5.2.3 Results

Breakdown of naive application of the hybrid method and improvement

We first consider the calculation with the same parameters as the case 3 in the $I = 2$ $\pi\pi$ calculation, since they give a precise potential at $t < 8$ (see Fig.5.4 (Left)). Figure 5.9 (Left) shows the potential at $t = 6$. As seen, the resultant potential is extremely noisy and we cannot reproduce

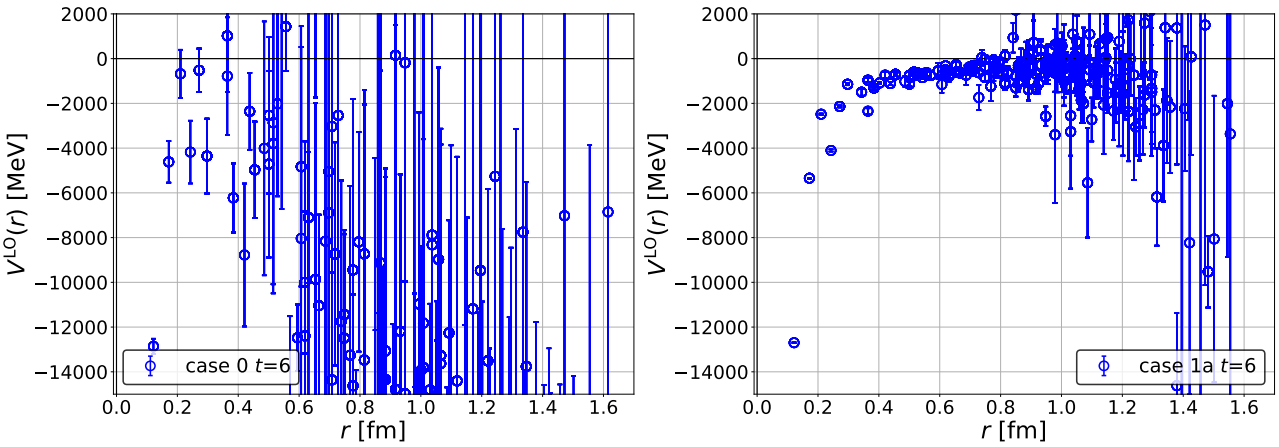

FIGURE 5.9: (Left) The potential at $t = 6$ in case 0 (the same setup as case 3 in Ref. [30]). (Right) The potential at $t = 6$ in case 1a.

any information from it. We suspect that this large fluctuation is caused by noise contamination from the sink-to-sink propagator because of the absence of the equal-time quark propagation in the $I = 2$ case.

To suppress such contamination, we additionally employ the following three noise reductions:

- Non-zero relative time ($\Delta t \neq 0$) scheme for avoiding the equal-time propagation at the sink operator.
- Finer spatial dilution in an estimation of the sink-to-sink propagator.
- Average over the increased number of noise vectors.

The potential after the additional noise reduction (case 1a) at $t = 6$ is shown in Fig.5.9 (Right). Thanks to the noise reductions, the statistical fluctuation drastically reduces [1]. The interaction shows a strong attraction without a repulsive core, which suggests that the existence of the bound state corresponding to the ρ meson. We also observe some non-smooth behavior in a short-distance part of the potential. It probably comes from higher partial wave contaminations (in this case $l = 3$), as already observed in previous HAL QCD studies.

Physical observables

To extract the physical observables, we fit the potential by using the 3-Gaussian shape as

$$V(r) = a_0 e^{-r^2/a_1^2} + a_2 e^{-r^2/a_3^2} + a_4 e^{-r^2/a_5^2}. \tag{5.27}$$

Since our potential happens to have a long tail structure, we consider the nearest-neighbor finite volume effect of the periodic boundary condition in the fit,

$$V(\mathbf{r})_{\mathrm{PBC}} = V(\mathbf{r}) + \sum_{\mathbf{n}\in\{(0,0,\pm1),(0,\pm1,0),(\pm1,0,0)\}} V(\mathbf{r} + L\mathbf{n}). \tag{5.28}$$

The fit result is given as a red line in Fig.5.10 (Left). We then calculate the ground state energy by using the Gaussian expansion method(GEM) [67] and obtain the binding energy as

$$E_{\mathrm{bind}} = 668 \pm 24_{\mathrm{stat}} \begin{pmatrix} +69 \\ -151 \end{pmatrix}_{\mathrm{sys(time\ dep.)}} \mathrm{MeV}, \tag{5.29}$$

where the first error is statistical, and the second error is the systematic one estimated by the potential at different timeslices, $t = 5, 6, 7$. Since we expect that the ρ meson appears as a deeply bound state around $E_{\mathrm{bind}} = |m_\rho - 2m_\pi| \approx 515$ MeV, the result is roughly consistent within a large systematic error.

[1] In this study, we do not specify which noise reduction contributes the most since it needs many calculations with other setups. Instead, we focus on increasing the statistics to extract information of the ρ meson.

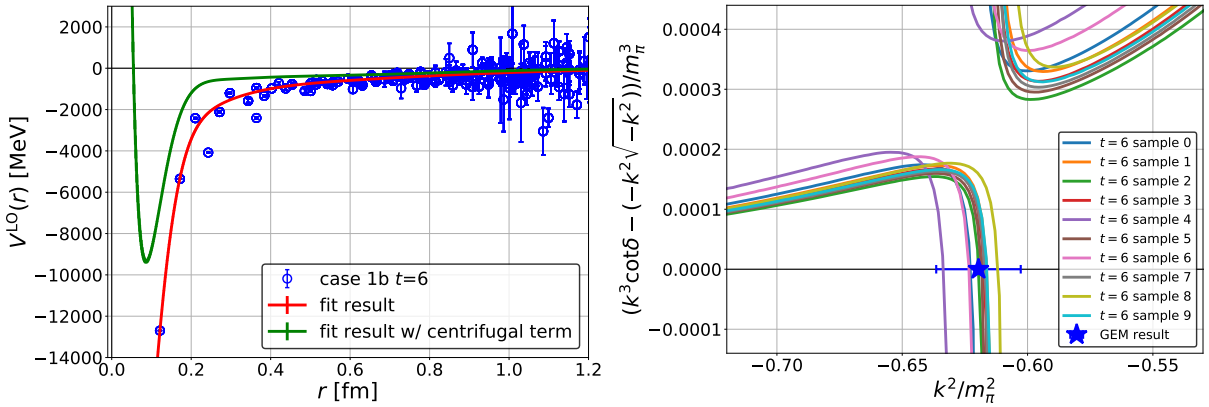

FIGURE 5.10: (Left) Fitting result at $t = 6$. Blue points are the original data, and red line shows the fitting result. Green line is the fitting result curve with the centrifugal potential term with $l = 1$, $V_c(r) = \frac{1}{m_\pi}\frac{1\cdot 2}{r^2}$. (Right) A difference between $k^3\cot\delta_1(k)$ and $-k^2\sqrt{-k^2}$ around the intersection for each jackknife sample, together with k^2 corresponding to the binding energy obtained by the Gaussian expansion method (blue solid star). It can be seen that all samples satisfy the physical pole condition and have a discontinuity, which typically appears for a deeply-bound system.

Finally, in order to verify the extracted negative energy state is a physical bound pole, we study the behavior of the $k^3\cot\delta_1(k)$ in a negative energy region. The P-wave physical bound state condition is given as

$$\frac{d}{dk^2}\left[k^3\cot\delta_1(k) - (-k^2\sqrt{-k^2})\right]\Big|_{k^2=-\kappa_b^2} < 0. \tag{5.30}$$

Figure5.10(Right) shows the behavior of our $k^3\cot\delta_1(k) - (-k^2\sqrt{-k^2})$ around the negative energy pole. It indicates that our result indeed satisfies the physical pole condition.

In summary, we confirm that our potential can reproduce a physical pole corresponding to the ρ meson if we sufficiently reduce the noise contamination coming from the estimation of the equal-time quark propagation.

5.3 Exploration of better calculation scheme

The series of our study using the hybrid method reveals that the precise potentials can be obtained if the noise contamination is sufficiently removed. On the other hand, we also find unfavorable points for applications to large-scale simulations. The first bottleneck is that it consumes a lot of memory space in numerical calculations. The hybrid lists $w^{(i)}(x), u^{(i)}(x)$ typically have $N_{\mathrm{hl}} \sim \mathcal{O}(10^2)$ elements together with the color, spinor and spacetime indices. Furthermore, the hybrid operators $O^{(i,j)}(x)$ which are constructed in contraction procedures costs more, namely $N_{\mathrm{hl}}^2 \sim \mathcal{O}(10^4)$ elements in addition to the spacetime index x. The larger lattice size we employ, the more memory space the operators consume. One possible remedy is to enlarge the parallelization of the computation so as to compress the local volume of spacetime index x in

each MPI process. However, it is sometimes difficult in practice due to the restriction of computational resources. Too much parallelization may also lead to a worse performance due to the busy communications between the MPI processes. The second concerning point is the existence of dense matrix products on each lattice site. As discussed, the hybrid operator is a $N_{\rm hl} \times N_{\rm hl}$ complex dense matrix. Since we divide the lattice volume by MPI parallelization, we need to perform the products of the hybrid operator without any MPI parallelization. Furthermore, our calculation scales $\mathcal{O}(N_{\rm hl}^3)$ in some diagrams, and it easily explodes by increasing $N_{\rm hl}$. It may be partly improved by introducing, for example, the BLAS routine or some thread parallelization, but it is preferable to reduce such index contractions in the first place. In addition to the numerical issues above, the hybrid method itself is very noisy in the HAL QCD method. Therefore we have to consume a lot of computational resources to reduce the noise contamination by repeating calculations with different combinations of noise vectors or taking finer dilutions within the restriction of the memory usage and calculation time.

Motivated by those issues, we try to establish a better calculation scheme for large-scale simulations by considering not only the hybrid method but also other numerical techniques in lattice QCD. Required features of the new calculation scheme are:

1. Small memory usage
2. Few additional index contractions which cannot be parallelized
3. Less noise contamination

Those conditions are not independent of each other, and the smartest way to achieve them simultaneously is to reduce the number of insertion of the noisy estimator in some way. Indeed, it leads to the fewer appearance of the noise indices $(i, j, \cdots)$, and their contraction is expected to scale as less than $\mathcal{O}(N_{\rm hl}^3)$. Intermediate calculations like dense matrix products in the hybrid method also disappear, as well as we do not need to put huge intermediate data on memory space. The noise contamination from the noisy estimator also decreases in the first place. Fortunately, we find that the techniques we introduce in Chap.4 and their combinations can achieve the fewer usage of the noisy estimator, inspired by the previous work on the Lüshcer's method [68].

To understand the situation, let us consider the $I = 2$ $\pi\pi$ calculation for example. As discussed before, the separated diagram and connected diagram contribute to the correlation function and they are given as

$$(+) \sum_{\mathbf{y_1},\mathbf{y_2},\mathbf{x},t_0} \mathrm{tr}\left[D^{-1}(\mathbf{x}+\mathbf{r}, t+t_0|\mathbf{y_1}, t_0)\gamma_5 D^{-1}(\mathbf{y_1}, t_0|\mathbf{x}+\mathbf{r}, t+t_0)\gamma_5\right] \times \mathrm{tr}\left[D^{-1}(\mathbf{x}, t+t_0|\mathbf{y_2}, t_0)\gamma_5 D^{-1}(\mathbf{y_2}, t_0|\mathbf{x}, t+t_0)\gamma_5\right], \tag{5.31}$$

and

$$(-)\sum_{\mathbf{y_1},\mathbf{y_2},\mathbf{x},t_0}\mathrm{tr}\Big[D^{-1}(\mathbf{x}+\mathbf{r},t+t_0|\mathbf{y_1},t_0)\gamma_5 D^{-1}(\mathbf{y_1},t_0|\mathbf{x},t+t_0) \times\gamma_5 D^{-1}(\mathbf{x},t+t_0|\mathbf{y_2},t_0)\gamma_5 D^{-1}(\mathbf{y_2},t_0|\mathbf{x}+\mathbf{r},t+t_0)\gamma_5\Big], \tag{5.32}$$

respectively. Within the framework of the hybrid method, we have to introduce 4 noisy estimators to calculate each diagrams. As you notice, however, both of them have the source structures to which we can apply the one-end trick like

$$\cdots\sum_{\mathbf{y}} D^{-1}(\mathbf{x}_1,t_1|\mathbf{y},t_0)\Gamma D^{-1}(\mathbf{y},t_0|\mathbf{x}_2,t_2)\cdots. \tag{5.33}$$

Applying the one-end trick for each pion operators in the source part, we can calculate traces of the separated diagram as

$$\begin{aligned}
\sum_{\mathbf{y}}\ \mathrm{tr}\ &\left[D^{-1}(\mathbf{x},t|\mathbf{y},t_0)\gamma_5 D^{-1}(\mathbf{y},t_0|\mathbf{x},t)\gamma_5\right] && (5.34)\\
\approx\ &\sum_i\sum_{\mathbf{y},\mathbf{z}}\mathrm{tr}\left[D^{-1}(\mathbf{x},t|\mathbf{y},t_0)\eta^{(i)}(\mathbf{y})\otimes\eta^{(i)\dagger}(\mathbf{z})\gamma_5 D^{-1}(\mathbf{z},t_0;\mathbf{x},t)\gamma_5\right] && (5.35)\\
=\ &\sum_i\sum_{\mathbf{y},\mathbf{z}}\mathrm{tr}\left[D^{-1}(\mathbf{x},t|\mathbf{y},t_0)\eta^{(i)}(\mathbf{y})\otimes\left(D^{-1}(\mathbf{x},t|\mathbf{z},t_0)\eta^{(i)}(\mathbf{z})\right)^\dagger\right] && (5.36)\\
=\ &\sum_i \xi^{(i)\dagger}_{t_0}(\mathbf{x},t)\cdot\xi^{(i)}_{t_0}(\mathbf{x},t), && (5.37)
\end{aligned}$$

where a dot symbol represents an inner product of the color and spinor indices and we do not consider noise average here. At the end of the day, the separated diagram can be calculated as

$$(+)\sum_{\mathbf{x},t_0}\sum_{i,j}|\xi^{(i)}_{t_0[r]}(\mathbf{x}+\mathbf{r},t+t_0)|^2\,|\xi^{(j)}_{t_0[s]}(\mathbf{x},t+t_0)|^2. \tag{5.38}$$

The same discussion leads

$$(-)\sum_{\mathbf{x},t_0}\sum_{i,j}\left(\xi^{(i)\dagger}_{t_0[r]}(\mathbf{x}+\mathbf{r},t+t_0)\cdot\xi^{(j)}_{t_0[s]}(\mathbf{x}+\mathbf{r},t+t_0)\right)\ \left(\xi^{(j)\dagger}_{t_0[s]}(\mathbf{x},t+t_0)\cdot\xi^{(i)}_{t_0[r]}(\mathbf{x},t+t_0)\right), \tag{5.39}$$

for the connected diagram. The insertions of the noisy estimators now decrease from 4 to 2 in both diagrams. The scaling of the contraction is reduced to at most $\mathcal{O}(N^2_{\mathrm{dil}})$, where N_{dil} is the number of elements of indices (i,j).

Figure5.11 shows a comparison of the $I=2$ $\pi\pi$ potentials obtained by the hybrid method and the one-end trick. We can see that their entire behavior agrees with each other, and the noisy behavior observed in the case of the hybrid method is drastically reduced by the one-end trick. As regards the computational cost, an elapsed time to obtain the potential in Fig.5.11 reduces by a factor of $\sim 1/8$ in comparison to the hybrid method, together with $\sim 1/7$ times smaller

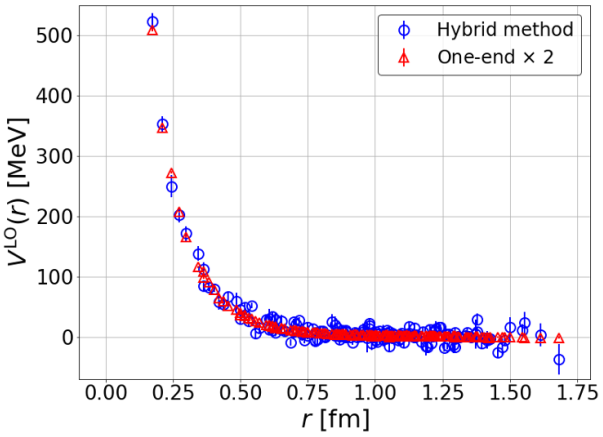

FIGURE 5.11: Effective LO potentials of $I = 2$ $\pi\pi$ S-wave interaction obtained by using the hybrid method (blue) and the one-end trick (red).

statistical errors on average over different r. This fact indicates that an approximately $\times 392 (= 8 \times 7^2)$ statistical improvement is achieved thanks to the one-end trick. We get confidence for the new scheme in this test calculation, then move on to the $I = 1$ $\pi\pi$ interaction with a more realistic situation where the ρ meson appears as a resonance state. This is the next result of this thesis.

Chapter 6

Emergence of the ρ resonance from the HAL QCD potential in lattice QCD

In this chapter, we discuss our recent result on the ρ resonance[48]. We employ the new calculation scheme to handle all-to-all propagators and study a more realistic situation, where the ρ meson appears as a resonance. The new scheme allows us to determine the non-local $I = 1$ $\pi\pi$ interaction at the next-to-next-to-leading order (NNLO) in the derivative expansion for the first time. The extracted potential reproduces a typical resonant behavior corresponding to the ρ resonance, although there is still a remaining truncation error of the derivative expansion.

6.1 Calculation of correlation functions by the improved scheme

The correlation functions for the $I = 1$ $\pi\pi$ P-wave interaction are defined as

$$C(t - t_0) = \sum_{\mathbf{x},\mathbf{y}} e^{i\mathbf{p}\cdot\mathbf{y}} e^{-i\mathbf{p}\cdot\mathbf{x}} \langle \pi^+(\mathbf{x}, t)\pi^-(\mathbf{y}, t_0)\rangle, \tag{6.1}$$

$$F^{I=1}_{\pi\pi,\mathbf{P}=\mathbf{0}}(\mathbf{r}, t - t_0) = \sum_{t_0} \langle (\pi\pi)_{I=1,I_z=0}(\mathbf{r}, t)\overline{\mathcal{J}}^{T_1^-}_{I=1,I_z=0}(t_0)\rangle, \tag{6.2}$$

where we only consider the center-of-mass frame. We employ the smeared-sink operator in this study,

$$(\pi\pi)_{I=1,I_z=0}(\mathbf{r}, t) = \frac{1}{\sqrt{2}}\{\pi^+_{\text{smear}}(\mathbf{r} + \mathbf{x}, t)\pi^-_{\text{smear}}(\mathbf{x}, t) - \pi^-_{\text{smear}}(\mathbf{r} + \mathbf{x}, t)\pi^+_{\text{smear}}(\mathbf{x}, t)\}. \tag{6.3}$$

The reason why we choose this operator is discussed in Appendix E. The source operators are chosen as

$$\overline{\mathcal{J}}^{T_1^-}_{\rho,I=1,I_z=0}(t_0) = \overline{\rho}^0_3(t_0), \tag{6.4}$$

$$\overline{\mathcal{J}}^{T_1^-}_{\pi\pi,I=1,I_z=0}(t_0) = \overline{(\pi\pi)}_{I=1,I_z=0}(\mathbf{p}_3, t_0), \tag{6.5}$$

where $\mathbf{p}_3 = (0, 0, 2\pi/L)$ is a back-to-back relative momentum of two pion operators. $\overline{(\pi\pi)}_{I=1,I_z=0}(\mathbf{p}, t)$ and $\overline{\rho}^0_3$ are defined as

$$\overline{\rho}^0_3(t) = \sum_{\mathbf{z}} \frac{1}{\sqrt{2}} \left(\bar{u}(\mathbf{z}, t)\gamma_3 u(\mathbf{z}, t) - \bar{d}(\mathbf{z}, t)\gamma_3 d(\mathbf{z}, t)\right) \tag{6.6}$$

$$\overline{(\pi\pi)}_{I=1,I_z=0}(\mathbf{p}, t) = \frac{1}{\sqrt{2}} \sum_{\mathbf{y_1},\mathbf{y_2}} e^{-i\mathbf{p}\cdot\mathbf{y_1}} e^{i\mathbf{p}\cdot\mathbf{y_2}} \left(\pi^-(\mathbf{y_1}, t)\pi^+(\mathbf{y_2}, t) - \pi^+(\mathbf{y_1}, t)\pi^-(\mathbf{y_2}, t)\right) \tag{6.7}$$

The effective LO potentials are obtained as before,

$$V_i^{\mathrm{LO}}(r) = \frac{\sum_{g\in O_h} R_i^\dagger(g\mathbf{r}, t) \left[\frac{\nabla^2}{m_\pi} - \frac{\partial}{\partial t} + \frac{1}{4m_\pi}\frac{\partial^2}{\partial t^2}\right] R_i(g\mathbf{r}, t)}{\sum_{g\in O_h} R_i^\dagger(g\mathbf{r}, t) R_i(g\mathbf{r}, t)}, \tag{6.8}$$

where R_i $(i = \rho, \pi\pi)$ are normalized correlation functions with different source operators $\overline{\mathcal{J}}_i(t_0)$ $(i = \rho, \pi\pi)$. We also determine the effective N^{2}LO potential $U^{\mathrm{N^2LO}}(\mathbf{r}, \mathbf{r}') = (V_0^{\mathrm{N^2LO}} + V_2^{\mathrm{N^2LO}}\nabla^2)\delta(\mathbf{r} - \mathbf{r}')$ by solving the following linear equations [69]:

$$\begin{pmatrix} 1 & \nabla^2 R_\rho(\mathbf{r}, t)/R_\rho(\mathbf{r}, t) \\ 1 & \nabla^2 R_{\pi\pi}(\mathbf{r}, t)/R_{\pi\pi}(\mathbf{r}, t) \end{pmatrix} \begin{pmatrix} V_0^{\mathrm{N^2LO}}(r) \\ V_2^{\mathrm{N^2LO}}(r) \end{pmatrix} = \begin{pmatrix} V_\rho^{\mathrm{LO}}(r) \\ V_{\pi\pi}^{\mathrm{LO}}(r) \end{pmatrix}. \tag{6.9}$$

We study the systematics of the derivative expansion by those effective potentials.

The correlation function with the $\pi\pi$-type source consists of the separated diagram and box diagram. The ρ-type source induces the triangle diagram, as introduced before. Figure 6.1 summarizes representative diagrams appearing in the correlation functions, and the techniques utilized in the evaluations of quark propagator are shown by different colors and symbols. The details of the Wick contraction are given in Appendix D. Here we focus on details of numerical evaluation of each diagram based on the new calculation scheme.

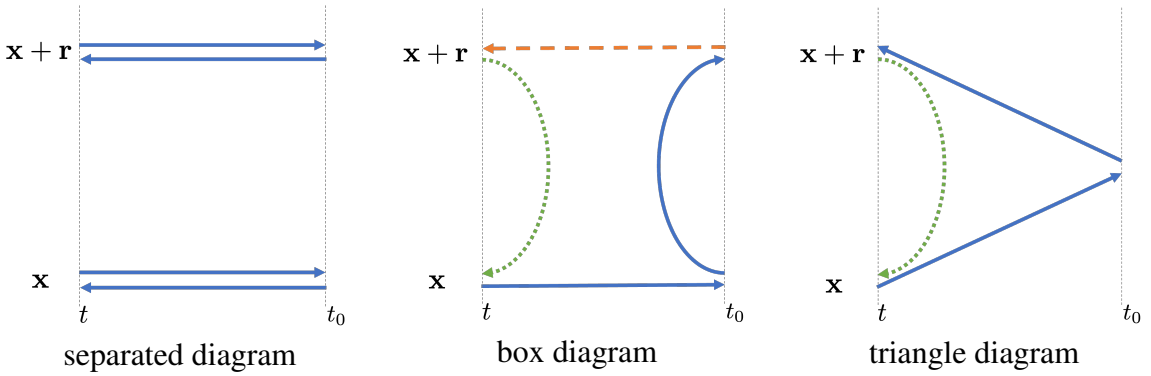

FIGURE 6.1: Representative diagrams appeared in this study. Blue solid, orange dashed and green dotted lines are calculated with the one-end trick, sequential propagator and point-to-all propagator, respectively. Statistical improvement by the CAA is also employed for green dotted lines.

6.1.1 Separated diagram

The separated diagram in Fig. 6.1 is written in terms of quark propagators as

$$G^{\rm sep}_{\mathbf{x};t_0}(\mathbf{r},t) = (+)\sum_{\mathbf{y_1},\mathbf{y_2}} e^{i\mathbf{p_z}\cdot\mathbf{y_1}}e^{-i\mathbf{p_z}\cdot\mathbf{y_2}}{\rm tr}\left[D^{-1}(\mathbf{x}+\mathbf{r},t|\mathbf{y_1},t_0)\gamma_5 D^{-1}(\mathbf{y_1},t_0|\mathbf{x}+\mathbf{r},t)\gamma_5\right] \times {\rm tr}\left[D^{-1}(\mathbf{x},t|\mathbf{y_2},t_0)\gamma_5 D^{-1}(\mathbf{y_2},t_0|\mathbf{x},t)\gamma_5\right]. \tag{6.10}$$

By using the one-end trick twice, we obtain

$$G^{\rm sep}_{\mathbf{x};t_0}(\mathbf{r},t) = (+)\sum_{i,j}\left(\chi^{(i)\dagger}_{\gamma_5,t_0[r]}(\mathbf{x}+\mathbf{r},t)\cdot\xi^{(i)}_{\mathbf{p}_z,t_0[r]}(\mathbf{x}+\mathbf{r},t)\right)\left(\chi^{(j)\dagger}_{\gamma_5,t_0[s]}(\mathbf{x},t)\cdot\xi^{(j)}_{-\mathbf{p}_z,t_0[s]}(\mathbf{x},t)\right), \tag{6.11}$$

where i,j are indices for dilutions and r,s distinguish independent noise vectors. In practice, the coordinate $\mathbf{x}$ is averaged over the whole space to reduce the statistical fluctuation,

$$G^{\rm sep}_{t_0}(\mathbf{r},t) = \frac{1}{L^3}\sum_{\mathbf{x}} G^{\rm sep}_{\mathbf{x};t_0}(\mathbf{r},t). \tag{6.12}$$

6.1.2 Box diagrams

The box diagram shown in Fig. 6.1 is given as

$$G^{\rm box}_{\mathbf{x};t_0}(\mathbf{r},t) = (-)\sum_{\mathbf{y_1},\mathbf{y_2}} e^{i\mathbf{p_z}\cdot\mathbf{y_1}}e^{-i\mathbf{p_z}\cdot\mathbf{y_2}}{\rm tr}[D^{-1}(\mathbf{x}+\mathbf{r},t|\mathbf{y_1},t_0)\gamma_5 D^{-1}(\mathbf{y_1},t_0|\mathbf{y_2},t_0)\gamma_5 \times D^{-1}(\mathbf{y_2},t_0|\mathbf{x},t)\gamma_5 D^{-1}(\mathbf{x},t|\mathbf{r}+\mathbf{x},t)\gamma_5]. \tag{6.13}$$

We first insert the one-end trick to a summation of $\mathbf{y_2}$,

$$(-)\sum_i\sum_{\mathbf{y_1}} e^{i\mathbf{p_z}\cdot\mathbf{y_1}}{\rm tr}[D^{-1}(\mathbf{x}+\mathbf{r},t|\mathbf{y_1},t_0)\gamma_5\xi^{(i)}_{-\mathbf{p}_z,t_0[r]}(\mathbf{y_1},t_0)\chi^{(i)\dagger}_{\gamma_5,t_0[r]}(\mathbf{x},t)D^{-1}(\mathbf{x},t|\mathbf{r}+\mathbf{x},t)\gamma_5]. \tag{6.14}$$

An another all-to-all propagator $D^{-1}(\mathbf{x}+\mathbf{r},t|\mathbf{y_1},t_0)$ is exactly calculated by the sequential propagator technique[33], where we solve a linear equation

$$\left(D\zeta\right)(x) = e^{i\mathbf{p_z}\cdot\mathbf{x}}\gamma_5\xi^{(i)}_{-\mathbf{p}_z,t_0[r]}(\mathbf{x},t)\delta_{t,t_0}, \tag{6.15}$$

whose solution ζ gives

$$\zeta^{(i)}_{\mathbf{p_z},-\mathbf{p_z},t_0[r]}(\mathbf{x},t) = \sum_{\mathbf{y_1}} D^{-1}(\mathbf{x},t|\mathbf{y_1},t_0)\gamma_5\xi^{(i)}_{-\mathbf{p}_z,t_0[r]}(\mathbf{y_1},t_0)e^{i\mathbf{p_z}\cdot\mathbf{y_1}}. \tag{6.16}$$

Substituting Eq. (6.16) into Eq. (6.14), we obtain

$$G^{\rm box}_{\mathbf{x};t_0}(\mathbf{r},t) = (-)\sum_i \chi^{(i)\dagger}_{\gamma_5,t_0[r]}(\mathbf{x},t) H^{-1}(\mathbf{x},t|\mathbf{r}+\mathbf{x},t)\zeta^{(i)}_{\mathbf{p_z},-\mathbf{p_z},t_0[r]}(\mathbf{r}+\mathbf{x},t), \tag{6.17}$$

where H^{-1} is an inverse of the hermitized Dirac operator $H = \gamma_5 D$.

To increase statistics of the box diagrams, we employ the covariant approximation averaging (CAA) for $\mathbf{x}$, which is given by

$$G^{\rm box,imp}_{\mathbf{x_0};t_0}(\mathbf{r},t) = G^{\rm box,exact}_{\mathbf{x_0};t_0}(\mathbf{r},t) - G^{\rm box,relaxed}_{\mathbf{x_0};t_0}(\mathbf{r},t) + \frac{1}{N_G}\sum_{\mathbf{x}'} G^{\rm box,relaxed}_{\mathbf{x}';t_0}(\mathbf{r},t), \tag{6.18}$$

where N_G is the number of a summation over $\mathbf{x}'$. Here $G^{\rm box,exact/relaxed}$ is defined as

$$\begin{aligned} &G^{\rm box,exact/relaxed}_{\mathbf{x_0};t_0}(\mathbf{r},t) \\ &\quad = (-)\sum_i \Bigg[\frac{1}{L^3}\sum_{\mathbf{x}}\sum_n^{N_{\rm low}} \frac{1}{\lambda_n} \chi^{(i)\dagger}_{\gamma_5,t_0[r]}(\mathbf{x},t) v^{(n)}(\mathbf{x},t) v^{(n)\dagger}(\mathbf{x}+\mathbf{r},t) \zeta^{(i)}_{\mathbf{p_z},-\mathbf{p_z},t_0[r]}(\mathbf{r}+\mathbf{x},t) \\ &\qquad + \chi^{(i)\dagger}_{\gamma_5,t_0[r]}(\mathbf{x_0},t) H^{-1}_{\rm high,exact/relaxed}(\mathbf{x_0},t|\mathbf{r}+\mathbf{x_0},t) \zeta^{(i)}_{\mathbf{p_z},-\mathbf{p_z},t_0[r]}(\mathbf{r}+\mathbf{x_0},t) \Bigg], \end{aligned} \tag{6.19}$$

where λ_n and $v^{(n)}$ are the n-th eigenvalue and eigenvector of H, $N_{\rm low}$ is the number of eigenmodes used, while $H^{-1}_{\rm high,exact/relaxed}$ is an inverse of H projected onto the high-mode subspace with a tight/relaxed stopping condition. Since χ and ζ are already solved with tight precision, we only relax a precision of the sink-to-sink propagator (green dotted line in Fig. 6.1). Furthermore, we averaged over all $\mathbf{x}$ in the low-mode part to maximize statistics. In comparison to the hybrid method, the insertion of the noise vectors decreases from 4 to 1, even though we give up the full spatial average of $\mathbf{x}$. A fewer spatial average is, however, not a severe problem in practice when we choose uncorrelated (= spatially distant) coordinates as many as possible for the averaging.

6.1.3 Triangle diagram

A triangle diagram shown in Fig. 6.1 is written as

$$G^{\rm tri}_{\mathbf{x};t_0}(\mathbf{r},t) = (-)\sum_{\mathbf{y}} {\rm tr}[D^{-1}(\mathbf{r}+\mathbf{x},t|\mathbf{y},t_0)\gamma_3 D^{-1}(\mathbf{y},t_0|\mathbf{x},t)\gamma_5 D^{-1}(\mathbf{x},t|\mathbf{r}+\mathbf{x},t)\gamma_5]. \tag{6.20}$$

Using the one-end trick at the source part, we obtain

$$G^{\rm tri}_{\mathbf{x};t_0}(\mathbf{r},t) = (-)\sum_i \chi^{(i)\dagger}_{\gamma_3,t_0[r]}(\mathbf{x},t) H^{-1}(\mathbf{x},t|\mathbf{r}+\mathbf{x},t)\xi^{(i)}_{\mathbf{0},t_0[r]}(\mathbf{r}+\mathbf{x},t). \tag{6.21}$$

As in the case of the box diagram, we employ the CAA for $\mathbf{x}$, which gives an improved triangle diagram as

$$G^{\mathrm{tri,imp}}_{\mathbf{x_0};t_0}(\mathbf{r},t) = G^{\mathrm{tri,exact}}_{\mathbf{x_0};t_0}(\mathbf{r},t) - G^{\mathrm{tri,relaxed}}_{\mathbf{x_0};t_0}(\mathbf{r},t) + \frac{1}{N_G}\sum_{\mathbf{x}'} G^{\mathrm{tri,relaxed}}_{\mathbf{x}';t_0}(\mathbf{r},t), \tag{6.22}$$

where

$$\begin{aligned} &G^{\mathrm{tri,exact/relaxed}}_{\mathbf{x_0};t_0}(\mathbf{r},t) \\ &= (-)\sum_i \Bigg[\frac{1}{L^3}\sum_{\mathbf{x}}\sum_n^{N_{\mathrm{low}}} \frac{1}{\lambda_n} \chi^{(i)\dagger}_{\gamma_5,t_0[r]}(\mathbf{x},t) v^{(n)}(\mathbf{x},t) v^{(n)\dagger}(\mathbf{x}+\mathbf{r},t) \xi^{(i)}_{\mathbf{0},t_0[r]}(\mathbf{r}+\mathbf{x},t) \\ &\qquad + \chi^{(i)\dagger}_{\gamma_5,t_0[r]}(\mathbf{x_0},t) H^{-1}_{\mathrm{high,exact/relaxed}}(\mathbf{x_0},t|\mathbf{r}+\mathbf{x_0},t) \xi^{(i)}_{\mathbf{0},t_0[r]}(\mathbf{r}+\mathbf{x_0},t) \Bigg]. \end{aligned} \tag{6.23}$$

The difference between the triangle and box diagram is only the combination of the one-end vectors. In comparison to the hybrid method, the insertion of the noise vectors decreases from 3 to 1.

6.1.4 Comparison to the result using the hybrid method

Before moving on to the details of the ρ resonance study, we briefly discuss the comparison between the hybrid method and the new scheme in terms of the $I = 1$ $\pi\pi$ interaction. Figure6.2 shows the effective LO potential of $I = 1$ $\pi\pi$ system at $t = 5$ with the $\pi\pi$ type source operator, obtained by the two different all-to-all treatments with the CP-PACS/JLQCD configurations introduced before. As seen in Fig. 6.2, the fluctuating behavior seen in the hybrid method is drastically suppressed by the new treatment. In this test calculation, about $\times 100$ statistical improvement is achieved on average. This improvement enables us to study the ρ resonance in details.

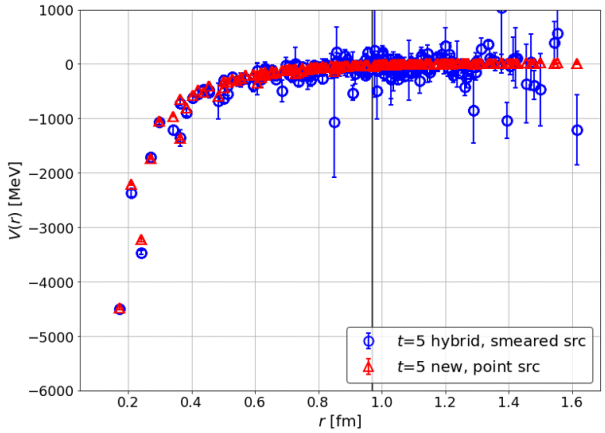

FIGURE 6.2: Comparison between the effective LO potentials at $m_\pi \approx 870$ MeV, obtained by the hybrid method (blue) and the new strategy (red)

6.2 Simulation details

We employ (2+1)-flavor full QCD configurations generated by the PACS-CS Collaborations [70] on a $32^3 \times 64$ lattice with the Iwasaki gauge action[55] and a non-perturbatively improved Wilson-clover action[54]. The paramters of the lattice actions and corresponding hadron masses are shown in Table 6.1. Since the ρ meson mass is above two-pion threshold, the ρ meson appears as a resonance [39]. The calculations are performed in the center-of-mass frame only, with the periodic boundary condition for all spacetime directions.

TABLE 6.1: Parameters of the gauge configuration in this study

β	κ_{ud}	κ_s	$c_{\rm SW}$	a [fm]	m_π[MeV]	m_ρ[MeV]
1.90	0.13754	0.13640	1.715	0.0907	411	892

Table 6.2 and 6.3 show general setups and parameters of the one-end trick and the CAA, respectively. We employ smeared quark operators $q_s(\mathbf{x},t) = \sum_{\mathbf{y}} f(\mathbf{x}-\mathbf{y})q(\mathbf{y},t)$ at the sink with the Coulomb gauge fixing, in order to improve signals of potentials at short distance. A smearing function f is given by

$$f(\mathbf{x}) = \begin{cases} Ae^{-B|\mathbf{x}|} & (\ 0 < |\mathbf{x}| < R\ ) \\ 1 & (\ |\mathbf{x}| = 0\ ) \\ 0 & (\ |\mathbf{x}| \geq R\ ), \end{cases} \tag{6.24}$$

with $A = 1.0,\ B = 1.0,\ R = 3.5$. As discussed in Appendix E, these parameters make potential smoother without worsening the convergence of the derivative expansion. For the one-end trick, we generate a single Z_4 noise vector for each insertion. To suppress the stochastic noises, we employ a dilution technique [29] in color, spinor, and space indices. We take space $s2$ dilution and $s4$ dilution [31] in the $\pi\pi$-type source and the ρ-type source, respectively. Color and spinor indices are fully diluted. As regards the CAA, we exactly calculate a low-mode part using 300 eigenmodes, and a high-mode part is estimated by an average over loosely solved solutions on 64 different spatial points $\mathbf{x} = (x_0 + 8l, y_0 + 8m, z_0 + 8n) \bmod 32$, with $l, n, m \in \{0, 1, 2, 3\}$. Tight and relaxed solutions are obtained with 1.0×10^{-24} and 9.0×10^{-6} for the squared residue, respectively. We randomly choose the reference point $\mathbf{x}_0 = (x_0, y_0, z_0)$ for each configuration to remove unnecessary systematics.

TABLE 6.2: Numerical setup for the calculation.

Source type	Scheme	$N_{\rm conf}$ (#. of time slice ave.)	Stat. error
$\pi\pi$-type	equal-time, smeared-sink	100 (64)	jackknife with bin–size 5
ρ-type	equal-time, smeared-sink	200 (64)	jackknife with bin–size 10

TABLE 6.3: Setups for the one-end trick and the CAA in this study. $N_{\rm eig}$ is the number of low eigenmodes. Color and spinor dilutions are always used.

Source type	One-end trick		CAA	
	Noise vector	Space dilution	$N_{\rm eig}$	# of averaged points
$\pi\pi$-type	Z_4 noise	$s2$ (even-odd)	300	64
ρ-type	Z_4 noise	$s4$	300	64

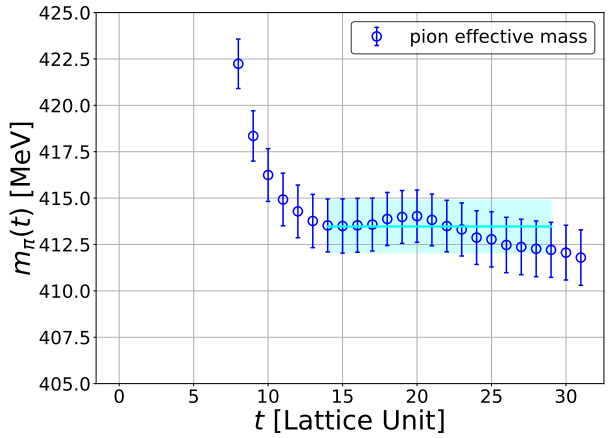

FIGURE 6.3: Effective mass of a pion (blue circles) and the fit result by a cosh function at $t = [t_{\rm min}, t_{\rm max}] = [14, 29]$ (cyan solid line with bands).

Figure 6.3 shows an effective mass of a pion obtained by an average of 200 configurations ($\times 64$ time slice average). A fit to the pion propagator at $t = [t_{\rm min}, t_{\rm max}] = [14, 29]$ with a cosh function gives $m_\pi = 413.5(1.4)$ MeV. We also check a $t_{\rm min}$ dependence of the effective mass, and the dependence is negligible compared with statistical errors as far as $t_{\rm min} \geq 13$. Therefore we confirm that a ground state saturation in $C(t)$ is achieved at $t = 13$. A possible leading inelastic contribution for two pions in this setup comes from a P-wave $K\overline{K}$ state with energy $W_{K\overline{K}} = 2\sqrt{m_K^2 + (2\pi/L)^2} \approx 1530$ MeV in non-interacting case, while the two-pion ground state energy is reported as $E_0 = 914(11)$ MeV in Ref. [39]. We therefore expect inelastic contributions in our correlation functions are suppressed at $t \approx 1/[W_{K\overline{K}} - E_0] \approx 3.5$. These considerations suggest that inelastic contributions in $R(\mathbf{r}, t)$ become negligible at $t \geq 13$, so that potentials can be reliably extracted at $t \geq 13$. Hereafter, we show results at $t = 14$ and 18 for ρ-type source and $\pi\pi$-type source, respectively.

As already discussed, the reduced rotational symmetry introduces higher partial wave contamination in lattice QCD simulations. This leads to systematic uncertainties in the HAL QCD potential appearing as multi-valued structures of potentials as a function of r. In this study, we address this issue by performing the approximated partial wave decomposition recently introduced to lattice QCD [62]. In practice, we remove the dominant $l = 3$ contamination when we evaluate the potential at $r = [2, 14.8]$. The remaining contamination in a short-range part, to which the partial wave decomposition cannot be reliably applied, is treated as the systematic uncertainty as will be discussed later.

The numerical simulation in this study is performed on the HOKUSAI Big-Waterfall in RIKEN and the Oakforest-PACS in Joint Center for Advanced HighPerformance Computing (JCAHPC).

6.3 Result

6.3.1 LO analysis

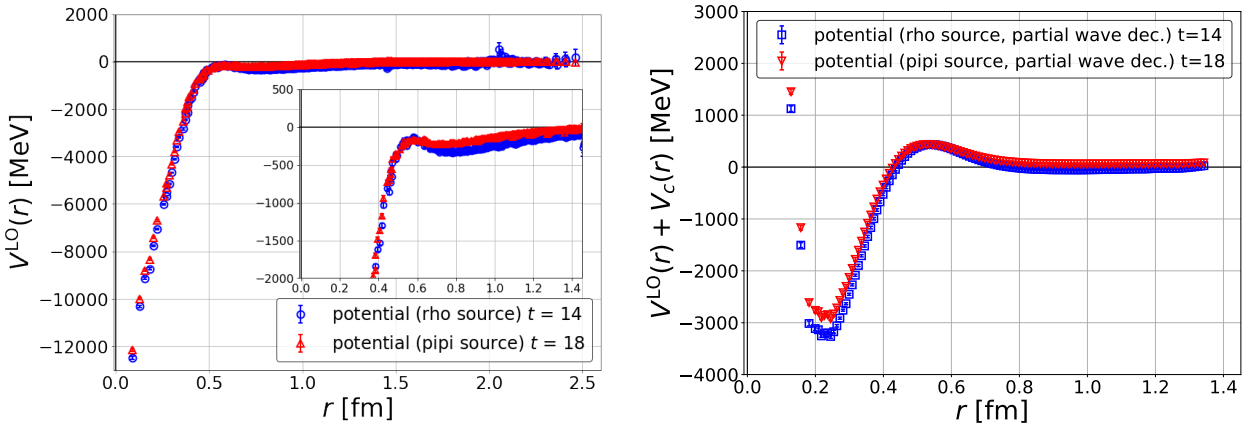

FIGURE 6.4: (Left) Effective LO potentials. Blue and red points show the results from the ρ-type source and the $\pi\pi$-type source, respectively. Inset shows an enlarged view of potentials. (Right) Improved potentials obtained by the partial wave decomposition with the P-wave centrifugal term, $V_c(r) = \frac{1}{2\mu}\frac{1\cdot 2}{r^2}$.

Figure 6.4 (Left) show the results for effective LO potentials without the partial wave decomposition. We observed that the potentials are attractive at all distances. Fig. 6.4 (Right) represents potentials with the P-wave centrifugal term after the partial wave decomposition, which become much smoother. The potentials with the centrifugal term have an attractive pocket at short distances and a potential barrier around $r = 0.5$ fm, which is characteristic for the existence of a resonance. We also notice that potentials depends on the choice of source operators. This observation suggests a presence of non-negligible higher-order contributions in the derivative expansion.

To calculate physical observables, we fit LO potentials with a sum of Gaussian terms given by

$$V(r) = a_0 e^{-(r-a_1)^2/a_2^2} + a_3 e^{-(r-a_4)^2/a_5^2} + a_6 e^{-(r-a_7)^2/a_8^2}. \tag{6.25}$$

For the fit, we utilize data obtained by the partial wave decomposition at $r = [2, 14.8]$ as already mentioned, combined with the original lattice data at $r \leq 2$. We also remove data at very short distances ($r = 0, 1$) since they suffer from large discretization errors. The remaining systematic uncertainties caused by non-smoothness at short distances are estimated by differences among three different fit results: a result using all allowed data (Fit), a result removing data at $r \leq 0.3$ fm which deviate more than 1σ upward from Fit (Fit$^-$), and a result removing data at $r \leq 0.3$

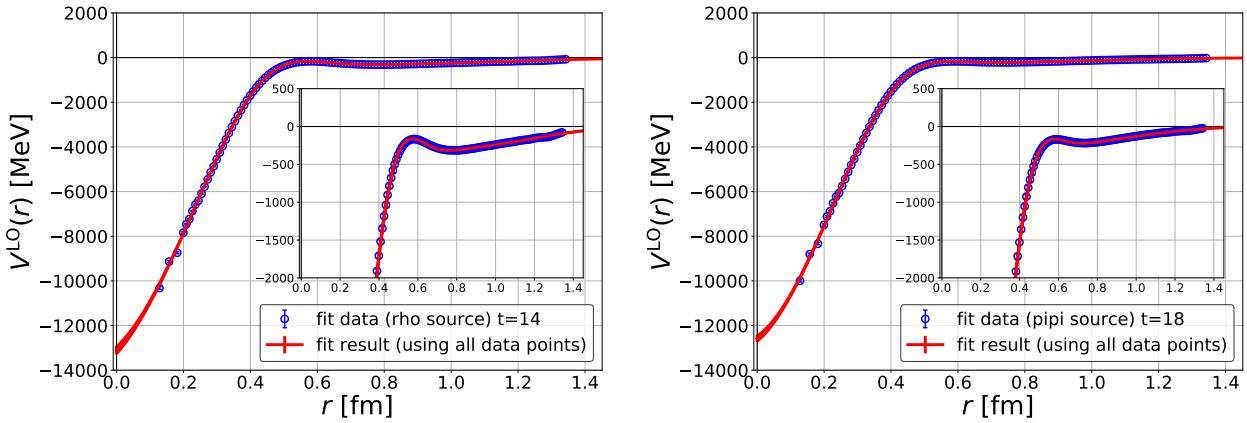

FIGURE 6.5: (Left) Fit result with the ρ-type source. Inset shows an enlarged view of them. (Right) The same plot with the $\pi\pi$-type source. Both results are obtained with all allowed data points.

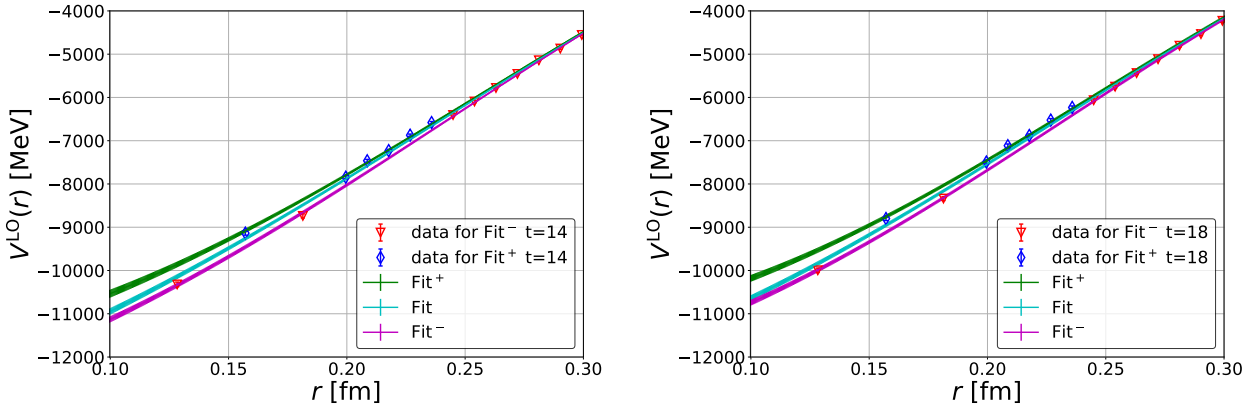

FIGURE 6.6: Systematic uncertainty in the fit of the potential at short distances. (Left) Three fit results with the ρ-type source. Red and blue points show data used in Fit$^-$ and Fit$^+$, respectively, and magenta and green lines are results of Fit$^-$ and Fit$^+$. We also show the fit result with all allowed data (Fit) by a cyan line for a comparison. (Right) The same plot with the $\pi\pi$-type source.

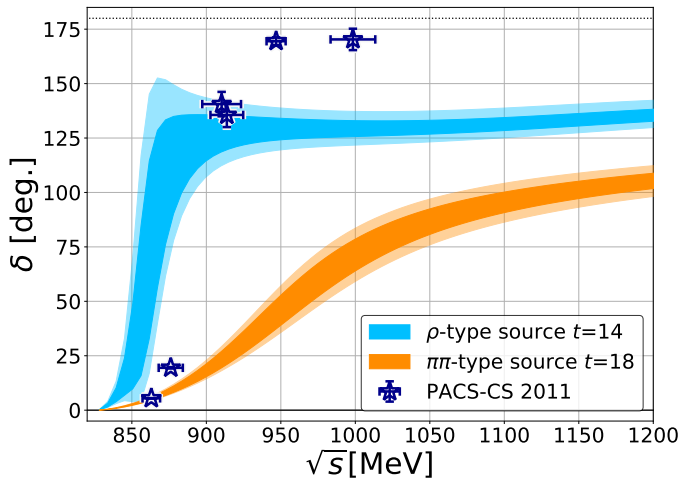

FIGURE 6.7: Phase shifts at the LO analysis. Blue (orange) band shows the ρ-type ($\pi\pi$-type) source result. Statistical errors are given by dark color bands, whereas systematic errors estimated by three different fits at short distances are represented by light color bands. The previous finite-volume results by the PACS-CS Collaboration [39] are also given by navy stars for comparison.

fm which deviate more than 1σ downward from Fit (Fit$^+$). The fit results using all allowed data (Fit) are shown in Figure 6.5, and three fit results are compared in Figure 6.6. We estimate systematic errors for physical observables by differences among fit results, taking the result using all allowed data as a central value.

Figure 6.7 shows scattering phase shifts obtained by the effective LO potentials, where systematic errors are shown by light color bands on top of statistical errors by dark color bands. Shown together is the previous result reported in Ref. [39], in which authors perform the Lüscher's finite-volume analysis using the same gauge configuration. The phase shift obtained with the ρ-type source crosses 90 degrees around $\sqrt{s} \approx 870$ MeV, while it only reaches around 130 degrees as the energy increases. On the other hand, the phase shift with the $\pi\pi$-type source crosses 90 degrees at much higher energy, around $\sqrt{s} \approx 1050$ MeV, with a much broader width. These behaviors are probably caused by truncation errors of the derivative expansion for the LO potential. Since the ρ-type source strongly overlaps the ρ resonance state, which corresponds to the ground state in our calculation, the resultant phase shift reproduces the resonance structure relatively well. On the other hand, the $\pi\pi$-type source mainly overlaps P-wave $\pi\pi$ scattering states far above the ρ resonance state in our setup, then it is difficult to capture the resonance structure correctly.

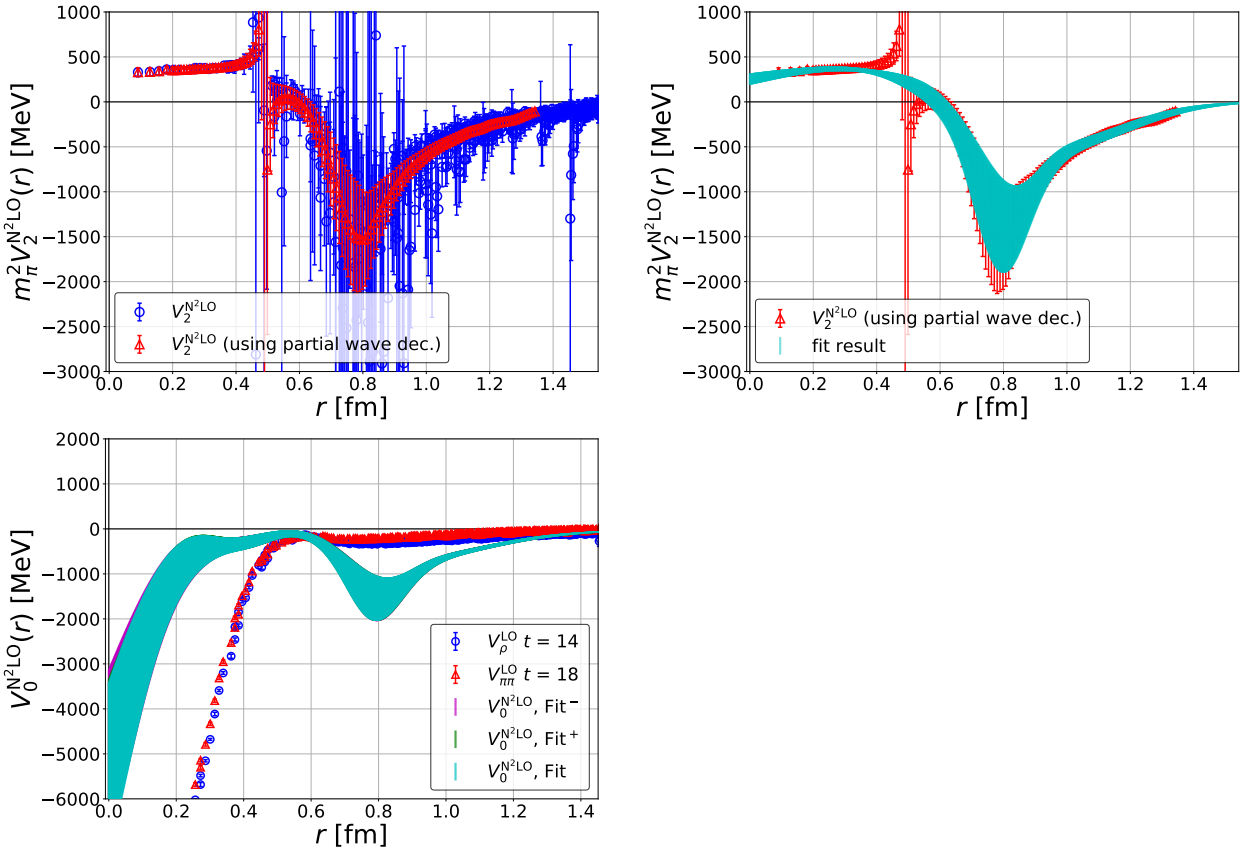

FIGURE 6.8: Effective N^{2}LO potentials. (Upper left) $V_2^{\mathrm{N^2LO}}$ determined from raw data (blue circles) and data obtained with the partial wave decomposition (red triangles). (Upper right) The fit result (cyan band) using the decomposed data (red triangles). (Lower) $V_0^{\mathrm{N^2LO}}$ obtained by three fit results , Fit(cyan), Fit$^-$(magenta) and Fit$^+$(green). Shown together are the effective LO potentials for a comparison.

6.3.2 N^{2}LO analysis

By solving Eq.(6.9), the effective N^{2}LO potentials are obtained as

$$V_2^{\mathrm{N^2LO}}(r) = \frac{V_\rho^{\mathrm{LO}}(r) - V_{\pi\pi}^{\mathrm{LO}}(r)}{\nabla^2 R_\rho(r)/R_\rho(r) - \nabla^2 R_{\pi\pi}(r)/R_{\pi\pi}(r)} \tag{6.26}$$

$$V_0^{\mathrm{N^2LO}}(r) = V_\rho^{\mathrm{LO}}(r) - V_2^{\mathrm{N^2LO}}(r)\nabla^2 R_\rho(r)/R_\rho(r). \tag{6.27}$$

In Fig. 6.8 (upper left), we show $V_2^{\mathrm{N^2LO}}$ obtained from raw data (blue points) and improved data by the partial wave decomposition (red points). The partial wave decomposition significantly reduces fluctuations of $V_2^{\mathrm{N^2LO}}$, as seen in the figure. A singular behavior around $r \approx 0.5$ fm is caused by a vanishing denominator of $V_2^{\mathrm{N^2LO}}$ in Eq.(6.26). In the fit of $V_2^{\mathrm{N^2LO}}$, we assume that the N^{4}LO and higher order terms in the derivative expansion can be neglected. This assumption leads us to employ a smooth fit function (same as the LO potentials) and utilize data points satisfying $1 - 2\mu V_2^{\mathrm{N^2LO}} > 0$. The fit result is shown by a cyan band in Fig. 6.8 (upper right). Since significant non-smooth behavior is not observed for $V_2^{\mathrm{N^2LO}}$ at short distances, systematic errors associated with removals of data mentioned before are not included in the analysis for $V_2^{\mathrm{N^2LO}}$. $V_0^{\mathrm{N^2LO}}(r)$ is then determined by the fit results of V_ρ, $\nabla^2 R_\rho/R_\rho$ and $V_2^{\mathrm{N^2LO}}$ through Eq. (6.27). We estimate systematic errors of $V_0^{\mathrm{N^2LO}}(r)$ at short distances through those of V_ρ^{LO} and $\nabla^2 R_\rho/R_\rho$. Figure 6.8 (lower) shows the resultant $V_0^{\mathrm{N^2LO}}$, together with effective LO potentials, V_ρ^{LO} and $V_{\pi\pi}^{\mathrm{LO}}$, for a comparison. As expected, there exists a large difference between $V_{\rho,\pi\pi}^{\mathrm{LO}}$ and $V_0^{\mathrm{N^2LO}}$ in Fig. 6.8 (lower).

To obtain the N^{2}LO phase shifts, we solve the radial Schrödinger equation with the N^{2}LO potential,

$$\left(\frac{d^2}{dr^2} - \frac{l(l+1)}{r^2} - \frac{2\mu V_0(r) - k^2}{1 - 2\mu V_2(r)}\right)\phi = 0. \tag{6.28}$$

The N^{2}LO phase shifts and $k^3 \cot\delta_1/\sqrt{s}$ are shown in Figure 6.9, together with the LO results and the previous finite-volume result. As seen in Fig. 6.9, except for the region $s < 0.75$ GeV^2 ($\sqrt{s} < 870$ MeV), the N^{2}LO phase shifts and $k^3 \cot\delta_1/\sqrt{s}$ become roughly consistent with the finite-volume results. The remaining deviation observed in the low-energy region can also be understood from the truncation error of the derivative expansion. In this study, the calculations are performed only in the center-of-mass frame, whose energy levels on the current lattice volume do not cover the low-energy region near the $\pi\pi$ threshold. Therefore, the N^{2}LO approximation in this study could suffer from the large truncation error of the derivative expansion in such a low-energy region. The detailed investigation is left for future studies.

In the last of this section, let us discuss the N^{2}LO interaction from a different point of view. At first sight, it is difficult to understand the relation between the effective N^{2}LO potential $V_0^{\mathrm{N^2LO}}$, $V_2^{\mathrm{N^2LO}}$ and the resultant phase shift. To make the situation more transparent, we convert our N^{2}LO potential $U^{\mathrm{N^2LO}} = V_0^{\mathrm{N^2LO}} + V_2^{\mathrm{N^2LO}}\nabla^2$ to an energy-dependent local form

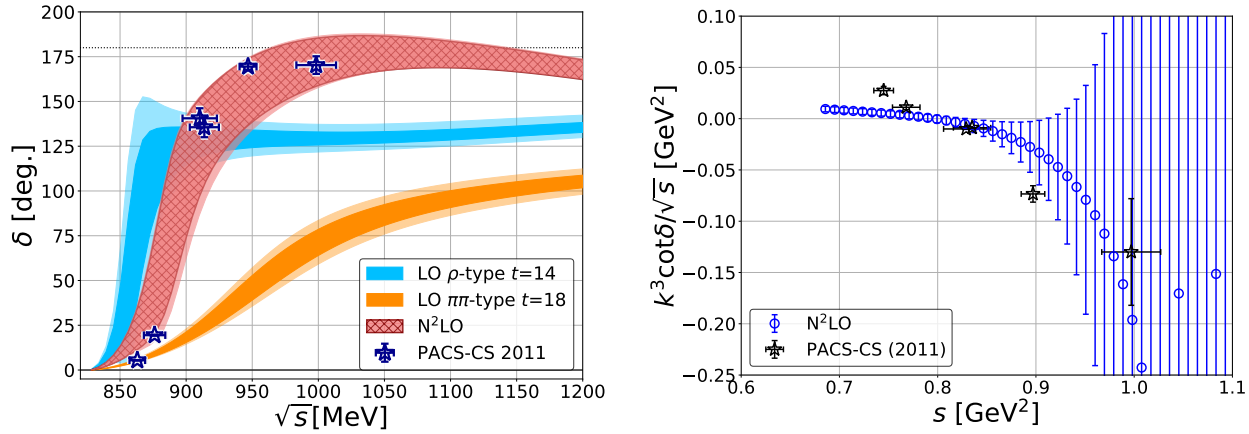

FIGURE 6.9: The N^{2}LO phase shifts (left) and $k^3 \cot\delta_1/\sqrt{s}$ (right), together with LO results (left figure) and previous finite-volume result by the PACS-CS Collaboration [39] (both figure) for comparisons. Large statistical errors at $s > 0.9$ GeV^2 in $k^3 \cot\delta_1/\sqrt{s}$ (right) are mainly caused by a divergent behavior of $\cot\delta$ at the phase shift around 180 degrees.

$V^{\mathrm{N^2LO}}(r;k)$ as [69]

$$V^{\mathrm{N^2LO}}(r;k) = \frac{V_0^{\mathrm{N^2LO}} - k^2 V_2^{\mathrm{N^2LO}}}{1 - m_\pi V_2^{\mathrm{N^2LO}}}. \tag{6.29}$$

Figure 6.10 shows this energy-dependent local potentials with the centrifugal term at several energies: near threshold ($\sqrt{s} = 830$ MeV), near the ground state energy in the center-of-mass frame ($\sqrt{s} = 910$ MeV), and at higher energy ($\sqrt{s} = 1050$ MeV). We also show V_ρ^{LO} for comparison. At low energy, the attractive pocket of $V^{\mathrm{N^2LO}}(r;k)$ is weaker than that of V_ρ^{LO}. It makes the N^{2}LO phase shifts smaller than the LO phase shift with ρ-type source. Around the CM ground state energy, $V^{\mathrm{N^2LO}}(r;k)$ and V_ρ^{LO} are almost identical since V_ρ^{LO} is almost saturated by the ground state. At high energy, a difference between $V^{\mathrm{N^2LO}}(r;k)$ and V_ρ^{LO} becomes large in all ranges. The significant improvement by the N^{2}LO analysis for the phase shifts at high energies can be understood from this difference.

6.3.3 Resonance parameters

We extract the resonance mass m_ρ and effective coupling between the ρ resonance and $\pi\pi$ scattering states, $g_{\rho\pi\pi}$, from the N^{2}LO potential. We employ two different procedures for the extraction, namely the Breit-Wigner fit and direct pole search of the S-matrix. In this section, we briefly discuss both procedures and compare our result to the previous finite-volume result.

Breit-Wigner fit

The Breit-Wigner fit is a conventional way to extract the resonance parameters from the narrow peak structure. We fit $k^3 \cot\delta_1(k)/\sqrt{s}$ by using the following parametrization,

$$\frac{k^3 \cot\delta_1(k)}{\sqrt{s}} = \frac{6\pi}{g_{\rho\pi\pi}^2}(m_\rho^2 - s), \tag{6.30}$$

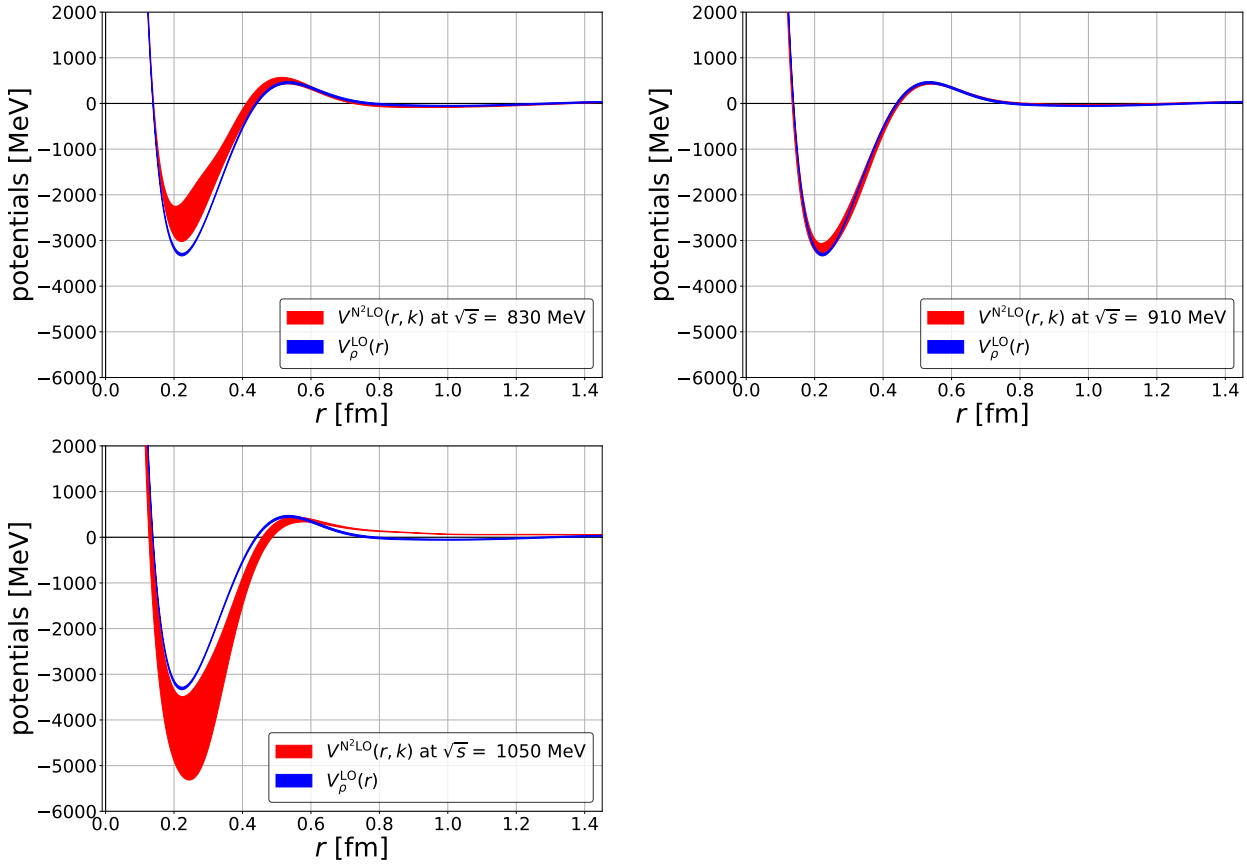

FIGURE 6.10: Energy-dependent local N^{2}LO potentials. (Upper left) near threshold ($\sqrt{s} = 830$ MeV). (Upper right) near the CM frame ground state energy ($\sqrt{s} = 910$ MeV). (Lower left) larger energy ($\sqrt{s} = 1050$ MeV). For a comparison, we show the effective LO potential with ρ-type source.

where m_ρ and $g_{\rho\pi\pi}$ are fit parameters corresponding to a resonance mass and a $\rho \to \pi\pi$ effective coupling, respectively. Our fit result is shown in Fig. 6.11 and it gives

$$m_\rho = 888(19)(^{+6}_{-2})\ \mathrm{MeV}, \tag{6.31}$$

$$g_{\rho\pi\pi} = 13.4(2.6)(^{+0.8}_{-0.0}), \tag{6.32}$$

where the first errors are statistical and the second ones are systematic errors associated with the short-range behavior of $V_0^{\mathrm{N^2LO}}$.

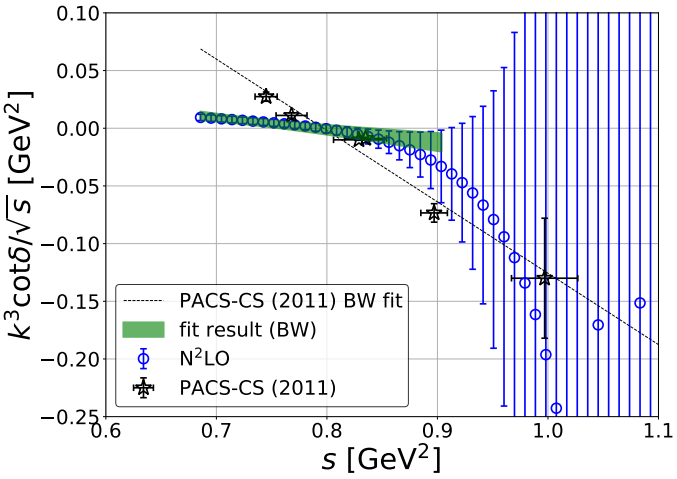

FIGURE 6.11: The Breit-Wigner fit for the N^{2}LO phase shifts $k^3 \cot \delta_1(k)/\sqrt{s}$ (blue points). The green band represents the fit with statistical errors and a range of the energy used in the fit. We also show data and Breit-Wigner fit of PACS-CS (2011) [39] by the black points and the dashed line, respectively, for a comparison.

Direct pole search

Theoretically, a resonance state is defined as a pole of the S-matrix on the second Riemann sheet, which provides us another method to extract resonance parameters in the HAL QCD method. To access the S-matrix in complex energy region, we solve the Schrödinger equation with arguments rotated by $r \to re^{i\theta}, k \to ke^{-i\theta}$[71–73], which reads

$$\left(\frac{d^2}{dr^2} - \frac{l(l+1)}{r^2} - \frac{2\mu e^{2i\theta} V_0(e^{i\theta} r) - k^2}{1 - 2\mu V_2(e^{i\theta} r)} \right) \phi = 0. \tag{6.33}$$

The regular solution ϕ to this equation behaves at long distances as

$$\phi \to \frac{i}{2} \left[\mathcal{J}_l(ke^{-i\theta}) \hat{h}_l^-(kr) - \mathcal{J}_l^*(ke^{-i\theta}) \hat{h}_l^+(kr) \right], \tag{6.34}$$

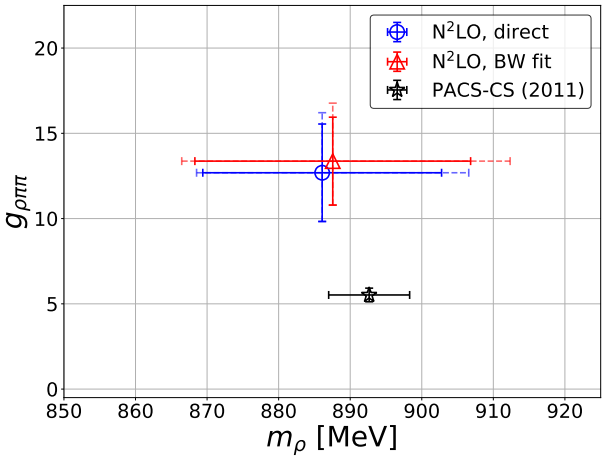

FIGURE 6.12: A comparison of N^{2}LO resonance parameters from the direct pole search (blue circle) and the Breit-Wigner fit (red triangle). Vertical and horizontal axes represent the coupling $g_{\rho\pi\pi}$ and the mass m_ρ, respectively. Statistical (systematic) errors are represented by solid (dashed) bars. Shown together is the result from PACS-CS (2011) [39] (black star). Errors for PACS-CS (2011) are statistical only.

where $\hat{h}_l^{\pm}(z) = \hat{n}_l(z) \pm i\hat{j}_l(z)$ are the Riccati-Hankel functions and $\mathcal{J}_l$ is the Jost function for the angular momentum l. The S-matrix on the complex $ke^{-i\theta}$ can therefore be obtained as

$$s_l(ke^{-i\theta}) = \frac{\mathcal{J}_l^*(ke^{-i\theta})}{\mathcal{J}_l(ke^{-i\theta})}, \tag{6.35}$$

from which we can search a pole position $k_{\rm pole} = |k_{\rm pole}|e^{-i\theta_{\rm pole}}$ by changing an input θ and k. The resonance mass and the decay width are extracted from the pole position $\sqrt{s}_{\rm pole}$ as

$$\sqrt{s}_{\rm pole} = 2\sqrt{k_{\rm pole}^2 + m_\pi^2} = m_\rho - i\Gamma_\rho/2, \tag{6.36}$$

where the decay width is related to the coupling constant $g_{\rho\pi\pi}$ as

$$g_{\rho\pi\pi} = \sqrt{\frac{6\pi\Gamma_\rho m_\rho^2}{k_\rho^3}}, \quad k_\rho := \sqrt{m_\rho^2/4 - m_\pi^2}. \tag{6.37}$$

The direct pole search gives

$$m_\rho = 886(17)(^{+4}_{-1})\ \text{MeV}, \tag{6.38}$$
$$\Gamma_\rho/2 = 22(8.6)(^{+4.5}_{-0.0})\ \text{MeV}, \tag{6.39}$$
$$g_{\rho\pi\pi} = 12.7(2.9)(^{+0.7}_{-0.0}), \tag{6.40}$$

where the first errors are statistical while the second ones are systematic errors.

Comparison to the previous result

Let us compare our N^{2}LO results with the previous result using the finite-volume method [39]. We summarize m_ρ and $g_{\rho\pi\pi}$ in Fig. 6.12. While m_ρ's are consistent with each other in all three cases, effective couplings in our study are about twice as large as the previous one. This discrepancy can be clearly seen as a difference in slopes of $k^3 \cot\delta_1/\sqrt{s}$ data at $s < 0.9$ GeV^2 in Fig. 6.11, which directly correspond to the coupling as $-6\pi/g^2_{\rho\pi\pi}$. In particular, a significant disagreement between the previous result and ours at $s \approx 0.75$ GeV^2 is the main source of the discrepancy for the slope. We note that the lowest energy level is obtained in the laboratory frame with $\mathbf{P} = (0, 0, 2\pi/L)$, which cannot be covered by the center-of-mass frame calculation.

This observation gives us an important lesson for the study of P-wave resonances by the HAL QCD method with the center-of-mass frame. If the non-locality of the potential happens to be large, the truncation errors could be large near the threshold. While a resonance mass is likely to be reproduced relatively well as long as the resonance appears in the energy region covered by the center-of-mass frame, the decay width (the effective coupling) may suffer from larger systematics since it is determined by the wide energy dependence around the resonance. To control this, we have some possible options:

1. Tuning lattice parameters such as a box size so as to cover a wide energy range even in the center-of-mass frame.

2. Determine the width by the support of the finite-volume method in the laboratory frame.

3. Perform the HAL QCD method with a combination of both the center-of-mass and laboratory frames.

The first option can be performed if the resonance mass is roughly guessed beforehand, but it is practically difficult for searches of unknown resonances. The second one is better than the first one, although it is only applicable to systems with good S/N ratios. The additional introduction of model dependence in coupled channel analysis is not preferable as well. The third one sounds to be the best, but it is highly nontrivial in practice since we have never performed the laboratory frame calculation in the HAL QCD method. Motivated by this result in part, we perform the first numerical study of the laboratory frame formalism. We discuss this topic in the next chapter.

Chapter 7

$I = 2$ $\pi\pi$ potential from the laboratory frame NBS wave function

From the ρ resonance study, we obtain an important lesson that the laboratory frame calculation may reduce the truncation error in the derivative expansion in certain cases. Furthermore, the study on the light scalar σ resonance in $I = 0$ $\pi\pi$ S-wave interaction requires the vacuum subtraction, which can also be achieved by introducing some non-zero total momenta. Although the formulation of the laboratory frame calculation has already been introduced[49], its numerical calculation has not been performed yet since the non-zero momentum projection of the hadron operators generally needs the all-to-all propagator. It is, however, now possible within a reasonable computational cost thanks to the new calculation scheme.

In this chapter, we discuss a numerical verification of the laboratory frame formulation. We study the elastic $I = 2$ $\pi\pi$ S-wave interaction as a first trial. Since the formulation contains involving numerical derivatives and their combinations, our prime interest is whether we can extract a precise HAL QCD potential from such a complicated calculation. Moreover, the energy eigenstates in the laboratory frame take different values from those in the center-of-mass frame, then we can see the systematics of the derivative expansion. We briefly mention a preliminary application to the $I = 1$ $\pi\pi$ interaction in the last part.

7.1 Calculation of correlation functions

The correlation functions are defined as

$$C_{\mathbf{p}}(X^4) = \sum_{\mathbf{x},\mathbf{y}} \langle \pi^+(\mathbf{x}, X_4) \overline{\pi}^+_{\rm smear}(\mathbf{p}, 0) \rangle, \tag{7.1}$$

$$F_{\pi^+\pi^+,\mathbf{P}}(\mathbf{x}, x^4, X^4) = \sum_{\mathbf{X}} e^{-i\mathbf{P}\cdot\mathbf{X}} \langle {\rm T} \pi^+(X + x/2) \pi^+(X - x/2) \overline{\mathcal{J}}_{\pi^+\pi^+}(\mathbf{P}, 0) \rangle, \tag{7.2}$$

where the pion operator $\pi^{\pm}$ is given as before. In this study, we take three different source operators as

$$\overline{\mathcal{J}}_{\pi^+\pi^+}(\mathbf{P}=(0,0,0),0) = \overline{\pi}^+_{\rm smear}(\mathbf{p_1}=\mathbf{0},0)\overline{\pi}^+_{\rm smear}(\mathbf{p_2}=\mathbf{0},0) \tag{7.3}$$

$$\overline{\mathcal{J}}_{\pi^+\pi^+}(\mathbf{P}=(0,0,1),0) = \overline{\pi}^+_{\rm smear}(\mathbf{p_1}=\mathbf{e_z},0)\overline{\pi}^+_{\rm smear}(\mathbf{p_2}=\mathbf{0},0) \tag{7.4}$$

$$\overline{\mathcal{J}}_{\pi^+\pi^+}(\mathbf{P}=(0,0,2),0) = \overline{\pi}^+_{\rm smear}(\mathbf{p_1}=\mathbf{e_z},0)\overline{\pi}^+_{\rm smear}(\mathbf{p_2}=\mathbf{e_z},0), \tag{7.5}$$

where we describe momenta in unit of $2\pi/L$ and $\overline{\pi}^+(\mathbf{p},0)$ is defined as

$$\overline{\pi}^+(\mathbf{p},0) = \sum_{\mathbf{y}} \pi^-(\mathbf{y},0)e^{+i\mathbf{p}\cdot\mathbf{y}}. \tag{7.6}$$

Those source operators overlap to the $I = 2$ $\pi\pi$ S-wave states with total momenta $\mathbf{P} = (0,0,n)$ $(n = 0,1,2)$, respectively. We employ the exponential smearing in all source operators. The correlation functions above can be estimated by using the one-end trick as discussed in Chap.5, except for the existence of relative time shifts and additional exponential factor $e^{-i\mathbf{P}\cdot\mathbf{X}}$ in the sink parts. Treatments of those additional features are almost trivial, therefore we do not discuss them in details here.

In this thesis, we basically refer to the results obtained by the R-correlators with the free lowest energy normalization:

$$R_{\mathbf{P}=\mathbf{0}}(\mathbf{x},x^4,X^4) = \frac{F_{\pi^+\pi^+,\mathbf{0}}(\mathbf{x},x^4,X^4)}{C_{\mathbf{0}}(X^4)^2} \tag{7.7}$$

$$R_{\mathbf{P}=\mathbf{e_z}}(\mathbf{x},x^4,X^4) = \frac{F_{\pi^+\pi^+,\mathbf{e_z}}(\mathbf{x},x^4,X^4)}{C_{\mathbf{0}}(X^4)C_{\mathbf{e_z}}(X^4)} \tag{7.8}$$

$$R_{\mathbf{P}=\mathbf{2e_z}}(\mathbf{x},x^4,X^4) = \frac{F_{\pi^+\pi^+,\mathbf{2e_z}}(\mathbf{x},x^4,X^4)}{C_{\mathbf{e_z}}(X^4)^2}. \tag{7.9}$$

The other normalization is studied to see the systematics, which is discussed in Appendix F. As a reminder, we summarize the formula necessary for the extraction of the effective LO potential again. We first estimate the following building blocks:

$$G(\mathbf{x},x^4,X^4) = \left((\partial_{X^4}-W_{0,\rm free})^2-\mathbf{P}^2\right)R_{\mathbf{P}}(\mathbf{x},x^4,X^4), \tag{7.10}$$

$$E(\mathbf{x},x^4,X^4) = \frac{1}{4m}\left[\partial^2_{X^4}-2W_{0,\rm free}\partial_{X^4}+W^2_{0,\rm free}-\mathbf{P}^2-4m^2\right]G(\mathbf{x},x^4,X^4), \tag{7.11}$$

$$L_{\perp}(\mathbf{x},x^4,X^4) = \nabla^2_{\perp}G(\mathbf{x},x^4,X^4), \tag{7.12}$$

$$L_{\parallel}(\mathbf{x},x^4,X^4) = \left(-(\partial_{X^4}-W_{0,\rm free})\nabla_{\parallel}+i\mathbf{P}\partial_{x^4}\right)^2 R(\mathbf{x},x^4,X^4), \tag{7.13}$$

TABLE 7.1: Numerical setup for the calculation. Momenta in the source operators are shown in unit of $2\pi/L$.

	Source	$N_{\rm conf}$ (#. of time slice ave.)	Stat. error
case 1	$\bar{\pi}(0,0,1)\bar{\pi}(0,0,0)$	399 (64)	jackknife with bin–size 21
case 2	$\bar{\pi}(0,0,1)\bar{\pi}(0,0,1)$	399 (64)	jackknife with bin–size 21
CM	$\bar{\pi}(0,0,0)\bar{\pi}(0,0,0)$	399 (16)	jackknife with bin–size 21

where the derivatives are numerically estimated by the central differences. By combining these, the effective LO potential in the time-dependent method is obtained by

$$V^{\rm LO}_{x^{*4}=0}(\mathbf{x}_\perp) = \left.\frac{\left(L_\perp + L_\parallel + mE\right)(\mathbf{x}, x^4, X^4)}{mG(\mathbf{x}, x^4, X^4)}\right|_{x^4=0,\mathbf{x}_\parallel=0}. \tag{7.14}$$

We use the standard time-dependent method in the case of $\mathbf{P} = \mathbf{0}$ instead of the complicated formulae above.

7.2 Numerical setup

We employ 2+1 flavor full QCD configurations generated by PACS-CS Collaborations [70] on a $32^3 \times 64$ lattice. The lattice actions and their parameters are basically same as the configuration used in the ρ resonance study, except for the hopping parameters $(\kappa_{ud}, \kappa_s) = (0.13700, 0.13640)$. This choice of the hopping parameters leads to the pion mass at $m_\pi \approx 700$ MeV. The pion mass is somewhat large, but it is convenient for our purpose since the computational cost of matrix inversions becomes cheap. The periodic boundary condition is employed in all spacetime directions as before. The general setups are given in Table 7.1. Correlation functions with non-zero total momenta (zero total momentum) are evaluated by 399 $\times$ 64 timeslices (399 $\times$ 16 timeslices) gauge configurations, and statistical errors are estimated by the jack-knife method with bin-size 21. The parameters of the exponential smearing are taken as $A = 1.2$, $B = 0.30$. As regards the one-end trick, we generate a single Z_4 noise vector for each insertion. We employ the dilution technique [29] in color, spinor, and spatial indices. Color and spinor indices are fully diluted, and $s2$ (even-odd) dilution [31] is taken for the spatial index. The numerical simulation is performed on Oakforest-PACS in Joint Center for Advanced HighPerformance Computing (JCAHPC).

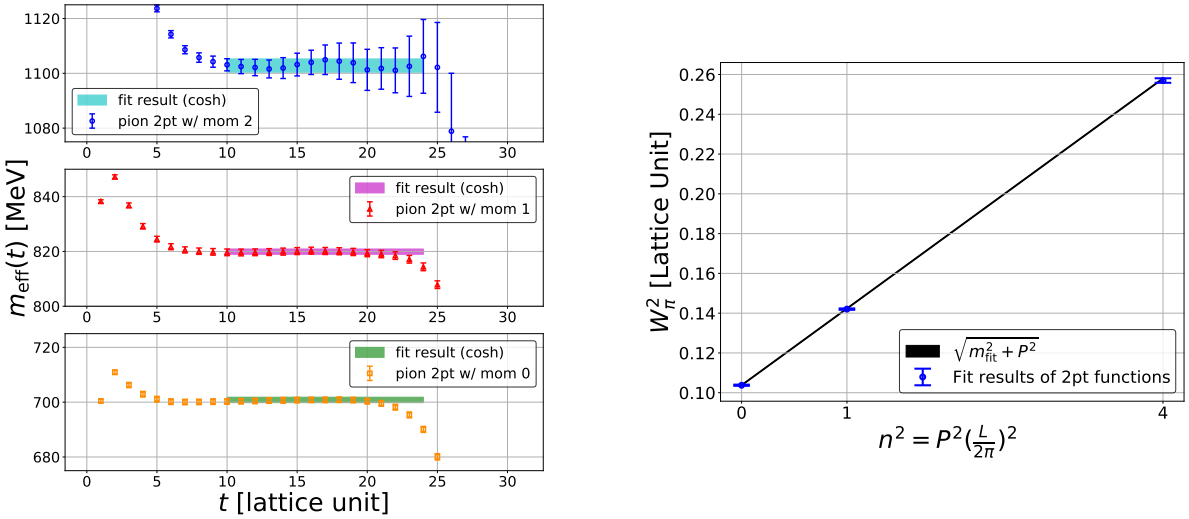

FIGURE 7.1: (Left) Effective energies of pion with $|p| = 0$ (orange square), $|p| = 2\pi/L$ (red triangle) and $|p| = 4\pi/L$ (blue circle). Fit results using a cosh shape and corresponding fit ranges are shown as bands. (Right) Comparison between extracted energies and continuum dispersion relation, $E(p) = \sqrt{m_{\pi,\mathrm{fit}}^2 + p^2}$. For $m_{\pi,\mathrm{fit}}$, we use the fit result of 2pt correlation function with $|p| = 0$ (green band in the bottom of the left figure).

7.3 Result

7.3.1 Dispersion relation

Since our formulation relies on the continuum dispersion relation, we first check a behavior of a pion dispersion relation. Figure 7.1 shows effective energies of a single pion with momenta $\mathbf{p} = (0, 0, n)$ $(n = 0, 1, 2)$ and comparison to the continuum dispersion relation $E(p) = \sqrt{m_\pi^2 + \mathbf{p}^2}$. We use the fit result of a pion propagator with $|p| = 0$ for m_π in the continuum dispersion relation. We obtain good plateaus thanks to the quark smearing, and as you can see in Fig. 7.1 (Right), energy levels with non-zero momenta do not deviate from the continuum dispersion relation up to $|p| = 4\pi/L$. Therefore we confirm that we can reliably utilize the continuum dispersion relation in this study.

7.3.2 NBS wave function in the laboratory frame

Let us first consider the spatial dependence of the $F_{\pi^+\pi^+,\mathbf{P}}(\mathbf{x}, x^4, X^4)$. Figure 7.2 (Left) shows the effective energies obtained by the X^4 dependence of $\sum_{\mathbf{x}} F_{\pi^+\pi^+,\mathbf{P}}(\mathbf{x}, x^4 = 0, X^4)$, together with corresponding non-interacting energy levels as horizontal lines. We observe that all effective energies reach a plateau at around $X^4 = 10$, and they are slightly larger than the non-interacting energies. It indicates that $F_{\pi^+\pi^+,\mathbf{P}}(\mathbf{x}, x^4, X^4)$ in our study is almost dominated by the ground states after $X^4 = 10$ and the interaction is repulsive. In Fig.7.2 (Right), we show $\mathbf{x}_\perp$ dependence of $F_{\pi^+\pi^+,\mathbf{P}}(\mathbf{x}_\perp, \mathbf{x}_\parallel = 0, x^4 = 0, X^4)$ at $X^4 = 16$. The smaller number of data in the laboratory frame is due to the fixed $\mathbf{x}_\parallel = 0$, which is mandatory to fix the scheme of the

NBS wave function. As expected from the effective energies, they show typical behaviors for the repulsive force, namely a monotonic increase. Furthermore, we observe that the NBS wave function in case 2 is similar to the center-of-mass wave function. This behavior is understandable since the lowest energy of case 2 is almost the same as the center-of-mass ground state, as seen in Fig.7.2 (left).

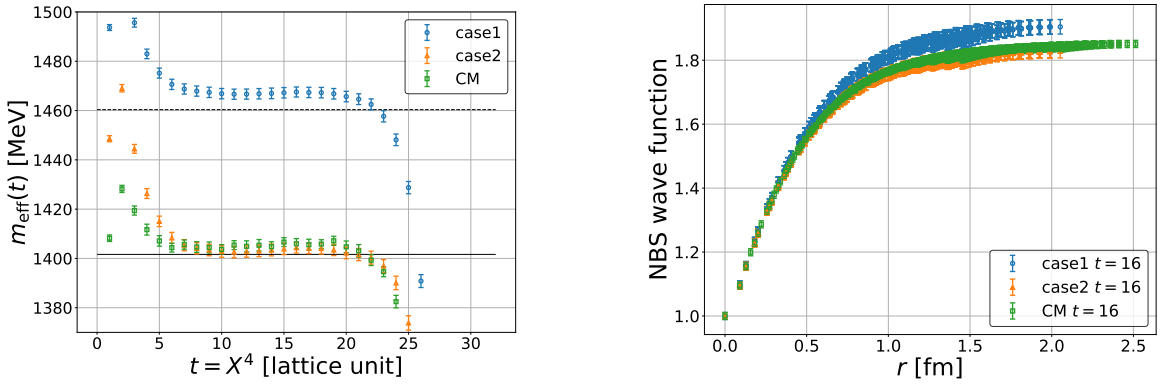

FIGURE 7.2: (Left) Effective energies obtained by spatial summation of $F_{\pi^+\pi^+,\mathbf{P}}$. Laboratory frame energies are boosted back to the CM frame via $W_{\mathrm{CM}}^2 = W_{\mathrm{L}}^2 - P^2$ for comparison. Dashed and solid lines show the lowest non-interacting energies with $\mathbf{P} = (0, 0, 2\pi/L)$ and $(0, 0, 4\pi/L)$, respectively. (Right) spatial dependence of $F_{\pi^+\pi^+,\mathbf{P}}$. For $|P| \neq 0$, we fix $\mathbf{x}_{\parallel} = \mathbf{0}$ and only show $\mathbf{x}_{\perp}$ dependence. Values at the origin are normalized to unity.

7.3.3 Effective LO potentials

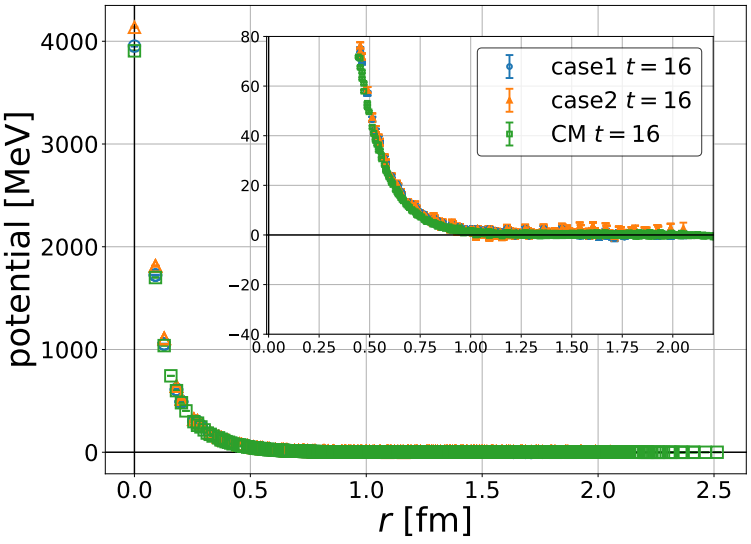

FIGURE 7.3: Comparison of all effective LO potentials. Inset shows an enlarged view of the potentials.

Figure7.3 shows the effective LO potential obtained by the time-dependent method at $X^4 = 16$. The potential show repulsive behaviors as expected, and three results with different momenta

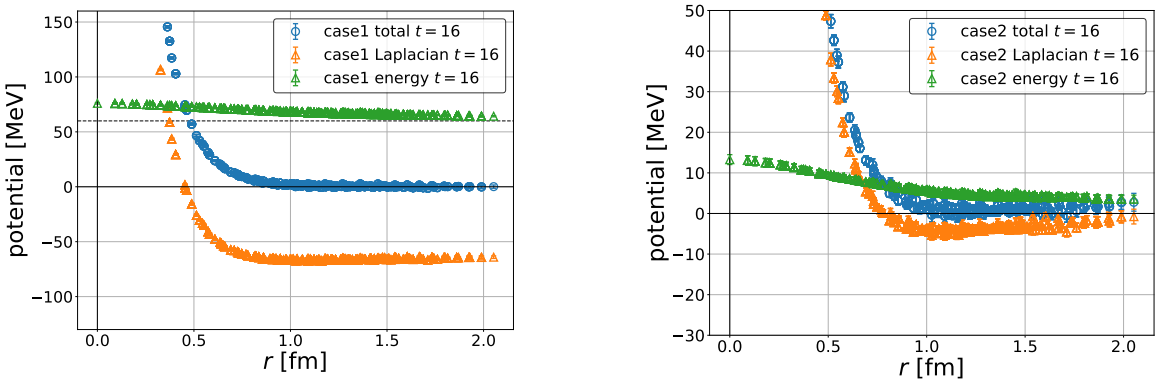

FIGURE 7.4: Decomposition of the effective LO potential in case 1 (Left) and case 2 (Right). A dotted line represents an expected relative energy in non-interacting case.

are almost consistent except for a short distance. We observe that the laboratory frame calculations have larger statistical errors and non-smooth behaviors than the center-of-mass case. Typically, the non-zero momentum calculation of the correlation function is noisier than the zero-mom calculation since the statistical improvement by the translational invariance is reduced. Indeed, the NBS wave functions in the laboratory frame themselves are noisier than the center-of-mass one (see Fig.7.2 (right)), even though the statistics is four times more. Moreover, there can be another noise source in the laboratory frame, namely high-order (4th) X^4 derivative terms in the time-dependent method. To estimate values of 4th-order X^4 derivatives with a fixed X^4 using the numerical difference, we need the information of $X^4 \pm 1, 2$. The correlation function generally becomes noisy at a large X^4, therefore the higher-order X^4 derivatives include noisier data. The non-smooth behaviors can be understood by the partial wave contents of the irreducible representation of the cubic group. In the laboratory frame calculation, the cubic rotation is no longer the symmetry of the system, since the box shape changes by the Lorentz contraction. In our calculation, the box shape becomes rectangular with size $L \times L \times \gamma L$ (γ is a boost factor) in the center-of-mass frame, then the rotational symmetry reduces to a subgroup of the cubic symmetry which keeps the rectangle invariant. The irreducible representation A_1^+ of the reduced symmetry contains contributions from $l = 0, 2, ...$, and therefore our calculation is suffered from $l = 2$ waves in contrast to the center-of-mass frame, where leading contamination comes from $l = 4$ waves. The difference observed in the short distance may be understood in terms of a discretization error. Since the laboratory frame calculation has a lot of numerical derivatives, there is more accumulated discretization error than the center-of-mass calculation. The discretization error mainly appears as the short-distance part around the origin, then the difference is significant there.

Next, to see how the time-dependent method works in details, we decompose the potentials into the Laplacian part ($\frac{\left(L_\perp + L_\parallel\right)}{mG}$) and the energy part ($\frac{mE}{mG}$) and see each components individually. Figure7.4 shows total and each components in the same plots. As seen, each component has a non-zero deviation from zero at large distances, but those shifts cancel with each other in total. Since the shift values are consistent with expectations from the non-interacting energy

levels, the cancellation is strong evidence of the validity of the time-dependent method.

Although we need larger statistics than the conventional center-of-mass calculation, we confirm that the precise potential can be extracted from the laboratory frame NBS wave function.

7.3.4 Scattering phase shifts

Finally, let us consider the behavior of physical observables, the scattering phase shifts $\delta_0(k)$ and $k \cot \delta_0(k)$. To calculate the phase shifts, we fit the effective LO potentials by a 4-Gaussian shape,

$$V(r) = a_0 e^{-(r/a_1)^2} + a_2 e^{-(r/a_3)^2} + a_4 e^{-(r/a_5)^2} + a_6 e^{-(r/a_7)^2}. \tag{7.15}$$

Fit results are shown in Fig. 7.5. Details of the estimation of systematic uncertainty are given in

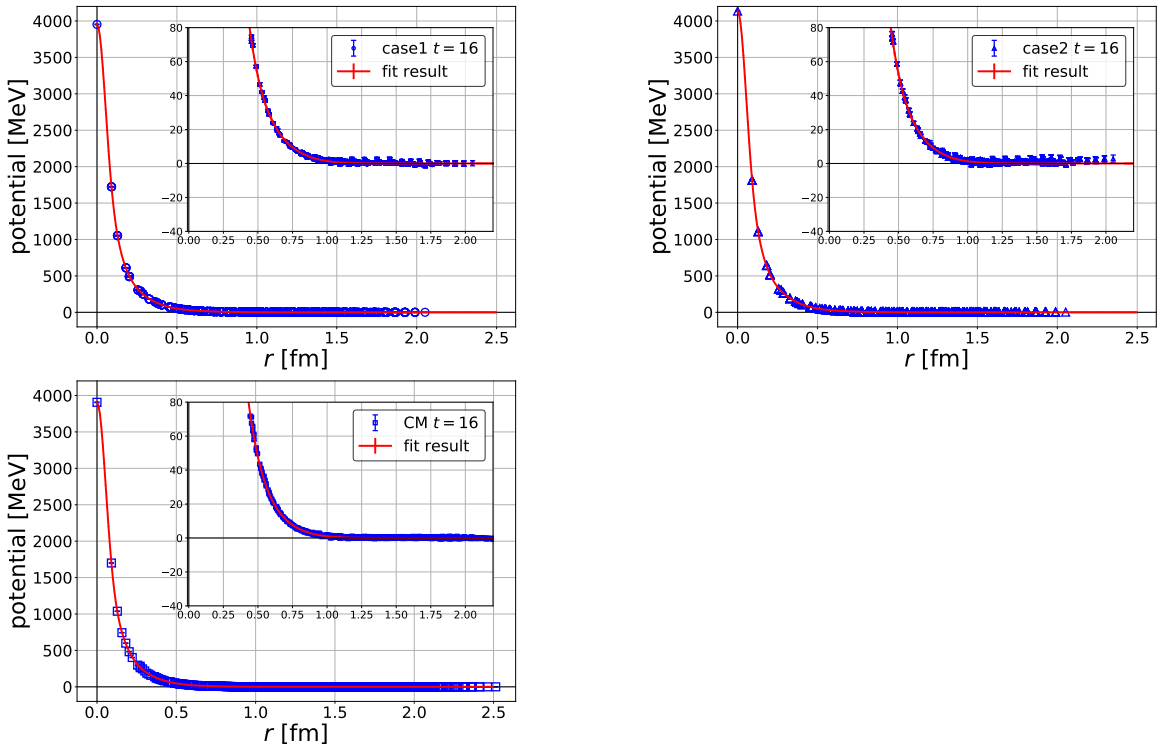

FIGURE 7.5: Fit results of the potentials. Original data (blue points) and corresponding fit results (red lines) are shown.

Appendix F. The resultant scattering phase shifts are summarized in Figure 7.7 (Left). As you can see, the phase shifts obtained by the laboratory frame calculations (blue and orange bands) give consistent phase shifts with the center-of-mass calculation (red band), as expected from the agreement of the LO potentials.

We also compare our result to values obtained by the Lüscher's method. The energy shifts needed for the analysis are extracted by single exponential fits of the time dependence of the R-correlators. Figure 7.6 shows effective energy shifts and corresponding fit results. Once we obtain the energy shifts, $k_n \cot \delta_0(k_n)$ is obtained by the Lüscher's formula as discussed in

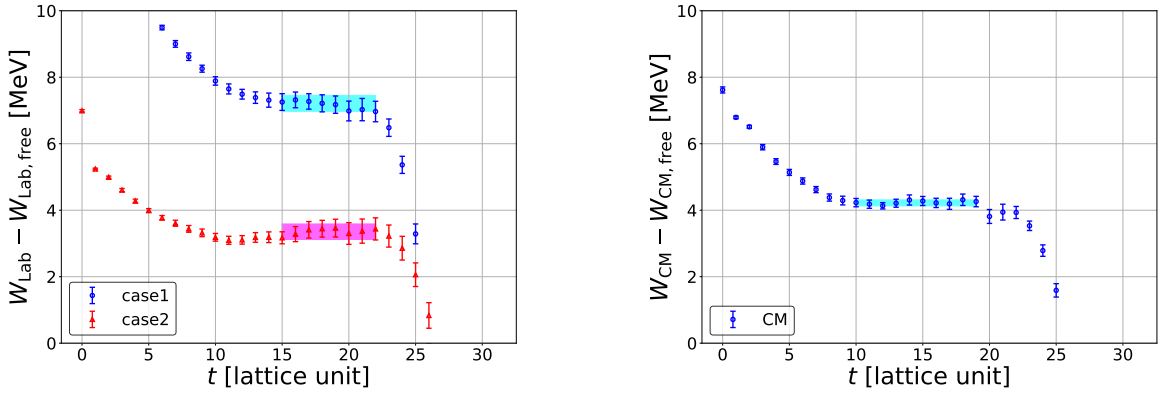

FIGURE 7.6: Extraction of the energy shifts by the exponential fits in the laboratory frame (left) and the center-of-mass frame (right). Color bands show fit range and fit result with statistical error.

Chap.3,

$$k_n \cot \delta_0(k_n) = 4\pi \frac{1}{\gamma_n L^3} \sum_{\mathbf{p} \in \mathcal{P}_\mathbf{d}} \frac{1}{\mathbf{p}^2 - k_n^2}, \tag{7.16}$$

where k_n is a relative momentum in the center-of-mass frame. All values of $k \cot \delta_0(k)$ are summarized in Fig. 7.7 (Right), together with a value in the literature [74]. As seen, we confirm that the phase shifts obtained by the HAL QCD method are consistent with those by the finite-volume method. It indicates that the LO approximation is valid in the energy region we consider here. This result also supports the validity of our calculation.

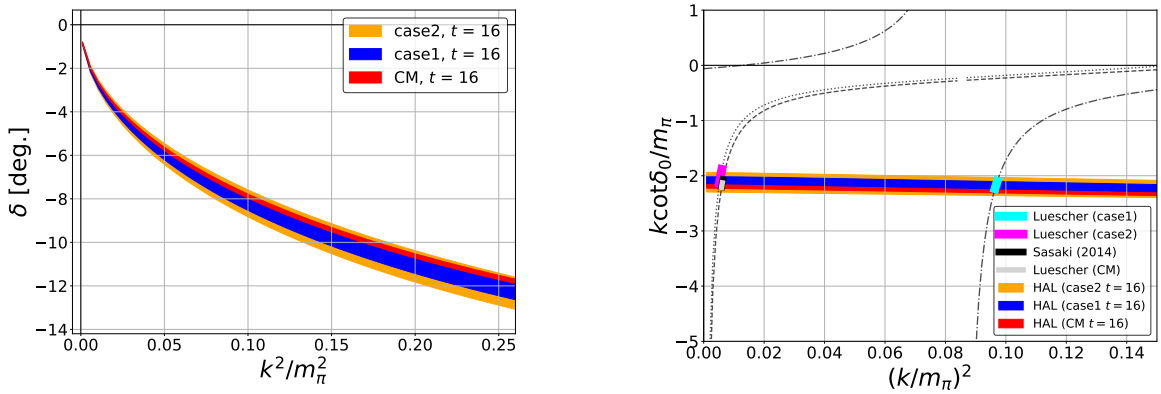

FIGURE 7.7: (Left) Scattering phase shifts obtained by the potentials. Color bands include both statistical and systematic error. (Right) $k \cot \delta_0(k)$ together with discrete points from the Lüscher's method. Dotted lines show k^2 dependence of the Lüscher's formula (7.16).

7.4 Preliminary application to the $I = 1$ $\pi\pi$ interaction

In the last part of this chapter, we briefly discuss a preliminary result on the $I = 1$ $\pi\pi$ interaction using the laboratory frame formalism. As mentioned before, we expect that this application gives a deeper understanding of the systematics observed in the ρ resonance study.

In this calculation, we employ gauge configurations at $m_\pi \approx 410$ MeV, same as the ρ resonance study. We employ the ρ-type source with a total momentum $\mathbf{P} = (0, 0, 2\pi/L)$ as

$$\overline{\mathcal{J}}^{A_2^-}_{\rho, I=1, I_z=0}(t_0) = \overline{\rho}^0_{\mathbf{p},3}(t_0), \tag{7.17}$$

$$\overline{\mathcal{J}}^{E^-}_{\rho, I=1, I_z=0}(t_0) = \overline{\rho}^0_{\mathbf{p},1}(t_0), \tag{7.18}$$

where $\overline{\rho}^0_{\mathbf{p},i}$ is defined as

$$\overline{\rho}^0_{\mathbf{p},i}(t) = \sum_{\mathbf{z}} e^{i\mathbf{p}\cdot\mathbf{z}} \frac{1}{\sqrt{2}} \left(\bar{u}(\mathbf{z}, t)\gamma_i u(\mathbf{z}, t) - \bar{d}(\mathbf{z}, t)\gamma_i d(\mathbf{z}, t) \right). \tag{7.19}$$

Those operators belongs to the irreducible representations A_2^- and E^-, whose lowest energies are reported as 863 MeV and 911 MeV in this setup, respectively [39]. The lowest energy state of A_2^- is interesting in particular, since this is what we want, the missing near-threshold state. Furthermore, the lowest energy of E^- is almost identical to the center-of-mass lowest energy and we can perform a consistency check by those results. Here we do not discuss a calculation of the correlation function in detail since it is almost the same as the center-of-mass case except for the relative time shift and insertions of exponential factors.

At present, we obtain a LO potential similar to V_ρ^{LO} using the source operator (7.18) as seen in Fig. 7.8 (Compare Fig. 6.4 (Left) in Chap. 6), although the statistical error is too large to compare them quantitatively. We may positively say that the laboratory frame formalism can also be applied to more involved systems, in which the all-to-all treatment is mandatory. On the other hand, we fail to extract the potential by using a source operator belonging to A_2^- representation (7.17). A possible reason is that the relative wave function is proportional to $\mathbf{x}_\parallel$ via the spherical harmonics of Y_{10} and the restriction of $\mathbf{x}_\parallel = 0$ in our formalism set the wave function zero automatically. To avoid this, we have to give up the time-dependent method and fix $\mathbf{x}_\parallel \neq 0$. In that case, however, the scheme of the potential cannot be the same as the center-of-mass frame. Therefore the combination to the center-of-mass calculation needs some assumption to the weak scheme dependence of the potential, but this is a highly nontrivial statement. Further studies are required.

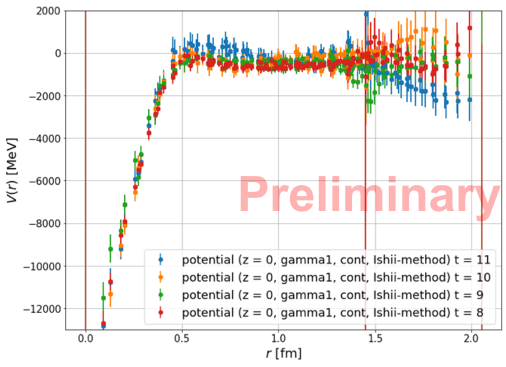

FIGURE 7.8: $I = 1$ $\pi\pi$ interaction from the laboratory frame.

Chapter 8

Summary and perspective

In this thesis, we introduce our works using the combination of the all-to-all propagator and the HAL QCD method and its application to the ρ resonance. This chapter is devoted to the summary and perspective of our study. We first summarize the results shown in this thesis section by section, then we present the prospects of our study, together with some latest preliminary calculations.

8.1 Application of the hybrid method

The first series of our study focuses on applications of the hybrid method, one of the methods to estimate the all-to-all propagator. This method is expected to be more suitable for the HAL QCD method than the LapH method. In those studies, we perform simulations on the $16^3 \times 32$ lattice with the pion mass of $m_\pi \approx 0.89$ GeV, and study $\pi\pi$ interactions with the isospin $I = 1, 2$. The study of $I = 2$ $\pi\pi$ interaction reveals that the potential with practical precision can be obtained by the hybrid method as long as the additional noise contamination is sufficiently removed. An important benefit by the all-to-all propagator, namely the early-time suppression of the inelastic contamination using the optimized source operator, is actually observed. We also obtain an important guiding principle for the parameter choice of the hybrid method. We then calculate the $I = 1$ $\pi\pi$ P-wave interaction with the same parameter choice as the $I = 2$ $\pi\pi$ interaction, but we find that the resultant potential is too noisy. Since the $I = 1$ $\pi\pi$ calculation newly allows quark creation/annihilation diagrams, we suspect that this structure enlarges the noise contamination of the hybrid method. We employ the time-separated sink operator and additionally introduce finer space dilution in the estimation of sink-to-sink propagator with an increased noise average to reduce this contamination. We find that the additional noise reduction gives a reasonable precision of the potential. The extracted interaction is strongly attractive and we obtain the physical bound state pole corresponding to the ρ meson.

In summary, we find that using the hybrid method only is not preferable in the HAL QCD method. One positive achievement is that the optimized source operator with quark smearing and momentum projection seems to lead to better time saturation behavior than the naive method. This observation is also related to a new direction of our research, application of all-to-all techniques to the baryon-baryon interaction as mentioned later. Another important aspect of those

studies is that they trigger the discussion on the new calculation scheme. Those studies identify the origin of the noisy behavior and indicate the right direction of improvements.

As a side note, there is still a possibility to use the hybrid as a part of the new calculation scheme. The guiding principle we obtained can be useful to optimize the parameters in such a case.

8.2 Study of the ρ resonance with the improved calculation scheme

Motivated by the success of the improved calculation scheme, we move on to the more realistic simulation of the ρ meson, which is the main result of this thesis. The ρ resonance is simple to calculate and is physically important, therefore it is ideal for the first step. We employ full QCD gauge configurations on the 32×64 lattice at the pion mass of $m_\pi \approx 0.41$ GeV and determine the HAL QCD potential at the N^{2}LO of the derivative expansion. As the previous result using the Lüscher's method with the same gauge configurations is available, we study the systematics of the derivative expansion by comparisons to it. In the LO analysis, the resultant LO potentials are attractive in all ranges and depend on the choice of the source operators. The phase shifts obtained by them deviate from the previous result, which indicates that the LO approximation is not enough for this system. We then investigate the effective N^{2}LO potential. Thanks to the improved scheme, we succeed in determining the effective N^{2}LO potential in the $I = 1$ $\pi\pi$ system for the first time. The N^{2}LO potential differs from the LO potentials largely, and the phase shift becomes roughly consistent with the previous result. We also extract the mass and coupling of the ρ resonance using the N^{2}LO potential. We find that the mass is consistent with the previous study, but the effective coupling deviates from it. We suspect that the main source of this deviation is a truncation error of the derivative expansion in a near-threshold region, which the center-of-mass energy levels cannot cover.

In conclusion, we can positively say that the typical structure of the ρ resonance is reproduced by the HAL QCD potential, thanks to the improved scheme on the all-to-all estimations. This fact opens a new frontier of the HAL QCD method, namely the resonance studies which require all-to-all propagators. On the other hand, it is newly revealed that potentials of P-wave (or higher partial wave) systems may suffer from the lack of the near-threshold information in the center-of-mass frame calculation when the non-locality of potentials is happened to be large. It indicates that we need to care about the convergence of the derivative expansion more in certain situations. Techniques to estimate all-to-all propagators developed in our study may also help to study the convergence of the expansion since they allow a wider choice of source operators.

8.3 Laboratory frame HAL QCD method

One of the possible remedies to reduce the truncation error of the derivative expansion in the near-threshold region is to introduce the laboratory frame calculation in the N^{2}LO (or higher) analysis. Moreover, to investigate the hadronic system which has the same quantum number as the vacuum, e.g. $I = 0$ $\pi\pi$ S-wave system, the laboratory frame calculation may play a crucial role to remove the vacuum contamination. The basic formulation of the extraction of the HAL QCD potential from the laboratory frame NBS wave functions is proposed before, but it has not been applied to actual simulations since it generally needs all-to-all propagators induced from spatial summations in the momentum projection. Under these circumstances, we study $I = 2$ $\pi\pi$ interaction by the laboratory frame formulation for the first time. The one-end trick enables us to construct source operators with some total momenta. We employ full QCD gauge configurations on the 32×64 lattice at the pion mass of $m_\pi \approx 0.70$ GeV and study the effective LO potentials of $I = 2$ $\pi\pi$ S-wave interaction with total momenta $\mathbf{P} = 2\pi/L(0, 0, n)$ $(n = 0, 1, 2)$. We find that the NBS wave functions in the laboratory frame behave similarly to the center-of-mass counterpart with somewhat larger statistical error. The extracted potential are consistent with each other except for short distances. We compare our new result to both the conventional center-of-mass HAL QCD result and results obtained by the Lüshcer's method, and we confirm consistency among them.

As a result, we confirm that the laboratory frame formulation of the HAL QCD method can be applied to practical simulations. It suggests a new possibility to calculate the interaction potential. This formalism may be applied to both the vacuum subtraction and the determination of the non-locality. Furthermore, the result implies that the $I = 2$ $\pi\pi$ interaction holds a small non-locality, which is consistent with the observation in the previous LapH application to the $I = 2$ $\pi\pi$ system at $m_\pi \approx 0.87$ GeV[26].

Possible issues appearing in this formalism are, for example, worse statistical errors than the center-of-mass calculations or sensitivity to the discretization error through the dispersion relation and the use of many derivatives. Furthermore, the condition to fix $\mathbf{x}_\parallel = 0$ in the time-dependent method may restrict the applicability of this formalism when we consider higher partial waves whose spherical harmonics depend on $\mathbf{x}_\parallel$, as also briefly mentioned later.

8.4 Perspective

Our new calculation scheme can be applied to not only resonant systems but also other hadronic scatterings, therefore we expect that there exist many applications in the future. We discuss possible applications expected in near future as the closing part of this thesis.

8.4.1 Resonance studies

Our prime motivation is to shed light on hadronic resonances discovered and predicted. Since we confirm that our calculation scheme can capture the typical ρ resonance up to systematics of the derivative expansion, we are now trying to investigate other resonant systems. One example is the scalar resonance in the light quark sector, so-called σ and κ resonance.

The σ resonance appears in $I = 0$ $\pi\pi$ S-wave channel and is known that it is very broad and light. This state is first predicted theoretically and its nature has been discussed for a very long time. Some lattice QCD calculations have also been performed [75–78] until now. The technical issue is that the $I = 0$ $\pi\pi$ S-wave channel needs the all-to-all propagator and has the same quantum number as the vacuum state, which introduces unwanted vacuum contamination in lattice QCD. The vacuum subtraction can be achieved by subtracting a time-independent term from the correlation function in some ways or by performing the laboratory frame calculations, where the vacuum cannot mix due to the vanishing total momentum. We are challenging to calculate the correlation function of this system since we can now treat both the all-to-all propagator and the laboratory frame. At this moment, we observed that the laboratory frame formalism seems to avoid the vacuum mixing, but we need more statistics to extract physical information.

The κ resonance is expected to appear as a broad resonance near the threshold of $I = 1/2$ $K\pi$ S-wave channel, but it is still "need confirmation" status in the Particle Data Group summary table [4]. It has also been discussed for a long time together with other scaler resonances like σ, and it is important to study this state in detail from lattice QCD. Its numerical simulation is relatively easy since it does not couple to the vacuum state. In our test calculation, however, the resultant NBS wave function has a node structure and the potential becomes singular at that point. This behavior may be attributed to the singular behavior of the NBS wave function due to the OPE as mentioned in Chap. 6 and Appendix E, but we have to investigate it carefully to find its origin and some possible remedies to avoid it. Both σ and κ are expected to belong to a scalar nonet of SU(3) flavor symmetry, therefore the numerical simulation on SU(3) limit can also bring valuable implications on them.

Applications to the charmed hadron interaction may also be important since many exotic resonances, e.g. the so-called X, Y, Z states, have been observed in experiments. To compare lattice QCD result to experiments, the large-scale simulation with physical hadron masses is mandatory. It may require more improvements of our all-to-all calculation scheme as well as improvements of computational codes.

The study on the meson-baryon interactions and baryon resonances, where the advantage of the HAL QCD method may appear more clearly, is now ongoing by a similar methodology.

The detailed study on the remaining systematics of the derivative expansion found in our ρ resonance study is another important task. As already discussed in Chap.7, we are now trying to extract the $I = 1$ $\pi\pi$ P-wave interaction using the laboratory frame. At this moment we obtain a LO potential similar to $V_\rho^{\rm LO}$ if we employ the source operator belongs to the E^- irreducible

representation of the tetragonal group. On the other hand, we fail to extract the potential from the A_2^- source operator, whose ground state is the near-threshold energy level we want. Further studies are required.

8.4.2 Other applications

The all-to-all propagator allows the smeared source operator with momentum projection. Therefore, the techniques in our study can bring some improvements in the determination of hadron interactions. Application to the baryon-baryon interactions is especially important to avoid an explosion of statistical errors due to the signal-to-noise ratio problem. Furthermore, the momentum projection allows us to study important interactions, e.g. the P-wave NN interaction. We can also study the systematics of the derivative expansion in more details by combining different source operators. Motivated by those issues, we are now working on the application of the one-end trick to baryon interactions. The one-end trick introduced in this thesis assumes applications to meson operators, but its extension to the baryon operator exists as well [79]. We apply this extension to the NN interaction and find that we can calculate the potential reasonably with some technical modification. At the same time, we find that the LO potential obtained by the smeared NN source operator is happened to be slightly different from the conventional one with the wall NN source, which may come from the non-locality of the potential. To study the origin of the difference, we study the $\Xi\Xi$ interaction, whose non-locality is discussed in detail before [69]. In this case, we obtain slightly different potential from that of the wall source as in the case of NN interaction, but the scattering length obtained by the potentials seems to be consistent with each other as seen in Fig.8.1 (right). By combining the previous result of the N^{2}LO study, the wall source seems to be somewhat better than the smeared source, but this conflicts with our intuition since the inelastic contamination in the smeared source is expected to be well-suppressed in general. At this moment we still do not understand the superiority of the wall source, but we expect that our understanding of the systematics of the HAL QCD potential as well as the nature of hadron interactions advances in the near future in collaboration with the supercomputer Fugaku.

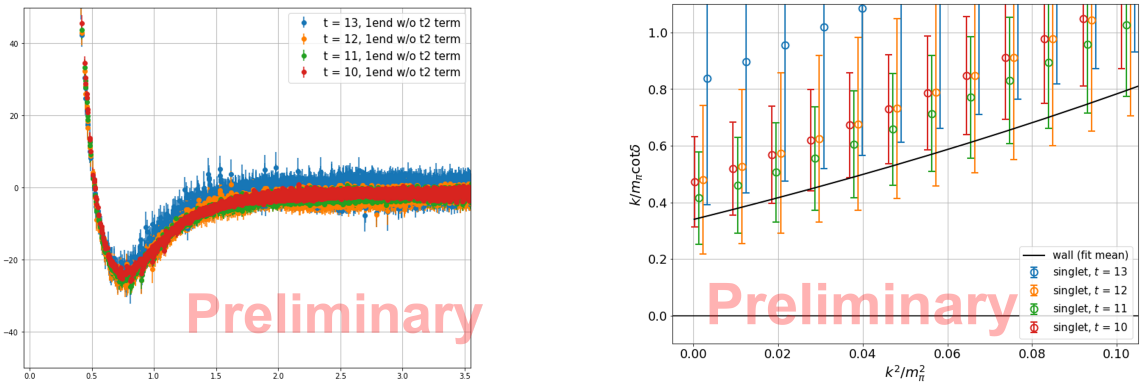

FIGURE 8.1: Preliminary results on ΞΞ interaction using the one-end trick. (Left) Effective LO potential of S-wave ΞΞ spin-singlet channel. (Right) $k \cot \delta$ in comparison to the wall source result. Black line shows mean values of $k \cot \delta$ obtained by the wall source.

Acknowledgements

First of all, I would like to thank to Prof. Sinya Aoki for his fruitful guidance and support. I am grateful to my research collaborators, Dr. Takumi Doi, Dr. Tatsumi Aoyama, Dr. Kenji Sasaki, Dr. Shinya Gongyo, Dr. Takaya Miyamoto and Mr. Kotaro Murakami, for stimulating discussions and advices. I also thank to all members of the HAL QCD Collaboration for fruitful discussions. I would like to thank Dr. Yusuke Namekawa for valuable discussion and comments on my research paper. I am very grateful to the member of Bridge++ code project, namely Dr. Issaku Kanamori and Dr. Hideo Matsufuru, for providing the improved version of Bridge++ solvers [80] and advices on its usage. I also wish to appreciate warm friendship and advices on my research life by past and present colleagues of Yukawa Institute for Theoretical Physics (YITP), Dr. Kazuma Shimizu, Dr. Takaya Miyamoto, Mr. Taigen Kawano and Mr. Takumi Bessyo. I would like to appreciate economical support and warm encouragement of my family, Yoshihiko Akahoshi, Chikako Akahoshi and Yukiko Maruno.

We thank the CP-PACS/JLQCD Collaboration[63, 64], PACS-CS Collaboration[70] and ILDG/JLDG[81] for providing their configurations. The numerical simulation in this study is performed on Cray XC40 previously in YITP, HOKUSAI Big-Waterfall in RIKEN and Oakforest-PACS in Joint Center for Advanced HighPerformance Computing (JCAHPC). The framework of our numerical code is based on Bridge++ code [65]. I am supported in part by the Japan Society for the Promotion of Science (JSPS).

The authors also thank YITP at Kyoto University. Discussions during the YITP workshop YITP-X-19-03 on "Non-perturbative methods in quantum field theories and applications to elementary particle physics", YITP-W-19-15 on "QUCS 2019" and YITP-T-19-01 on "Frontiers in Lattice QCD and related topics" were useful to complete this work.

Appendix A

Continuum limit of the naive lattice QCD action

In this appendix, we explicitly show that the lattice action (2.30) and (2.36) introduced in Chap. 2 reproduces the continuum action at the limit of $a \to 0$.

A.1 Fermion action

Let us consider the lattice fermion action (eq. (2.30) in Chap. 2),

$$S_F = a^4 \sum_{n\in\Lambda} \bar{\psi}^{(f)}(n) \left(\sum_{\mu=1}^{4} \gamma_\mu \frac{U_\mu(n)\psi^{(f)}(n+\hat{\mu}) - U_\mu^\dagger(n-\hat{\mu})\psi^{(f)}(n-\hat{\mu})}{2a} + m^{(f)}\psi^{(f)}(n) \right). \tag{A.1}$$

Since we consider the limit of $a \to 0$, we can utilize the exponential representation of the link variables and its expansion as

$$U_\mu(n) = e^{iaA_\mu(n)} = 1 + iaA_\mu(n) + \mathcal{O}(a^2) \tag{A.2}$$

$$U_\mu^\dagger(n-\hat{\mu}) = e^{-iaA_\mu(n-\hat{\mu})} = 1 - iaA_\mu(n) + \mathcal{O}(a^2). \tag{A.3}$$

Furthermore, the fermion fields are expanded as

$$\psi^{(f)}(n \pm \hat{\mu}) = \psi^{(f)}(n) \pm a\partial_\mu \psi^{(f)}(n) + \mathcal{O}(a^2). \tag{A.4}$$

By combining those equations, we can expand the difference operator of eq. (A.1) in terms of the lattice spacing a as

$$\begin{aligned} \frac{1}{2a}\{(1+iaA_\mu(n))(\psi^{(f)}(n)+a\partial_\mu\psi^{(f)}(n)) - (1-iaA_\mu(n))(\psi^{(f)}(n)-a\partial_\mu\psi^{(f)}(n)) + \mathcal{O}(a^2)\} \\ = \frac{1}{2a}\left(2aiA_\mu(n)\psi^{(f)}(n) + 2a\partial_\mu\psi^{(f)}(n) + \mathcal{O}(a^2)\right) \\ = (\partial_\mu + iA_\mu(n))\psi^{(f)}(n) + \mathcal{O}(a). \end{aligned} \tag{A.5}$$

Therefore, at the limit of $a \to 0$ we obtain

$$\begin{aligned} & a^4 \sum_{n\in\Lambda} \bar{\psi}^{(f)}(n) \left(\sum_{\mu=1}^{4} \gamma_\mu \frac{U_\mu(n)\psi^{(f)}(n+\hat{\mu}) - U_\mu^\dagger(n-\hat{\mu})\psi^{(f)}(n-\hat{\mu})}{2a} + m^{(f)}\psi^{(f)}(n) \right) \\ & \to \int d^4x \bar{\psi}^{(f)} (\sum_\mu \gamma_\mu(\partial_\mu + iA_\mu) + m^{(f)})\psi^{(f)}, \end{aligned} \tag{A.6}$$

where we replace the summation $a^4 \sum_{n\in\Lambda}$ to the integral $\int d^4x$ when we take the continuum limit. The final form is identical to the continuum fermion action.

A.2 Gauge action

Next, let us consider the Wilson gauge action (eq. (2.36) in Chap. 2),

$$S_G = \frac{2}{g^2} \sum_{n\in\Lambda} \sum_{\mu<\nu} \mathrm{Re}\ \mathrm{tr}(\mathbf{1} - U_{\mu\nu}(n)) \tag{A.7}$$

$$= \frac{1}{g^2} \sum_{n\in\Lambda} \sum_{\mu\neq\nu} \mathrm{tr}(\mathbf{1} - U_{\mu\nu}(n)), \tag{A.8}$$

where the second equality is obtained by utilizing $U_{\mu\nu} = U_{\nu\mu}^\dagger$. The second form is more useful to see the continuum limit. By using the Baker-Campbell-Hausdorff formula,

$$e^A e^B = e^{A+B+\frac{1}{2}[A,B]+\ldots}, \tag{A.9}$$

we can evaluate the plaquette in terms of the gauge field $A_\mu(x)$ as

$$\begin{aligned} U_{\mu\nu}(n) &= e^{iaA_\mu(n)} e^{iaA_\nu(n+\hat{\mu})} e^{-iaA_\mu(n+\hat{\nu})} e^{-iaA_\mu(n)} \\ &= \exp\left[iaA_\mu(n) + iaA_\nu(n+\hat{\mu}) - \frac{a^2}{2}[A_\mu(n), A_\nu(n+\hat{\mu})] + a^3 B_1 + a^4 C_1 + \ldots \right] \\ &\quad \times \exp\left[-iaA_\mu(n+\hat{\nu}) - iaA_\mu(n) - \frac{a^2}{2}[A_\mu(n+\hat{\nu}), A_\mu(n)] + a^3 B_2 + a^4 C_2 + \ldots \right] \\ &= \exp\Big[iaA_\mu(n) + iaA_\nu(n+\hat{\mu}) - iaA_\mu(n+\hat{\nu}) - iaA_\mu(n) \\ &\quad - \frac{a^2}{2}[A_\mu(n), A_\nu(n+\hat{\mu})] - \frac{a^2}{2}[A_\mu(n+\hat{\nu}), A_\mu(n)] \\ &\quad + [iaA_\mu(n) + iaA_\nu(n+\hat{\mu}), -iaA_\mu(n+\hat{\nu}) - iaA_\mu(n)] + a^3 B + a^4 C + \ldots \Big]. \end{aligned} \tag{A.10}$$

By inserting the expansion of gauge fields with shifts as

$$A_\mu(n+\hat{\nu}) = A_\mu(n) + a\partial_\nu A_\mu(n) + \mathcal{O}(a^2), \tag{A.11}$$

into the exponent of eq.(A.10), we obtain

$$\begin{aligned} U_{\mu\nu}(n) &= \exp\left[ia^2\partial_\mu A_\nu(n) - ia^2\partial_\nu A_\mu(n) - a^2[A_\mu(n), A_\nu(n)] + a^3 B'_{\mu\nu} + a^4 C'_{\mu\nu} + ...\right] \\ &= \exp\left[ia^2 F_{\mu\nu}(n) + a^3 B'_{\mu\nu} + a^4 C'_{\mu\nu} + ...\right]. \end{aligned} \tag{A.12}$$

Although we do not explicitly estimate the $\mathcal{O}(a^3)$ or higher order contributions $B'_{\mu\nu}, C'_{\mu\nu}$, they should have structures like $B'_{\mu\nu} = iB'^a_{\mu\nu}T^a, C'_{\mu\nu} = iC'^a_{\mu\nu}T^a$ since the plaquette $U_{\mu\nu}(n)$ belongs to SU(3). In the discussion of the continuum limit, details of the coefficients $B'^a_{\mu\nu}, C'^a_{\mu\nu}$ is not important, therefore we do not discuss any more. By inserting eq.(A.12) into the Wilson gauge action, we obtain

$$\begin{aligned} S_G &= \frac{1}{g^2}\sum_{n\in\Lambda}\sum_{\mu\neq\nu}\mathrm{tr}(\mathbf{1} - U_{\mu\nu}(n)) \\ &= \frac{1}{g^2}\sum_{n\in\Lambda}\sum_{\mu\neq\nu}\mathrm{tr}(-ia^2 F_{\mu\nu}(n) - a^3 B' - a^4 C' + \frac{a^4}{2}F^2_{\mu\nu}(n) + \mathcal{O}(a^5)). \end{aligned} \tag{A.13}$$

(A.14)

Since the generator of SU(3) T^a is trace-less, $\mathrm{tr}F_{\mu\nu} = \mathrm{tr}B'_{\mu\nu} = \mathrm{tr}C'_{\mu\nu} = 0$ is held. Therefore, at the limit of $a \to 0$, the Wilson gauge action reproduces the continuum gauge action as

$$S_G \to \frac{1}{2g^2}\int d^4x \mathrm{tr}F^2_{\mu\nu}. \tag{A.15}$$

Appendix B

Cubic and tetragonal symmetries

In this appendix, we summarize the rotational symmetry properties of lattice QCD simulations.

B.1 Cubic symmetry group

Lattice QCD simulations are performed in a finite spatial box, therefore the continuum rotational symmetry of the system reduces to the symmetries which keep the box invariant. In the center-of-mass frame, the reduced symmetry group is called the cubic group, denoted by O_h. The cubic group consists of 48 components: 10 rotations around x, y, z axis, 8 rotations around the threefold axis, 6 rotations around the twofold symmetry axis, and their 24 parity partners. We schematically show typical rotations in Figure B.1. There are 10 irreducible representations in

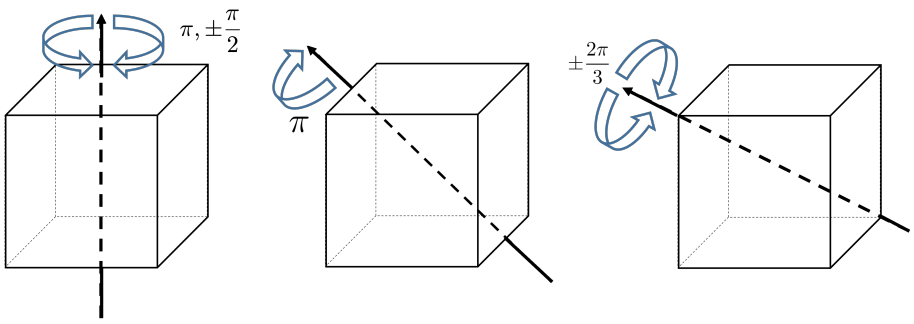

FIGURE B.1: Representative rotations in the cubic symmetry group. (Left) rotation around z-axis. (Middle) rotation around twofold symmetry axis. (Right) rotation around threefold symmetry axis.

the cubic group O_h: 1 dimensional representations $A_1^{\pm}$ and $A_2^{\pm}$; 2 dimensional representation $E^{\pm}$; and 3 dimensional representations $T_1^{\pm}$, $T_2^{\pm}$. Superscripts represent parity property. The energy eigenstates obtained in lattice QCD belong to those irreducible representations. In the scattering analysis in lattice QCD, the relation between irreducible representations of O_h and representations of continuum rotational group $O(3)$ is important to extract a certain partial wave component. By using the group theory, we obtain the relation summarized in Tab. B.1. For example, to analyze some S-wave ($l = 0$) scattering in lattice QCD, we have to study energy eigenstates belonging to A_1^+ irreducible representation.

TABLE B.1: Relation between partial waves and irreducible representations of the cubic group.

Partial wave rep.	Cubic irrep.
$l=0$	A_1^+
$l=1$	T_1^-
$l=2$	E^+, T_2^+
$l=3$	T_1^-, A_2^-, T_2^-
$l=4$	A_1^+, E^+, T_1^+, T_2^+

The projection of operators into a certain irreducible representation is achieved by acting the following projection:

$$P_j^{(\Gamma)} = \frac{n_\Gamma}{N} \sum_{g\in G} \Gamma^*_{jj}(g) R(g), \tag{B.1}$$

where $R(g)$ is some representation of the group O_h, $\Gamma(g)$ is a target irreducible representation with dimension n_Γ, N is a rank of O_h. Sometimes the traced projection is utilized as well,

$$P^{(\Gamma)} = \sum_j \frac{n_\Gamma}{N} \sum_{g\in G} \Gamma^*_{jj}(g) R(g) = \frac{n_\Gamma}{N} \sum_{g\in G} \chi^*(g) R(g), \tag{B.2}$$

where $\chi(g)$ is the character of $g \in O_h$. For instance, when we consider the operator which transforms under the cubic group as

$$\mathcal{O} \to U_R(g) \mathcal{O} U_R^\dagger(g), \tag{B.3}$$

the projected operator is given as

$$\mathcal{O}_j^\Gamma = P_j^{(\Gamma)} \mathcal{O} = \frac{n_\Gamma}{N} \sum_{g\in G} \Gamma^*_{jj}(g) U_R(g) \mathcal{O} U_R^\dagger(g). \tag{B.4}$$

B.2 Tetragonal symmetry group

In the laboratory frame calculation, the shape of the box changes due to the Lorentz contraction when the system is boosted back to the center-of-mass frame, and therefore the reduced symmetry group becomes smaller than the cubic group. Let us consider the case of our study, where total momenta are along with the z-axis. In that case, the box changes to a rectangular of $L \times L \times \gamma L$ with a boost factor γ. The symmetry group of such a rectangular is called the tetragonal symmetry group, denoted by D_{4h}. This symmetry group consists of 16 components: 4 rotations around $\mathbf{e}_z$; 4 rotations around $\mathbf{e}_x, \mathbf{e}_y, \mathbf{e}_x + \mathbf{e}_y, \mathbf{e}_x - \mathbf{e}_y$; and those multiplied by the reflection with respect to the (x, y)-plane. We show schematic figures of typical rotations in Figure B.2.

There are 10 irreducible representations in the tetragonal group D_{4h}: 1 dimensional representations $A_1^\pm$, $A_2^\pm$, $B_1^\pm$, $B_2^\pm$; and 2 dimensional representation $E^\pm$. The relation between those irreducible representations and the partial wave components is summarized in Tab. B.2. The

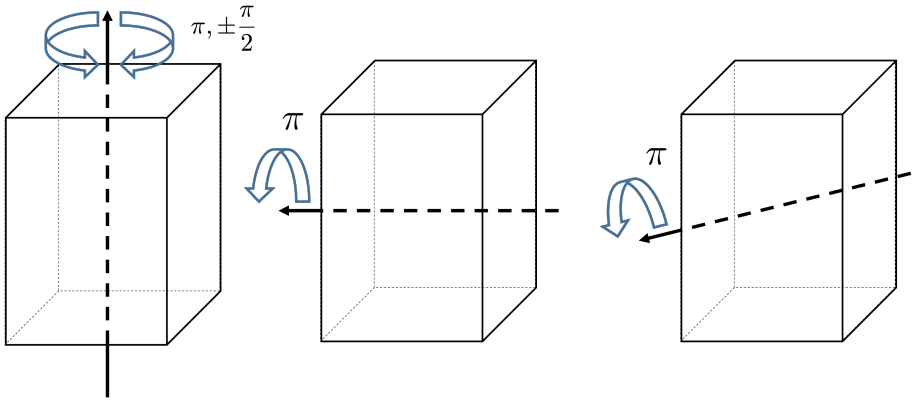

FIGURE B.2: Representative rotations in the tetragonal symmetry group. (Left) rotation around z-axis. (Middle) rotation around y-axis. (Right) rotation around $\mathbf{e}_x - \mathbf{e}_y$.

TABLE B.2: Relation between partial waves and irreducible representations of the tetragonal group. The coefficient in front of the irrep names represents multiplicity of appearance.

Partial wave rep.	Tetragonal irrep.
$l = 0$	A_1^+
$l = 1$	A_2^-, E^-
$l = 2$	A_1^+, B_1^+, B_2^+, E^+
$l = 3$	$A_2^-, B_1^-, B_2^-, 2E^-$

projection of the operator can be done as the cubic group.

Appendix C

Details of dilution

In this appendix, we summarize details of the dilution we employ in our study. To utilize the dilution technique, we need to determine the rules to split a single noise vector into diluted vectors as

$$\eta_{a\alpha}(\mathbf{x}, t) = \sum_{i=0}^{N_{\rm dil}-1} \eta^{(i)}_{a\alpha}(\mathbf{x}, t). \tag{C.1}$$

Since the noise vector generally has indices of color, spinor, and spacetime, we can consider a lot of splitting rules by combining the different kinds of indices. In the following, we introduce splitting rules of each kind of indices: color, spinor, time, and space. We combine them in practice.

C.1 Color dilution

As the color index consists of just three components, we employ a full dilution in this index as

$$\eta = \sum_{i=0}^{2} \eta^{(i)}_{\rm color}, \tag{C.2}$$

where each diluted vector only contains information of one of three color components as

$$(\eta^{(i)}_{\rm color})_{a\alpha}(\mathbf{x}, t) = 0 \ (\text{if i} \neq \text{a}). \tag{C.3}$$

C.2 Spinor dilution

The spinor index is also fully diluted as

$$\eta = \sum_{i=0}^{3} \eta^{(i)}_{\rm spinor}, \tag{C.4}$$

where $\eta^{(i)}_{\rm spinor}$ satisfies

$$(\eta^{(i)}_{\rm spinor})_{a\alpha}(\mathbf{x}, t) = 0 \ (\text{if i} \neq \alpha). \tag{C.5}$$

In our study, we always employ color and spinor dilution.

C.3 Time dilution

For time dilution, we employ not only the full dilution but also the interlaced one.

C.3.1 Full dilution

The full time dilution is almost trivial as the case of color and spinor indices. It is defined as

$$\eta = \sum_{i=0}^{Nt-1} \eta_{\mathrm{t}}^{(i)}, \tag{C.6}$$

where N_t is the time extent of considering lattice box and $\eta_{\mathrm{t}}^{(i)}$ contains information of each timeslices as

$$(\eta_{\mathrm{t}}^{(i)})_{a\alpha}(\mathbf{x}, t) = 0 \ (\mathrm{if\ i} \neq \mathrm{t}). \tag{C.7}$$

C.3.2 J-interlace dilution

In contrast to the full dilution, J-interlace dilution is somewhat non-trivial. In this dilution, we define the diluted vector $\eta_{\mathrm{t}-J\mathrm{int}}^{(i)}$ as

$$\eta = \sum_{i=0}^{Nt-1} \eta_{\mathrm{t}-J\mathrm{int}}^{(i)}, \tag{C.8}$$

with

$$(\eta_{\mathrm{t}-J\mathrm{int}}^{(i)})_{a\alpha}(\mathbf{x}, t) = 0 \ (\mathrm{if}\ i \neq t \bmod J). \tag{C.9}$$

We show a schematic figure in the case of 4-interlace dilution with full time extent of $N_t = 8$.

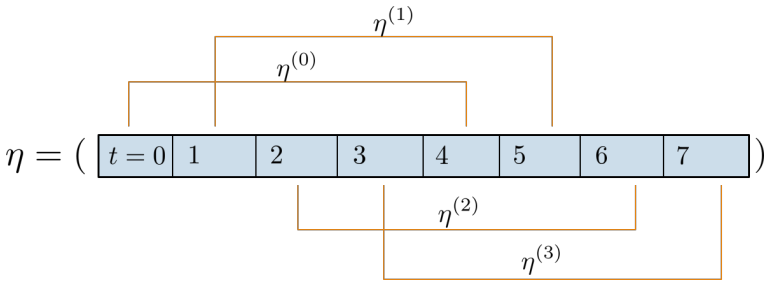

FIGURE C.1: schematic figure of 4-interlace dilution with $N_t = 8$.

C.4 Space dilution

The space dilution is the most non-trivial one in comparison with other kinds of dilution. In our study, we employ $s2$(even-odd), $s4$, $s8$ dilutions and their combination.

C.4.1 $s2$(even-odd) dilution

The $s2$ (even-odd) dilution splits the noise vector into two diluted vectors by considering the evenness and oddness of summations of spatial coordinates, $n_x + n_y + n_z$.

$$\eta = \eta_{\mathrm{s2}}^{(0)} + \eta_{\mathrm{s2}}^{(1)}, \tag{C.10}$$

with

$$\eta_{\mathrm{s2}}^{(i)} \neq 0, \quad \text{if } n_x + n_y + n_z = i \bmod 2, \tag{C.11}$$

A schematic picture is shown in Fig. C.2.

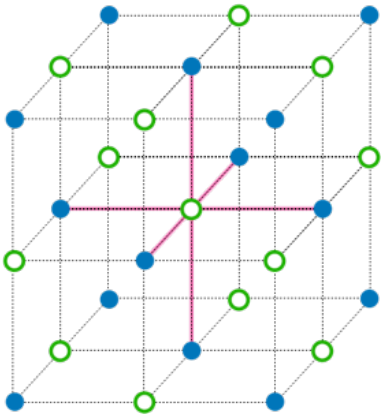

FIGURE C.2: Schematic picture of the $s2$(even-odd) dilution

C.4.2 $s4$ dilution

$s4$ dilution is taken so that the discretized Laplacian refer as independent diluted vectors as possible. It splits the noise vector into 4 diluted vectors as

$$\eta = \sum_{i=0}^{3} \eta_{\mathrm{s4}}^{(i)}, \tag{C.12}$$

The splitting rule is defined as follows:

$$\begin{cases} \eta_{\mathrm{s4}}^{(0)} \neq 0 & \text{if } (n_x, n_y, n_z) = \text{(even,even,even) or (odd,odd,odd)} \\ \eta_{\mathrm{s4}}^{(1)} \neq 0 & \text{if } (n_x, n_y, n_z) = \text{(odd,even,even) or (even,odd,odd)} \\ \eta_{\mathrm{s4}}^{(2)} \neq 0 & \text{if } (n_x, n_y, n_z) = \text{(even,odd,even) or (odd,even,odd)} \\ \eta_{\mathrm{s4}}^{(3)} \neq 0 & \text{if } (n_x, n_y, n_z) = \text{(odd,odd,even) or (even,even,odd)} \end{cases}. \tag{C.13}$$

A schematic picture is shown in Fig. C.3.

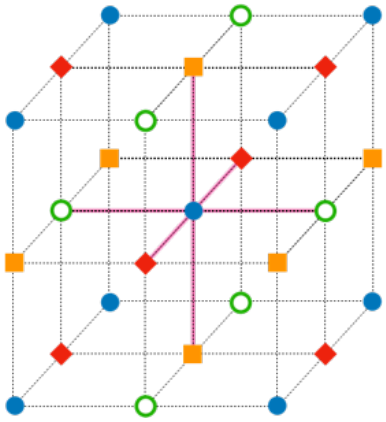

FIGURE C.3: Schematic picture of the $s4$ dilution

C.4.3 $s8$ dilution

The $s8$ dilution enables us to refer totally different diluted vectors in the discretized Laplacian.

$$\eta = \sum_{i=0}^{7} \eta_{s8}^{(i)} \tag{C.14}$$

The rule for splitting is defined as

$$
\begin{aligned}
\eta^{(0)} \neq 0 \quad \text{if} & \begin{cases} (n_x, n_y, n_z) = \text{(odd,odd,odd)} \text{ and } n_x + n_y + n_z = 1 \bmod 4 \\ (n_x, n_y, n_z) = \text{(even,even,even)} \text{ and } n_x + n_y + n_z = 2 \bmod 4 \end{cases} \\
\eta^{(1)} \neq 0 \quad \text{if} & \begin{cases} (n_x, n_y, n_z) = \text{(odd,odd,odd)} \text{ and } n_x + n_y + n_z = 3 \bmod 4 \\ (n_x, n_y, n_z) = \text{(even,even,even)} \text{ and } n_x + n_y + n_z = 0 \bmod 4 \end{cases} \\
\eta^{(2)} \neq 0 \quad \text{if} & \begin{cases} (n_x, n_y, n_z) = \text{(odd,even,even)} \text{ and } n_x + n_y + n_z = 1 \bmod 4 \\ (n_x, n_y, n_z) = \text{(even,odd,odd)} \text{ and } n_x + n_y + n_z = 2 \bmod 4 \end{cases} \\
\eta^{(3)} \neq 0 \quad \text{if} & \begin{cases} (n_x, n_y, n_z) = \text{(odd,even,even)} \text{ and } n_x + n_y + n_z = 3 \bmod 4 \\ (n_x, n_y, n_z) = \text{(even,odd,odd)} \text{ and } n_x + n_y + n_z = 0 \bmod 4 \end{cases} \\
\eta^{(4)} \neq 0 \quad \text{if} & \begin{cases} (n_x, n_y, n_z) = \text{(even,odd,even)} \text{ and } n_x + n_y + n_z = 1 \bmod 4 \\ (n_x, n_y, n_z) = \text{(odd,even,odd)} \text{ and } n_x + n_y + n_z = 2 \bmod 4 \end{cases} \\
\eta^{(5)} \neq 0 \quad \text{if} & \begin{cases} (n_x, n_y, n_z) = \text{(even,odd,even)} \text{ and } n_x + n_y + n_z = 3 \bmod 4 \\ (n_x, n_y, n_z) = \text{(odd,even,odd)} \text{ and } n_x + n_y + n_z = 0 \bmod 4 \end{cases} \\
\eta^{(6)} \neq 0 \quad \text{if} & \begin{cases} (n_x, n_y, n_z) = \text{(even,even,odd)} \text{ and } n_x + n_y + n_z = 1 \bmod 4 \\ (n_x, n_y, n_z) = \text{(odd,odd,even)} \text{ and } n_x + n_y + n_z = 2 \bmod 4 \end{cases} \\
\eta^{(7)} \neq 0 \quad \text{if} & \begin{cases} (n_x, n_y, n_z) = \text{(even,even,odd)} \text{ and } n_x + n_y + n_z = 3 \bmod 4 \\ (n_x, n_y, n_z) = \text{(odd,odd,even)} \text{ and } n_x + n_y + n_z = 0 \bmod 4 \end{cases}
\end{aligned}
\quad . \tag{C.15}
$$

See Fig. C.4 for a schematic figure of the $s8$ dilution.

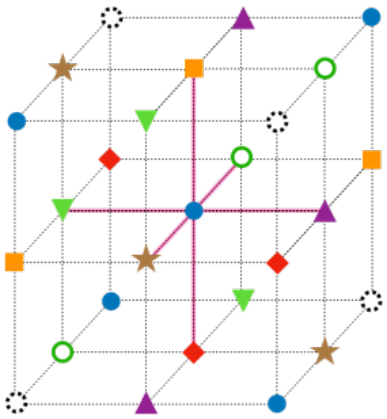

FIGURE C.4: Schematic picture of the $s8$ dilution

Appendix D

Correlation function of $\pi\pi$ interaction

In this appendix, we summarize definitions of correlation functions calculated in our study. Details on Wick contractions are explained as well.

D.1 Pion propagator

D.1.1 Definition

We define pion 2pt functions (pion propagator) as

$$C_{\mathbf{p}}(t-t_0) = \sum_{\mathbf{x},\mathbf{y}} e^{i\mathbf{p}\cdot\mathbf{y}} e^{-i\mathbf{p}\cdot\mathbf{x}} \langle \pi^+(\mathbf{x},t)\pi^-_{\mathrm{local/smear}}(\mathbf{y},t_0)\rangle, \tag{D.1}$$

where pion operators are defined as

$$\pi^+(\mathbf{x},t) = \bar{d}(\mathbf{x},t)\gamma_5 u(\mathbf{x},t), \tag{D.2}$$

$$\pi^-(\mathbf{x},t) = \bar{u}(\mathbf{x},t)\gamma_5 d(\mathbf{x},t). \tag{D.3}$$

$\pi_{\mathrm{local/smear}}$ at the source part represents a pion operator constructed by local or smeared quark fields. The source timeslice t_0 is averaged to improve the statistics in practice. The momentum projection of pion operators is done by the spatial summation with the exponential factor. Therefore, this correlation function contains single pion energies with spatial momentum $\mathbf{p}$, $E_\pi(\mathbf{p})$, as

$$C_{\mathbf{p}}(t-t_0) = Ce^{-E_\pi(\mathbf{p})(t-t_0)} + \cdots, \tag{D.4}$$

where C is an overlapping constant and ellipsis is the excited states contributions. In the continuum world, $E_\pi(\mathbf{p})$ is given as a dispersion relation of pion,

$$E_\pi(\mathbf{p}) = \sqrt{m_\pi^2 + \mathbf{p}^2}, \tag{D.5}$$

but in the lattice world it deviates from the continuum relation due to the finite lattice spacing. The formulation of the HAL QCD method is based on the continuum dispersion relation,

therefore in some cases involving non-zero momentum insertions (e.g. the laboratory frame calculations) it is better to check the deviation explicitly.

D.1.2 Wick contraction

After the Wick contraction, the correlation function becomes

$$\sum_{\mathbf{x},\mathbf{y}} e^{i\mathbf{p}\cdot\mathbf{y}} e^{-i\mathbf{p}\cdot\mathbf{x}} \langle \mathrm{tr}\left[D^{-1}(\mathbf{x},t;\mathbf{y},t_0)\gamma_5 D^{-1}(\mathbf{y},t_0;\mathbf{x},t)\gamma_5\right]\rangle_{\mathrm{gauge}}, \tag{D.6}$$

where $\langle\ \rangle_{\mathrm{gauge}}$ is a remaining path integral of gauge fields (Monte-Carlo simulations), and the trace is taken over the color and spinor indices. We also note that we ignore a flavor identification of quark propagators since we only consider the cases where up and down quark have the same mass, $m_u = m_d$.

D.2 $I = 2$ $\pi\pi$ S-wave correlation function

D.2.1 Definition

The most general definition of the correlation function for $I = 2$ $\pi\pi$ S-wave interaction is given as

$$F^{I=2}_{\pi\pi,\mathbf{P}}(\mathbf{x}, x^4, X^4 - X_0^4) = \sum_{\mathbf{X}} e^{-i\mathbf{P}\cdot\mathbf{X}} \langle \mathrm{T}\pi^+(X + x/2)\pi^+(X - x/2)\mathcal{J}_{\pi^+\pi^+}(\mathbf{P}, X_0^4)\rangle, \tag{D.7}$$

where $X = (\mathbf{X}, X^4)$ and $x = (\mathbf{x}, x^4)$ are the center-of-mass and relative coordinates between sink pions, $\mathbf{P}$ is a total momentum of the two-pion system. The source operator is defined as

$$\mathcal{J}_{\pi^+\pi^+}\left(\mathbf{P}, X_0^4\right) = \sum_{\mathbf{y},\mathbf{z}} e^{i\mathbf{p_1}\cdot\mathbf{y}} e^{i\mathbf{p_2}\cdot\mathbf{z}} \pi^-_{\mathrm{local/smear}}\left(\mathbf{y}, X_0^4\right) \pi^-_{\mathrm{local/smear}}\left(\mathbf{z}, X_0^4\right), \tag{D.8}$$

with $\mathbf{P} = \mathbf{p_1} + \mathbf{p_2}$. This source operator overlaps to states which have an isospin $I = 2, I_z = 2$, partial wave $l = 0$, and total momentum $\mathbf{P}$. The correlation function contains the NBS wave functions ϕ as

$$F^{I=2}_{\pi\pi,\mathbf{P}}(\mathbf{x}, x^4, X^4 - X_0^4) = \sum_n A_n \phi_{W_n}(\mathbf{x}, x^4) e^{-W_n(X^4 - X_0^4)} + \cdots, \tag{D.9}$$

where $A_n = \langle n|\mathcal{J}_{\pi^+\pi^+}(\mathbf{P}, 0)\rangle$ is an overlapping factor of the elastic n-th state, W_n is the energy of the n-th elastic state, and the ellipsis is the inelastic contribution.

D.2.2 Wick contraction

Next, let us consider the estimation of the correlation function introduced above. After the Wick contraction, the correlation function is rewritten by the summation of the two types of diagrams. Representative Wick contraction diagrams is shown in FigureD.1.

FIGURE D.1: Representative diagrams appearing in the $I = 2$ $\pi\pi$ correlation function. Gray arrows represent quark propagations and paired $\bar{q}q$ combinations correspond to each pion operators. In this cartoons, we show the source operators on the right hand side.

There are two types of diagram, one without any quark exchange between two pions (we call it "separated diagram"), the other with a single quark exchange (we call it "connected diagram"). Both types have the other contribution with flipped spatial coordinates of sink pions, but we do not discuss them since they can be immediately estimated from the representatives.

Separated diagram

The separated diagram corresponds to the following Wick contraction:

$$\langle \bar{d}\gamma_5 u(X + x/2)\bar{d}\gamma_5 u(X - x/2)\bar{u}\gamma_5 d(\mathbf{y}, X_0^4)\bar{u}\gamma_5 d(\mathbf{z}, X_0^4)\rangle, \tag{D.10}$$

where we abbreviate summation and exponential factors. After integrating quark fields, it becomes

$$\begin{aligned}(+)\langle \mathrm{tr}\left[D^{-1}(\mathbf{X} + \mathbf{x}/\mathbf{2}, X^4 + x^4/2; \mathbf{y}, X_0^4)\gamma_5 D^{-1}(\mathbf{y}, X_0^4; \mathbf{X} + \mathbf{x}/\mathbf{2}, X^4 + x^4/2)\gamma_5\right] \\ \times \mathrm{tr}\left[D^{-1}(\mathbf{X} - \mathbf{x}/\mathbf{2}, X^4 - x^4/2; \mathbf{z}, X_0^4)\gamma_5 D^{-1}(\mathbf{z}, X_0^4; \mathbf{x}, \mathbf{X} - \mathbf{x}/\mathbf{2}, X^4 - x^4/2)\gamma_5\right]\rangle_{\mathrm{gauge}},\end{aligned} \tag{D.11}$$

where $\langle\ \rangle_{\mathrm{gauge}}$ is a remaining path integral of gauge fields (Monte-Carlo simulations), and the trace is taken over the color and spinor indices.

Connected diagram

The Wick contraction of the connected diagram is

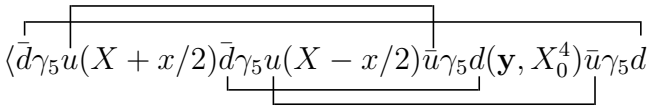

$$\langle \bar{d}\gamma_5 u(X+x/2)\bar{d}\gamma_5 u(X-x/2)\bar{u}\gamma_5 d(\mathbf{y},X_0^4)\bar{u}\gamma_5 d(\mathbf{z},X_0^4)\rangle, \tag{D.12}$$

and by performing quark integrals, we obtain

$$\begin{aligned}(-)\langle \mathrm{tr}\big[&D^{-1}(\mathbf{X}+\mathbf{x}/\mathbf{2},X^4+x^4/2;\mathbf{y},X_0^4)\gamma_5 D^{-1}(\mathbf{y},X_0^4;\mathbf{X}-\mathbf{x}/\mathbf{2},X^4-x^4/2)\\ &\times\gamma_5 D^{-1}(\mathbf{X}-\mathbf{x}/\mathbf{2},X^4-x^4/2;\mathbf{z},X_0^4)\gamma_5 D^{-1}(\mathbf{z},X_0^4;\mathbf{X}+\mathbf{x}/\mathbf{2},X^4+x^4/2)\gamma_5\big]\rangle_{\mathrm{gauge}}.\end{aligned} \tag{D.13}$$

D.3 $I=1$ $\pi\pi$ P-wave correlation function

D.3.1 Definition

The correlation function for the $I=1$ $\pi\pi$ P-wave interaction is defined as

$$F^{I=1}_{\pi\pi,\mathbf{P}=\mathbf{0}}(\mathbf{r},t-t_0)=\sum_{t_0}\langle(\pi\pi)_{I=1,I_z=0}(\mathbf{r},t)\overline{\mathcal{J}}^{T_1^-}_{I=1,I_z=0}(t_0)\rangle, \tag{D.14}$$

where we only consider the center-of-mass frame, $\mathbf{P}=\mathbf{0}$. In our study, the sink operator is chosen as

$$(\pi\pi)_{I=1,I_z=0}(\mathbf{r},t)=\frac{1}{\sqrt{2}}\{\pi^+(\mathbf{r}+\mathbf{x},t+\Delta t)\pi^-(\mathbf{x},t)-\pi^-(\mathbf{r}+\mathbf{x},t+\Delta t)\pi^+(\mathbf{x},t)\}, \tag{D.15}$$

with fixed Δt for the application of the hybrid method, and

$$(\pi\pi)_{I=1,I_z=0}(\mathbf{r},t)=\frac{1}{\sqrt{2}}\{\pi^+_{\mathrm{smear}}(\mathbf{r}+\mathbf{x},t)\pi^-_{\mathrm{smear}}(\mathbf{x},t)-\pi^-_{\mathrm{smear}}(\mathbf{r}+\mathbf{x},t)\pi^+_{\mathrm{smear}}(\mathbf{x},t)\}, \tag{D.16}$$

for the ρ resonance study. The coordinate $\mathbf{x}$ is fixed somewhere, but the NBS wave function is independent of it due to the translational invariance. Both choices are suitable for the reduction of systematics in each calculation and are discussed in detail in the main part. As regards the source operator, we can choose two different types of the source operator as

$$\overline{\mathcal{J}}^{T_1^-}_{\rho,I=1,I_z=0}(t_0) = \overline{\rho}^0_3(t_0), \tag{D.17}$$

$$\overline{\mathcal{J}}^{T_1^-}_{\pi\pi,I=1,I_z=0}(t_0) = \overline{(\pi\pi)}_{I=1,I_z=0}(\mathbf{p}_3,t_0), \tag{D.18}$$

where $\mathbf{p}_3 = (0, 0, 2\pi/L)$ is a back-to-back relative momentum of two pion operators, $\overline{(\pi\pi)}_{I=1,I_z=0}(\mathbf{p}, t)$ and $\overline{\rho}^0_3$ are defined as

$$\overline{\rho}^0_3(t) = \sum_{\mathbf{z}} \frac{1}{\sqrt{2}} \left(\bar{u}(\mathbf{z}, t)\gamma_3 u(\mathbf{z}, t) - \bar{d}(\mathbf{z}, t)\gamma_3 d(\mathbf{z}, t)\right) \tag{D.19}$$

$$\overline{(\pi\pi)}_{I=1,I_z=0}(\mathbf{p}, t) = \frac{1}{\sqrt{2}} \sum_{\mathbf{y_1},\mathbf{y_2}} e^{-i\mathbf{p}\cdot\mathbf{y_1}} e^{i\mathbf{p}\cdot\mathbf{y_2}} \left(\pi^-(\mathbf{y_1}, t)\pi^+(\mathbf{y_2}, t) - \pi^+(\mathbf{y_1}, t)\pi^-(\mathbf{y_2}, t)\right). \tag{D.20}$$

Those operators overlap to states which has an isospin $I = 1, I_z = 0$, partial wave $l = 1$, and total momentum $\mathbf{P} = \mathbf{0}$. In the study of the hybrid method, we only consider the ρ type source of Eq. (D.18), since it is expected that this source strongly overlaps a bound state corresponding to the ρ meson. On the other hand, the ρ resonance study employs both types to determine the non-local potential at the next-to-next-to-leading order of approximation of the derivative expansion.

D.3.2 Wick contraction

Representative Wick contraction diagrams is shown in FigureD.2 and D.3.

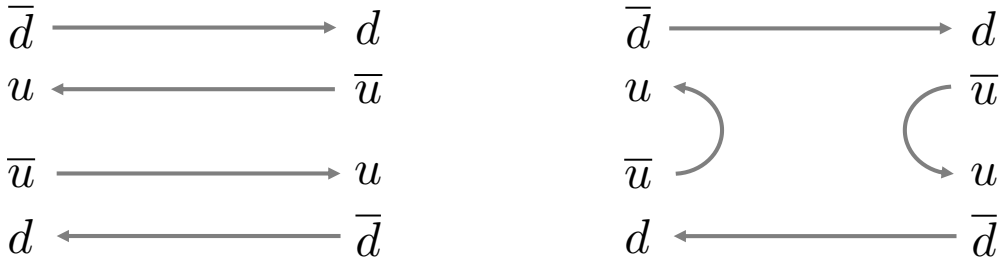

FIGURE D.2: Representative diagrams contributing to the correlation function with $\pi\pi$-type source operator.

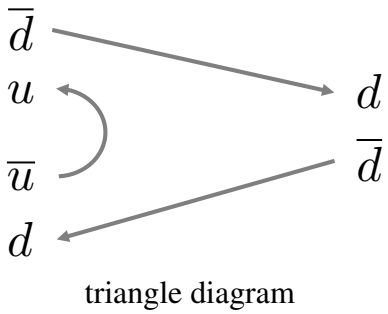

FIGURE D.3: Representative diagram contributing to the correlation function with ρ-type source operator.

In this calculation, there are new types of Wick contractions, namely box and triangle diagrams. Those diagrams contain a single quark creation/annihilation and they need all-to-all

propagators as already discussed. Naively, we can also consider another type of diagram called "disconnected diagram", in which quarks are totally annihilated in the source part and recreated in the sink part. Those disconnected contributions, however, are canceled due to the degeneracy of the up and down quark masses and we do not need to consider them here. As in the case of $I = 2$, there are some other contributions with flipped sink/source pions, but in the following we only focus on the representatives since others can be immediately estimated from the representatives or can be estimated similarly.

Separated diagram

The representative of the separated diagram corresponds to the following Wick contraction:

$$\langle \bar{d}\gamma_5 u(\mathbf{x}+\mathbf{r},t)\bar{u}\gamma_5 d(\mathbf{x},t)\bar{u}\gamma_5 d(\mathbf{y_1},t_0)\bar{d}\gamma_5 u(\mathbf{y_2},t_0)\rangle, \tag{D.21}$$

After integrating quark fields, it becomes

$$\begin{aligned}(+)\langle \mathrm{tr}\left[D^{-1}(\mathbf{x}+\mathbf{r},t;\mathbf{y_1},t_0)\gamma_5 D^{-1}(\mathbf{y_1},t_0;\mathbf{x}+\mathbf{r},t)\gamma_5\right] \\ \times \mathrm{tr}\left[D^{-1}(\mathbf{x},t;\mathbf{y_2},t_0)\gamma_5 D^{-1}(\mathbf{y_2},t_0;\mathbf{x},t)\gamma_5\right]\rangle_{\mathrm{gauge}},\end{aligned} \tag{D.22}$$

where the trace is taken on the color and spinor indices.

Box diagram

The Wick contraction of the representative box diagram is

$$\langle \bar{d}\gamma_5 u(\mathbf{x}+\mathbf{r},t)\bar{u}\gamma_5 d(\mathbf{x},t)\bar{u}\gamma_5 d(\mathbf{y_1},t_0)\bar{d}\gamma_5 u(\mathbf{y_2},t_0)\rangle, \tag{D.23}$$

and we obtain

$$\begin{aligned}(-)\langle \mathrm{tr}\big[D^{-1}(\mathbf{x}+\mathbf{r},t;\mathbf{x},t)\gamma_5 D^{-1}(\mathbf{x},t;\mathbf{y_2},t_0) \\ \times \gamma_5 D^{-1}(\mathbf{y_2},t_0;\mathbf{y_1},t_0)\gamma_5 D^{-1}(\mathbf{y_1},t_0;\mathbf{x}+\mathbf{r},t)\gamma_5\big]\rangle_{\mathrm{gauge}}.\end{aligned} \tag{D.24}$$

Triangle diagram

The Wick contraction of the representative triangle diagram is

$$\langle \bar{d}\gamma_5 u(\mathbf{x}+\mathbf{r},t)\bar{u}\gamma_5 d(\mathbf{x},t)\bar{d}\gamma_5 d(\mathbf{z},t_0)\rangle, \tag{D.25}$$

and we obtain

$$(-)\langle \mathrm{tr}\big[D^{-1}(\mathbf{x}+\mathbf{r},t;\mathbf{x},t)\gamma_5 D^{-1}(\mathbf{x},t;\mathbf{z},t_0)\gamma_3 D^{-1}(\mathbf{z},t_0;\mathbf{x}+\mathbf{r},t)\gamma_5\big]\rangle_{\mathrm{gauge}}. \tag{D.26}$$

Details of estimations of those diagrams in our studies will be discussed in the main part.

Appendix E

Smeared sink scheme

In this appendix, we discuss properties of the smeared-sink scheme in details.

E.1 Point-sink scheme vs smeared-sink scheme

To see why we need the smeared-sink scheme for the $I = 1$ $\pi\pi$ potential, let us compare potentials between the point-sink scheme and the smeared-sink scheme. Figure E.1 (left) shows the potentials obtained from the $\pi\pi$-type source with $N_{\rm conf} = 18$ ($\times$ 64 timeslice average). While the potential in the point-sink scheme shows large non-smooth and scattered behavior at small r, which makes a potential fit difficult, such behavior is absent for the potential in the smeared-sink scheme. If we calculate the potential in the point-sink scheme without including box diagrams, such non-smooth behavior does not appear (Fig. E.1 (right)). Therefore, it is probably caused by box diagrams, which contain quark creation/annihilations.

We suspect that this non-smooth and scattered structure is related to a singular behavior of the NBS wave function at short distances, caused by quark creation/annihilations. According to the argument by the operator product expansion[82–86], the sink operator strongly couples to the ρ-type operator at short distance, whose mass dimension is lower than the $\pi\pi$-type operator by 3, therefore the NBS wave function behaves as $\psi_W(\mathbf{r}) \sim \frac{1}{r^3} Y_{l=1,m=0}(\Omega_{\mathbf{r}})$ at short distances. This implies that the NBS wave function is highly localized and singular around the origin. Indeed, in the point-sink scheme this is the case as seen in Fig.E.2 (Left). Since data available at short distances are restricted on a discretized space, it is difficult to extract a potential smoothly from such a localized wave function by a discretized Laplacian. In the smeared-sink scheme, on the other hand, such a singular structure of the NBS wave function is much milder as seen in Fig.E.2 (Right), so that the potential reconstructed from discrete data is smoother at short distances. We also expect similar behaviors of HAL QCD potentials at short distances for other systems which allow quark creation/annihilations.

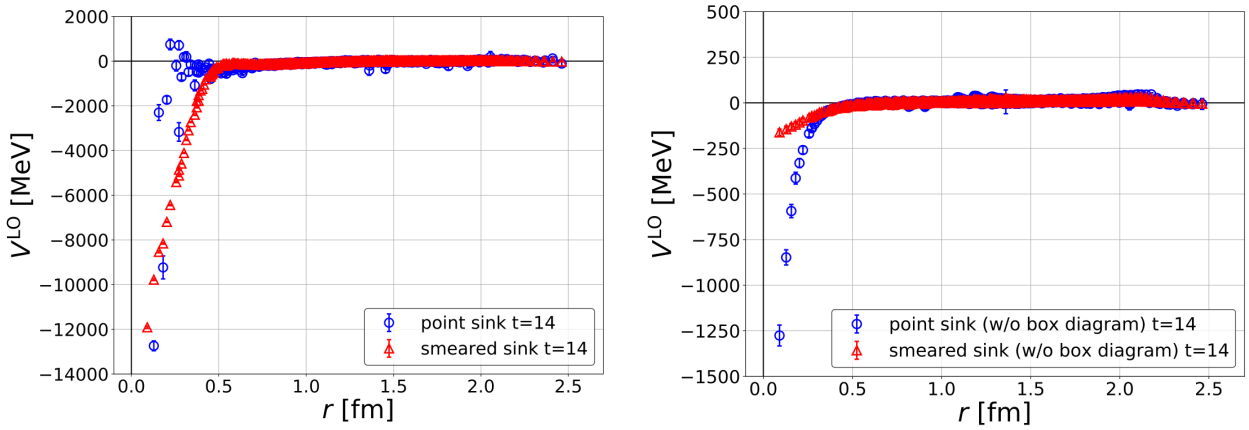

FIGURE E.1: A comparison in $I = 1$ $\pi\pi$ potential between two schemes at $t = 14$. (Left) The effective LO potentials from the $\pi\pi$-type source operator. Blue (red) points show data in the point-sink (smeared-sink) scheme. (Right) Those from the NBS wave function without box diagrams.

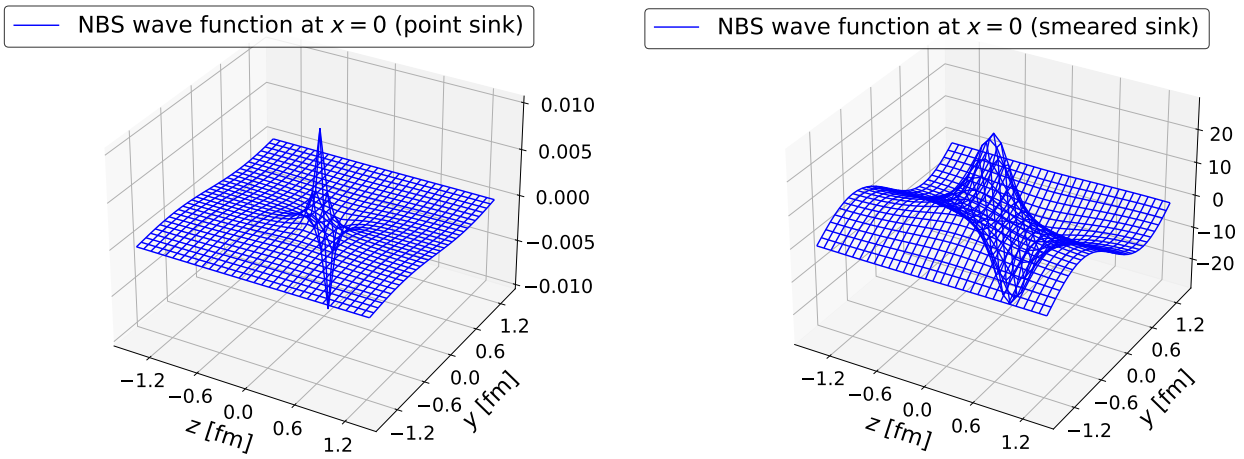

FIGURE E.2: The NBS wave function at $x = 0$ in the point-sink scheme (Left) and the smeared-sink scheme (Right).

E.2 Effect on the derivative expansion

The previous HAL QCD study with the LapH method [26] has revealed that the LapH sink-smearing significantly enhances non-localities of HAL QCD potentials, which makes the derivative expansion less reliable. Therefore we would like to check whether our sink-smearing scheme is free from such a problem. For this purpose, we calculate $I = 2$ $\pi\pi$ potential in both point-sink and smeared-sink schemes and compare LO phase shifts.

Calculations of NBS wave functions in both schemes are performed using the one-end trick with full color/spin dilution and $s2$ space dilution for a single Z_4 noise. We employ $N_{\rm conf} = 10$ ($\times 64$ timeslice average) gauge configurations and statistical errors are estimated by the jackknife method with bin-size 1.

Figure E.3(left) shows effective LO potentials at $t = 14$. Potentials between two schemes show different behaviors only at small r, which however do not affect phase shifts in a low-energy region, as plotted in Fig. E.3 (right). Thus our smeared-sink scheme does not enhance non-locality of the $I = 2$ $\pi\pi$ potential in this energy region. Since a energy range relevant for the ρ resonance in this study is well covered by $\sqrt{s} < 1200$ MeV, we expect that non-locality of the $I = 1$ $\pi\pi$ potential is not enhanced by the smeared-sink scheme, either.

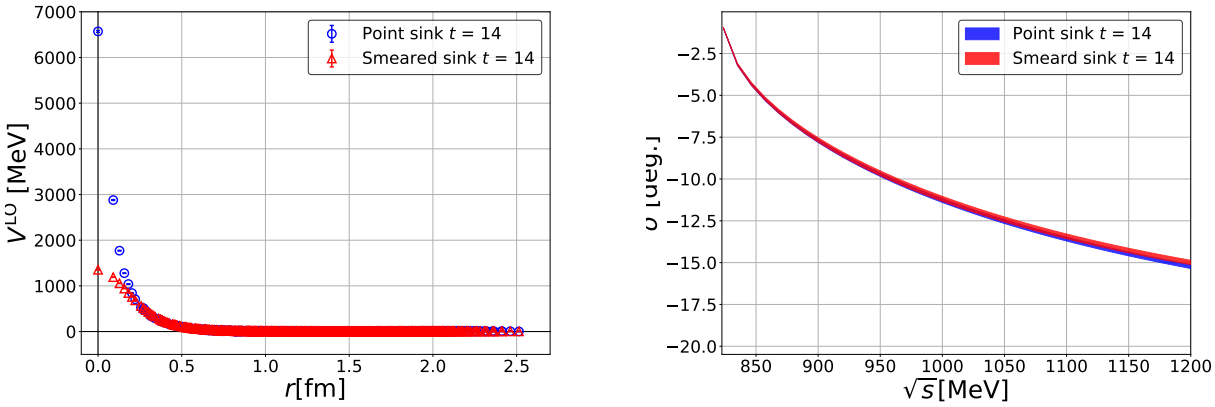

FIGURE E.3: A comparison between point-sink and smeared-sink schemes for the $I = 2$ $\pi\pi$ system. (Left) Effective LO potentials. Blue (red) points show data in the point-sink (smeared-sink) scheme. (Right) Corresponding phase shifts.

Appendix F

Laboratory frame calculation: Estimation of systematic uncertainty

In this appendix, we discuss estimation of the systematic uncertainty of the scattering phase shift shown in Chap. 7. We investigate two aspects of the potential: normalization dependence and X^4 dependence. In the former investigation, we consider another time-dependent method using a mass normalization. The R-correlators are defined as

$$R_{\mathbf{P}=\mathbf{e_z}}(\mathbf{x}, x^4, X^4) = \frac{F_{\pi^+\pi^+,\mathbf{e_z}}(\mathbf{x}, x^4, X^4)}{C_{\mathbf{0}}(X^4)^2} \tag{F.1}$$

$$R_{\mathbf{P}=\mathbf{2e_z}}(\mathbf{x}, x^4, X^4) = \frac{F_{\pi^+\pi^+,\mathbf{2e_z}}(\mathbf{x}, x^4, X^4)}{C_{\mathbf{0}}(X^4)^2}, \tag{F.2}$$

and the building blocks of the potential are modified to

$$G(\mathbf{x}, x^4, X^4) = \left((\partial_{X^4} - 2m)^2 - \mathbf{P}^2\right) R_{\mathbf{P}}(\mathbf{x}, x^4, X^4), \tag{F.3}$$

$$E(\mathbf{x}, x^4, X^4) = \frac{1}{4m}\left[\partial_{X^4}^2 - 4m\partial_{X^4} - \mathbf{P}^2\right] G(\mathbf{x}, x^4, X^4), \tag{F.4}$$

$$L_\perp(\mathbf{x}, x^4, X^4) = \nabla_\perp^2 G(\mathbf{x}, x^4, X^4), \tag{F.5}$$

$$L_\parallel(\mathbf{x}, x^4, X^4) = \left(-(\partial_{X^4} - 2m)\nabla_\parallel + i\mathbf{P}\partial_{x^4}\right)^2 R_{\mathbf{P}}(\mathbf{x}, x^4, X^4). \tag{F.6}$$

The LO potential is obtained by,

$$V^{\mathrm{LO}}_{x^{*4}=0}(\mathbf{x}_\perp) = \left.\frac{\left(L_\perp + L_\parallel + mE\right)(\mathbf{x}, x^4, X^4)}{mG(\mathbf{x}, x^4, X^4)}\right|_{x^4=0,\mathbf{x}_\parallel=0}. \tag{F.7}$$

As mentioned before, it is expected to give the same potential up to some systematics. Inversely, we can see the systematics from the difference between the two normalizations.

In the latter investigation, we compare potentials at $X^4 = 16 \pm 1$. In the following, we show both dependence and the final estimation of uncertainty of the phase shift.

F.1 Normalization dependence

First, let us see results using two different normalizations in the time-dependent method. Figure F.1 shows the normalization dependence of the effective LO potentials with non-zero total momenta, together with the center-of-mass result for a comparison. We observe a slight shift between the central values of the LO potential, although they are consistent statistically. Furthermore, we find that the shift behavior mainly comes from the energy term (see Figure F.2 and F.3). The estimation of k_m^2 involves discretized derivatives and dispersion relation, so the energy term suffers from the discretization error. We suspect the slight shift is the manifestation of the discretization error.

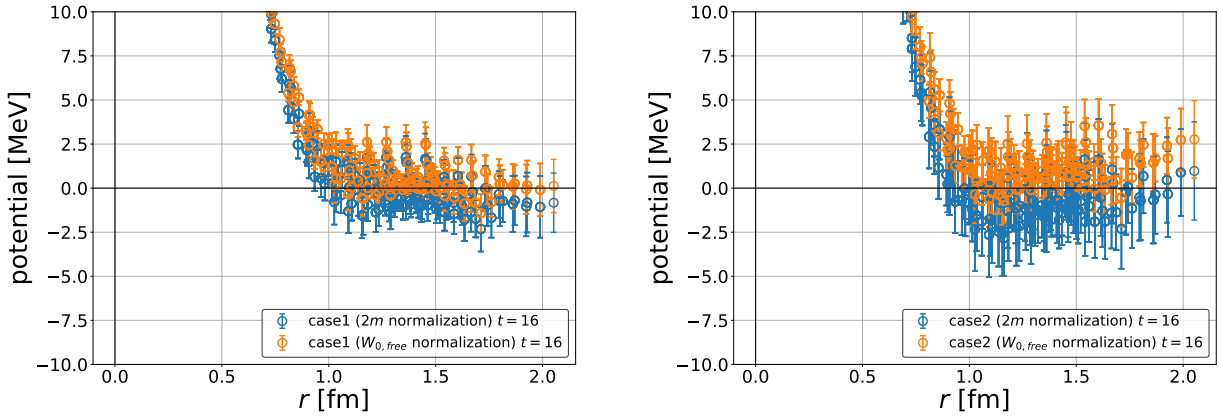

FIGURE F.1: Normalization dependence of the potential in the case 1 (Left) and case 2 (Right). We also show the center-of-mass result (black points) for comparison.

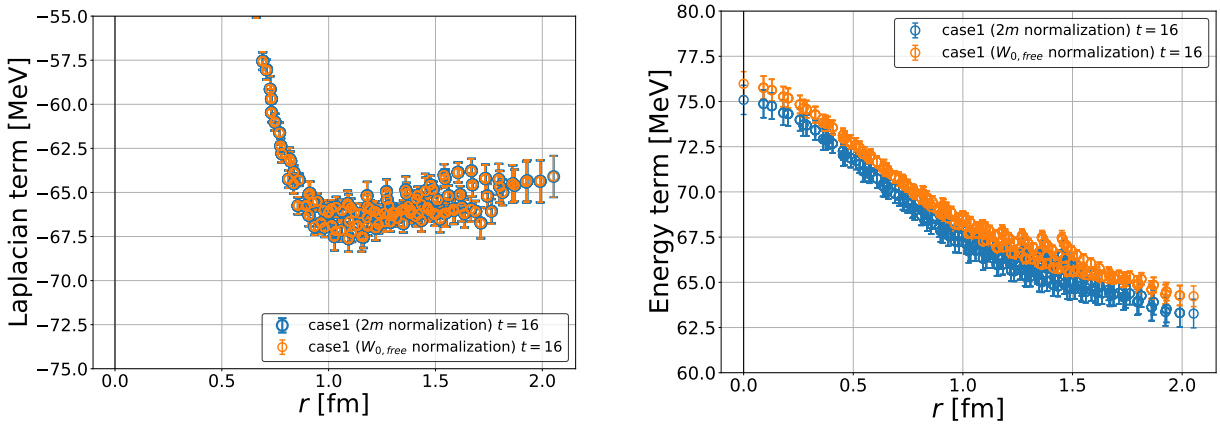

FIGURE F.2: Normalization dependence of the Laplacian (left) and energy term (right) in the case 1.

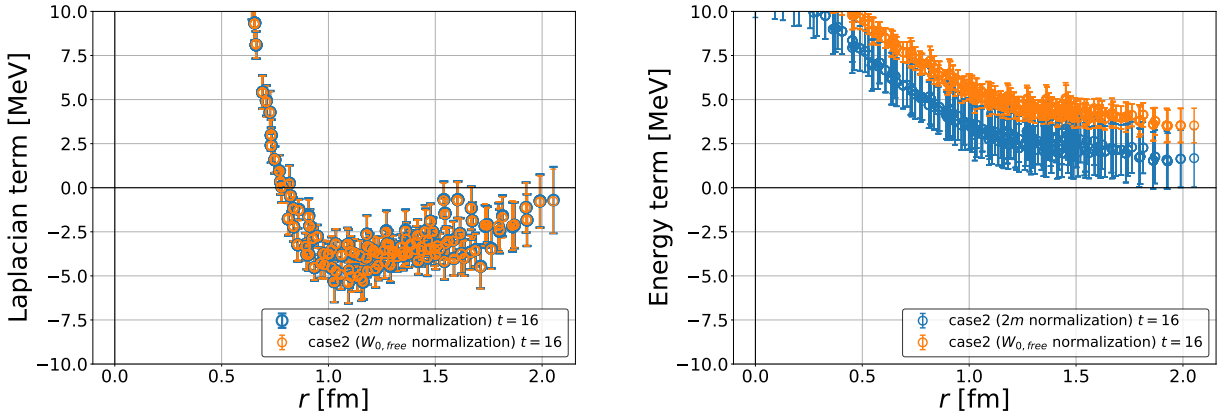

FIGURE F.3: Normalization dependence of the Laplacian (left) and energy term (right) in the case 2.

At first sight, it is not a problem within the statistics, but we observe that it affects the fit of the potential at a long distance in practice. To reduce the systematics as possible, we only use data at $r < 13$ in the potential fit since the long-range data is zero consistent. As seen in Fig. F.4, however, the remaining normalization dependence appears systematically as a weaker repulsive force for the $2m$ normalization. We, therefore, take this dependence into account in the estimation of the systematic uncertainty.

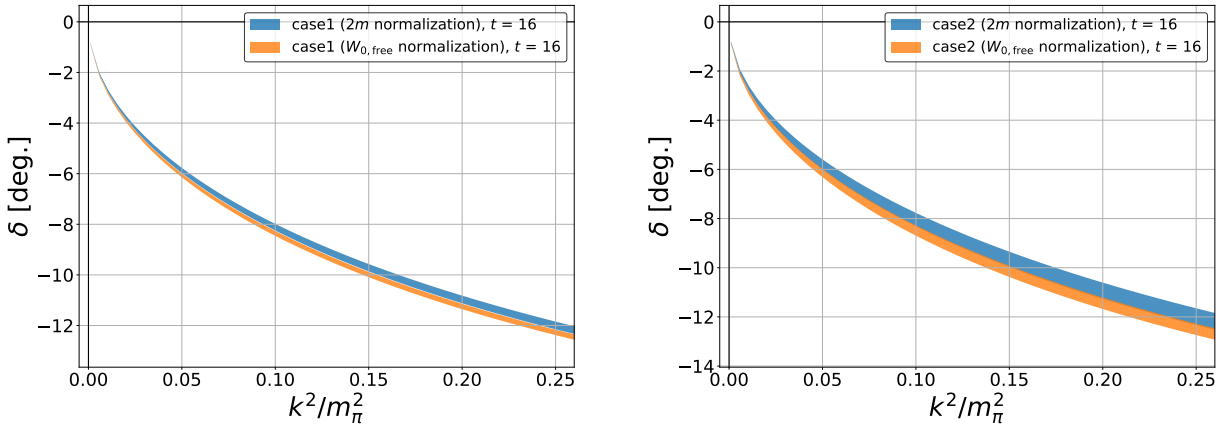

FIGURE F.4: Normalization dependence of the scattering phase shift at $X^4 = 16$ in the case 1 (left) and case 2 (right).

F.2 Timeslice dependence

Next, let us discuss the X^4 dependence of the potential. Figures F.5 and F.6 show the LO potential at $X^4 = 16 \pm 1$ in each total momentum sectors. As you can see, the potentials are consistent statistically, but the central values somewhat fluctuate. Such fluctuations can also affect the fit. We show the time dependence of the phase shift obtained by the $W_{0,\text{free}}$ normalization in Fig. F.7. The resultant phase shift fluctuates, so we also consider this dependence in the estimation of the systematics.

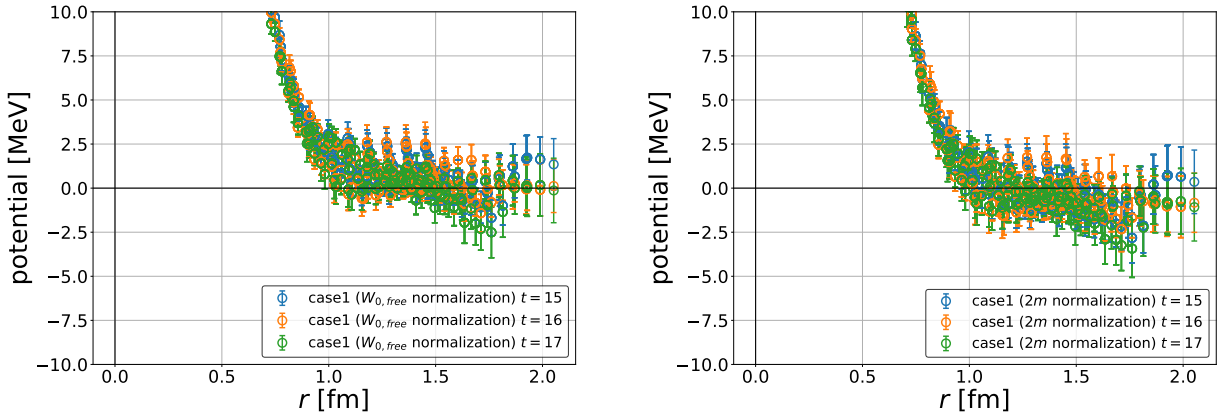

FIGURE F.5: X^4 dependence of the potential obtained from two normalizations using $W_{0,\mathrm{free}}$ (left) and $2m$ (right) in the case 1. The center-of-mass result at $X^4 = 16$ is shown as black points for a comparison.

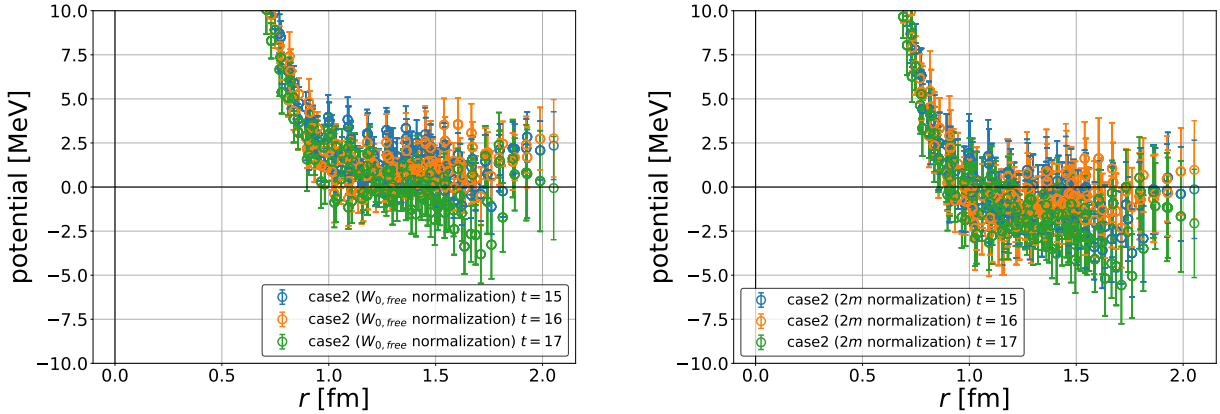

FIGURE F.6: X^4 dependence of the potential obtained from two normalizations using $W_{0,\mathrm{free}}$ (left) and $2m$ (right) in the case 2.

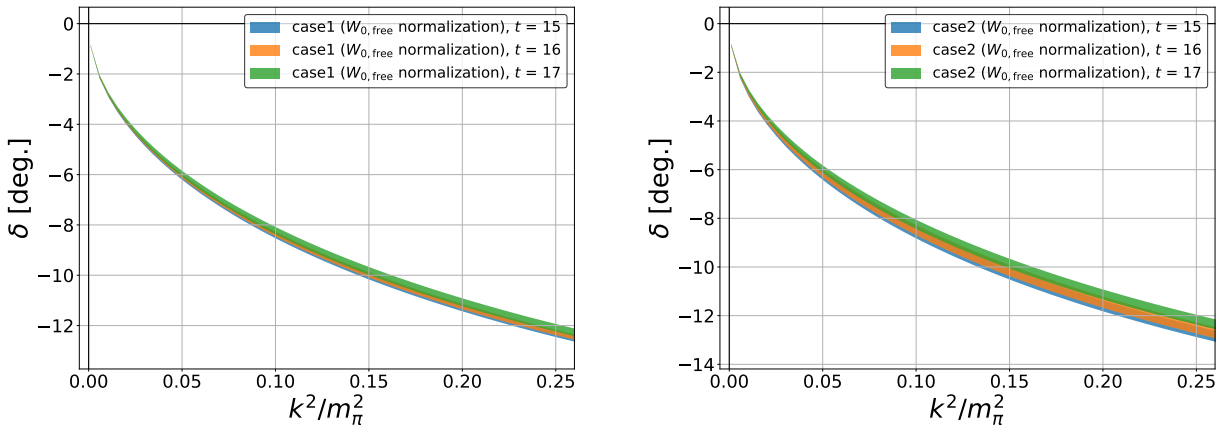

FIGURE F.7: X^4 dependence of the scattering phase shift using $W_{0,\mathrm{free}}$ normalization at $X^4 = 16$ in the case 1 (left) and case 2 (right). Almost the same X^4 dependence is observed in the case of $2m$ normalization.

F.3 Final estimation of uncertainty

Finally, let us discuss the final estimation of the systematic uncertainty. Since we observe both normalization dependence and X^4 dependence in the scattering phase shift, we estimate the systematic uncertainty by the difference of maximum and minimum of those data. Figure F.8 shows the final estimation of uncertainty of the scattering phase shift. Color bands include both statistical and systematic uncertainty. In the main text, we discuss consistency among different results including this systematic uncertainty.

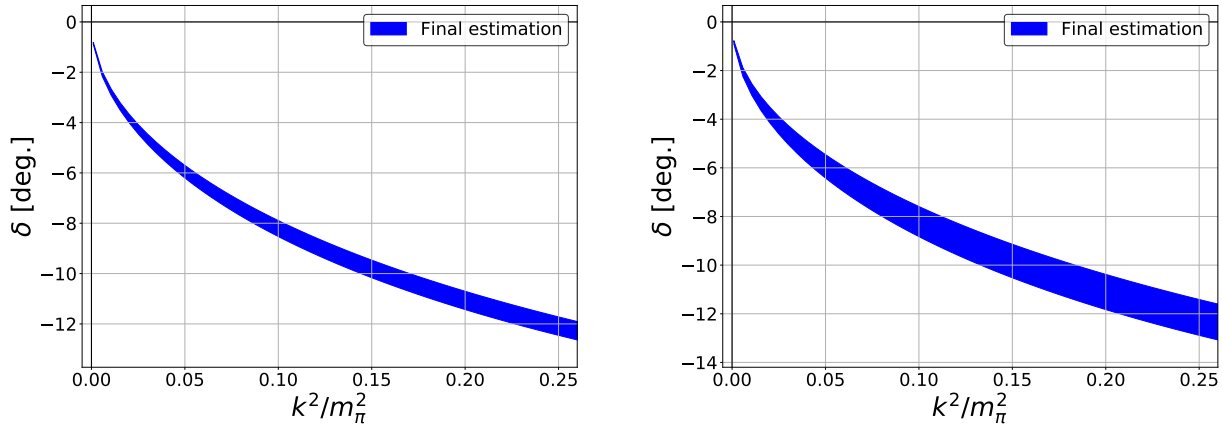

FIGURE F.8: Final estimation of uncertainty of the scattering phase shift. Color bands include both statistical and systematic uncertainty.

Bibliography

[1] M. Gell-Mann, Phys. Lett. **8**, 214 (1964).

[2] G. Zweig, (1964).

[3] G. Zweig, "An SU(3) model for strong interaction symmetry and its breaking. Version 2", in *DEVELOPMENTS IN THE QUARK THEORY OF HADRONS. VOL. 1. 1964 - 1978* (Feb. 1964), pp. 22–101.

[4] P. Zyla et al., PTEP **2020**, 083C01 (2020).

[5] S. K. Choi et al., Phys. Rev. Lett. **91**, 262001 (2003).

[6] Y.-R. Liu, H.-X. Chen, W. Chen, X. Liu, and S.-L. Zhu, Prog. Part. Nucl. Phys. **107**, 237 (2019).

[7] J. R. Pelaez, Phys. Rept. **658**, 1 (2016).

[8] K. G. Wilson, Phys. Rev. D **10**, 2445 (1974).

[9] M. Creutz, Phys. Rev. D **21**, 2308 (1980).

[10] S. Durr et al., Science **322**, 1224 (2008).

[11] L. Maiani and M. Testa, Physics Letters B **245**, 585 (1990).

[12] M. Luscher, Nucl. Phys. B **354**, 531 (1991).

[13] K. Rummukainen and S. A. Gottlieb, Nucl. Phys. B **450**, 397 (1995).

[14] M. T. Hansen and S. R. Sharpe, Phys. Rev. D **86**, 016007 (2012).

[15] R. A. Briceno, J. J. Dudek, and R. D. Young, Rev. Mod. Phys. **90**, 025001 (2018).

[16] N. Ishii, S. Aoki, and T. Hatsuda, Phys. Rev. Lett. **99**, 022001 (2007).

[17] S. Aoki, T. Hatsuda, and N. Ishii, Prog. Theor. Phys. **123**, 89 (2010).

[18] S. Aoki, Prog. Part. Nucl. Phys. **66**, 687 (2011).

[19] S. Aoki and T. Doi, Front. in Phys. **8**, 307 (2020).

[20] Y. Lyu, H. Tong, T. Sugiura, S. Aoki, T. Doi, T. Hatsuda, J. Meng, and T. Miyamoto, Phys. Rev. Lett. **127**, 072003 (2021).

[21] T. Iritani et al., Phys. Lett. B **792**, 284 (2019).

[22] S. Gongyo et al., Phys. Rev. Lett. **120**, 212001 (2018).

[23] Y. Ikeda, S. Aoki, T. Doi, S. Gongyo, T. Hatsuda, T. Inoue, T. Iritani, N. Ishii, K. Murano, and K. Sasaki, Phys. Rev. Lett. **117**, 242001 (2016).

[24] Y. Ikeda, J. Phys. G **45**, 024002 (2018).

[25] S. Acharya et al., Nature **588**, 232 (2020).

[26] D. Kawai, S. Aoki, T. Doi, Y. Ikeda, T. Inoue, T. Iritani, N. Ishii, T. Miyamoto, H. Nemura, and K. Sasaki, PTEP **2018**, 043B04 (2018).

[27] D. Kawai, EPJ Web Conf. **175**, 05007 (2018).

[28] M. Peardon, J. Bulava, J. Foley, C. Morningstar, J. Dudek, R. G. Edwards, B. Joo, H.-W. Lin, D. G. Richards, and K. J. Juge, Phys. Rev. D **80**, 054506 (2009).

[29] J. Foley, K. Jimmy Juge, A. O'Cais, M. Peardon, S. M. Ryan, and J.-I. Skullerud, Comput. Phys. Commun. **172**, 145 (2005).

[30] Y. Akahoshi, S. Aoki, T. Aoyama, T. Doi, T. Miyamoto, and K. Sasaki, PTEP **2019**, 083B02 (2019).

[31] Y. Akahoshi, S. Aoki, T. Aoyama, T. Doi, T. Miyamoto, and K. Sasaki, PTEP **2020**, 073B07 (2020).

[32] C. McNeile and C. Michael, Phys. Rev. D **73**, 074506 (2006).

[33] G. Martinelli and C. T. Sachrajda, Nucl. Phys. B **316**, 355 (1989).

[34] E. Shintani, R. Arthur, T. Blum, T. Izubuchi, C. Jung, and C. Lehner, Phys. Rev. D **91**, 114511 (2015).

[35] P. Estabrooks and A. Martin, Nuclear Physics B **95**, 322 (1975).

[36] S. D. Protopopescu, M. Alston-Garnjost, A. Barbaro-Galtieri, S. M. Flatté, J. H. Friedman, T. A. Lasinski, G. R. Lynch, M. S. Rabin, and F. T. Solmitz, Phys. Rev. D **7**, 1279 (1973).

[37] U.-G. Meissner, Physics Reports **161**, 213 (1988).

[38] R. Machleidt and I. Slaus, J. Phys. G **27**, R69 (2001).

[39] S. Aoki et al., Phys. Rev. D **84**, 094505 (2011).

[40] X. Feng, K. Jansen, and D. B. Renner, Phys. Rev. D **83**, 094505 (2011).

[41] C. B. Lang, D. Mohler, S. Prelovsek, and M. Vidmar, Phys. Rev. D **84**, [Erratum: Phys.Rev.D 89, 059903 (2014)], 054503 (2011).

[42] J. J. Dudek, R. G. Edwards, and C. E. Thomas, Phys. Rev. D **87**, [Erratum: Phys.Rev.D 90, 099902 (2014)], 034505 (2013).

[43] D. J. Wilson, R. A. Briceno, J. J. Dudek, R. G. Edwards, and C. E. Thomas, Phys. Rev. D **92**, 094502 (2015).

[44] C. Alexandrou, L. Leskovec, S. Meinel, J. Negele, S. Paul, M. Petschlies, A. Pochinsky, G. Rendon, and S. Syritsyn, Phys. Rev. D **96**, 034525 (2017).

[45] C. Andersen, J. Bulava, B. Hörz, and C. Morningstar, Nucl. Phys. B **939**, 145 (2019).

[46] M. Werner et al., Eur. Phys. J. A **56**, 61 (2020).

[47] M. Fischer, B. Kostrzewa, M. Mai, M. Petschlies, F. Pittler, M. Ueding, C. Urbach, and M. Werner, (2020).

[48] Y. Akahoshi, S. Aoki, and T. Doi, Phys. Rev. D **104**, 054510 (2021).

[49] S. Aoki, in 37th International Symposium on Lattice Field Theory (Jan. 2020).

[50] M. E. Peskin and D. V. Schroeder, in *An Introduction To Quantum Field Theory* (1995).

[51] H. Nielsen and M. Ninomiya, Nuclear Physics B **185**, 20 (1981).

[52] H. Nielsen and M. Ninomiya, Nuclear Physics B **193**, 173 (1981).

[53] L. H. Karsten, Physics Letters B **104**, 315 (1981).

[54] B. Sheikholeslami and R. Wohlert, Nucl. Phys. B **259**, 572 (1985).

[55] Y. Iwasaki, Nucl. Phys. B **258**, 141 (1985).

[56] S. Aoki et al., Nucl. Phys. B Proc. Suppl. **106**, 263 (2002).

[57] S. Aoki et al., Phys. Rev. D **72**, 054510 (2005).

[58] T. Yamazaki, K.-i. Ishikawa, Y. Kuramashi, and A. Ukawa, Phys. Rev. D **86**, 074514 (2012).

[59] T. Iritani et al., JHEP **10**, 101 (2016).

[60] C. R. Allton, C. T. Sachrajda, R. M. Baxter, S. P. Booth, K. C. Bowler, S. Collins, D. S. Henty, R. D. Kenway, B. J. Pendleton, D. G. Richards, J. N. Simone, A. D. Simpson, B. E. Wilkes, and C. Michael, Phys. Rev. D **47**, 5128 (1993).

[61] N. Ishii, S. Aoki, T. Doi, T. Hatsuda, Y. Ikeda, T. Inoue, K. Murano, H. Nemura, and K. Sasaki, Phys. Lett. B **712**, 437 (2012).

[62] T. Miyamoto, Y. Akahoshi, S. Aoki, T. Aoyama, T. Doi, S. Gongyo, and K. Sasaki, Phys. Rev. D **101**, 074514 (2020).

[63] S. Aoki et al., Phys. Rev. D **65**, 094507 (2002).

[64] S. Aoki et al., Phys. Rev. D **73**, 034501 (2006).

[65] S. Ueda, S. Aoki, T. Aoyama, K. Kanaya, H. Matsufuru, S. Motoki, Y. Namekawa, H. Nemura, Y. Taniguchi, and N. Ukita, J. Phys. Conf. Ser. **523**, 012046 (2014).

[66] K. Murano, N. Ishii, S. Aoki, T. Doi, T. Hatsuda, Y. Ikeda, T. Inoue, H. Nemura, and K. Sasaki, Phys. Lett. B **735**, 19 (2014).

[67] E Hiyama, Y Kino, and M Kamimura, Progress in Particle and Nuclear Physics **51**, 223 (2003).

[68] A. Abdel-Rehim, C. Alexandrou, J. Berlin, M. Dalla Brida, J. Finkenrath, and M. Wagner, Comput. Phys. Commun. **220**, 97 (2017).

[69] T. Iritani, S. Aoki, T. Doi, S. Gongyo, T. Hatsuda, Y. Ikeda, T. Inoue, N. Ishii, H. Nemura, and K. Sasaki, Phys. Rev. D **99**, 014514 (2019).

[70] S. Aoki et al., Phys. Rev. D **79**, 034503 (2009).

[71] B. G. Giraud, K. Kato, and A. Ohnishi, J. Phys. A **37**, 11575 (2004).

[72] J. Aguilar and J. M. Combes, Commun. Math. Phys. **22**, 269 (1971).

[73] E. Balslev and J. M. Combes, Commun. Math. Phys. **22**, 280 (1971).

[74] K. Sasaki, N. Ishizuka, M. Oka, and T. Yamazaki, Phys. Rev. D **89**, 054502 (2014).

[75] T. Blum et al., Phys. Rev. D **104**, 114506 (2021).

[76] D. Guo, A. Alexandru, R. Molina, M. Mai, and M. Döring, Phys. Rev. D **98**, 014507 (2018).

[77] R. A. Briceno, J. J. Dudek, R. G. Edwards, and D. J. Wilson, Phys. Rev. D **97**, 054513 (2018).

[78] R. A. Briceno, J. J. Dudek, R. G. Edwards, and D. J. Wilson, Phys. Rev. Lett. **118**, 022002 (2017).

[79] J. J. Wu, W. Kamleh, D. t. Leinweber, R. D. Young, and J. M. Zanotti, J. Phys. G **45**, 125102 (2018).

[80] I. Kanamori and H. Matsufuru, in Computational Science and Its Applications – ICCSA 2018 (2018), pp. 456–471.

[81] T. Amagasa et al., J. Phys. Conf. Ser. **664**, 042058 (2015).

[82] S. Aoki, J. Balog, and P. Weisz, JHEP **05**, 008 (2010).

[83] S. Aoki, J. Balog, and P. Weisz, JHEP **09**, 083 (2010).

[84] S. Aoki, J. Balog, and P. Weisz, New J. Phys. **14**, 043046 (2012).

[85] S. Aoki, J. Balog, and P. Weisz, Prog. Theor. Phys. **128**, 1269 (2012).

[86] S. Aoki, J. Balog, T. Doi, T. Inoue, and P. Weisz, Int. J. Mod. Phys. E **22**, 1330012 (2013).